Wideband Micro-Power Generators for Vibration Energy Harvesting

by

Mostafa Soliman

A thesis
presented to the University of Waterloo
in fulfillment of the
thesis requirement for the degree of
Doctor of Philosophy
in
Electrical and Computer Engineering

Waterloo, Ontario, Canada, 2009

I hereby declare that I am the sole author of this thesis. This is a true copy of the thesis, including any required final revisions, as accepted by my examiners.

I understand that my thesis may be made electronically available to the public.

Abstract

Energy harvesters collect and convert energy available in the environment into useful electrical power to satisfy the power requirements of autonomous systems. Vibration energy is a prevalent source of waste energy in industrial and built environments. Vibration-based energy harvesters, or vibration-based micro power generators (VBMPGs), utilize a transducer, a mechanical oscillator in this application, to capture kinetic energy from environmental vibrations and to convert it into electrical energy using electromagnetic, electrostatic, or piezoelectric transduction mechanisms.

A key design feature of all VBMPGs, regardless of their transduction mechanism, is that they are optimally tuned to harvest vibration energy within a narrow frequency band in the neighborhood of the natural frequency of the oscillator. Outside this band, the output power is too low to be conditioned and utilized. This limitation is exacerbated by the fact that VBMPGs are also designed to have high quality factors to minimize energy dissipation, further narrowing the optimal operating frequency band. Vibrations in most environments, however, are random and wideband. As a result, VBMPGs can harvest energy only for a relatively limited period of time, which imposes excessive constraints on their usability.

A new architecture for wideband VBMPGs is the main contribution of this thesis. The new design is general in the sense that it can be applied to any of the three transduction mechanisms listed above. The linear oscillator is replaced with a piecewise-linear oscillator as the energy-harvesting element of the VBMPG. The new architecture has been found to increase the bandwidth of the VBMPG during a frequency up-sweep, while maintaining the same bandwidth in a frequency down-sweep. Experimental results show that using the new architecture results in a 313% increase in the width of the bandwidth compared to that produced by traditional architecture. Simulations show that under random-frequency excitations, the new architecture collects more energy than traditional architecture.

In addition, the knowledge acquired has been used to build a wideband electromagnetic VBMPG using MicroElectroMechanical Systems, MEMS, technology. This research indicates that a variety of piecewise-linear oscillators, including impact oscillators, can be implemented on MPG structures that have been built using MEMS technology. When the scale of the MPGs is reduced, lower losses are likely during contact between the moving oscillators and the stopper, which will lead to an increase in bandwidth and hence in the amount of energy collected.

Finally, a design procedure has been developed for optimizing such wideband MPGs. This research showed that wideband MPGs require two design optimization steps in addition to the traditional technique, which is used in all types of generators, of minimizing mechanical energy losses through structural design and material selection. The first step for both regular and wideband MPGs minimizes the MPG damping ratio by increasing the mass and stiffness of the MPG by a common factor until the effect of size causes the rate at which energy losses increase to accelerate beyond that common factor. The second step, which is specific to wideband MPGs, tailors the output power and bandwidth to fit the Probability Density Function, PDF, of environmental vibrations. A figure of merit FoM was devised to quantify the quality of this fit. Experimental results show that with this procedure, the bandwidth at half-power level increases to more than 600% of the original VBMPG bandwidth.

Acknowledgments

First of all, I would like to express my sincere gratitude to my supervisors Professor Raafat Mansour, Professor Ehab El-Saadany and Professor Eihab Abdel-Rahman, for their guidance, encouragement, and contributions in the development of my research. Without their vision, deep insight, advice, and willingness to provide funding, this work would not have been possible. Their extensive knowledge, strong analytical skills, and commitment to the excellence of research are certainly treasures to their students. They give students freedom to explore the uncharted areas while providing the needed assistance at the right time. They are willing to share their knowledge and career experience and give emotional and moral encouragement. Their hard working attitude and high expectation toward research have inspired me to mature into a better researcher. I feel they are not just advisers but role models and friends. Working with them is proved to be a rewarding experience. I would like to thank them genuinely for everything I have achieved in my research so far.

I would also like to thank Prof. Patricia Nieva, Siva Sivoththaman, and Prof. Kankar Bhattacharya, for serving on my dissertation committee and providing valuable advice on my research. They have devoted precious time reading my thesis. Their constructive comments and valuable suggestions have greatly improved this dissertation.

Special thanks go to Bill Jolley of the Centre For Integrated RF Engineering (CIRFE). He created such a wonderful collaborative research environment and pleasant work atmosphere. I benefit greatly from his solid and broad technical knowledge, insightful comments, and invaluable advice.

I would like to thank my fellow graduate students in the CIRFE, with whom I have shared numerous hours (days and nights), and have had several intellectually stimulating discussions covering a wide range of topics.

This dissertation is dedicated to my parents whose love, sacrifice, support, and prayers have always been the greatest inspiration for me in my pursuit for betterment. My deepest acknowledgment goes to my sincere wife Nevien for her dedicated support and encouragement. This dissertation could not be completed without her presence beside me. My final acknowledgment goes to my lovely kids Rahma and Omar.

To my father, to my mother

To my sincere wife Nevien

and

To my beloved children, Rahma and Omar

Contents

List of Tables

List of Figures

Chapter 1

Introduction

1.1 Preamble

Advances in the design of microsystems and wireless platforms have paved the way for a whole new class of small, low data rate and low-power embedded autonomous sensors and networked sensor arrays [1]-[6]. These new wireless sensors are useful in built environment control; emergency response; and structural health monitoring of airframes, ships, and vehicles. In recent wireless sensor applications, the problem of wiring a large number of nodes in a dense network has become critical with respect to the prohibitive cost of wiring power to them or replacing them. For the nodes to be conveniently placed and used, they must be small, which places severe limits on their lifespan if they are powered by a battery meant to last the entire life of the device.

Thus far, batteries are the main power source for such wireless sensor networks. Batteries are classified as constant energy sources, but at some point voltage produced by the battery drops to a level where it is no longer useful, and the energy remaining in the battery is wasted. Recharging or replacing batteries in a network of sensors is very expensive. As well, whatever their useful lifespan, batteries contain hazardous chemical materials that harm the environment. Driven by these

technical, economic, and environmental reasons, energy harvesting technologies are gaining attention as alternative power sources that can overcome these challenges. This new powering technology could lead to clean self-powered wireless sensor networks with stable power sources and sensors with long lifespans. Energy harvesting thus seems to be a promising and effective solution for delivering power to wireless sensor networks.

Energy harvesting refers to the use of energy present in the environment of an application that enables it to perform its own task or function through a convenient energy converter or transducer, called a micro-power transducers or micro-power generators (MPG). The advantage of using the energy present in the immediate environment is that it minimizes or eliminates the need for external sources of energy and the need to transport this energy from another location.

A system or device can become self-powered through the attachment of a convenient energy harvester to the sensor. A self-powered sensor with wireless communication greatly minimizes the complexity and cost of monitoring and control, while enhancing reliability and flexibility. The lifetime of the whole system then becomes equal to the life of the powering transducer itself. Furthermore, when the device reaches the end of its lifespan, no further concern or resources are required with respect to disposing of hazardous chemicals from batteries, retrieving valuable resources; or draining energy from fuel cells, capacitors, or any other energy storage device. Even if a system uses a battery, harvesting energy can decrease the energy demand on the battery and prolong its life and excess energy present at any particular moment can even be used to recharge the battery.

Solar (light), thermal gradient, human, fluid flow, and vibration are types of environmental energies that can be harvested and converted to useful electrical energy. However, because vibration energy exists in many industrial, built, and transportation environments, this waste energy has been chosen as the focus of this thesis. Vibration energy can be converted to electrical energy through three main

kinds of transduction mechanisms: electromagnetic, electrostatic, and piezoelectric transduction mechanisms. All vibration energy conversion mechanisms use a linear mechanical oscillator to resonate naturally according to the excitation frequency presents in the environment. In addition, VBMPGs are designed to have a very high quality factor in order to minimize energy loss in the air and/or friction damping which leads to a narrow operating frequency band.

Regardless of the transduction mechanism (electromagnetic, electrostatic, or piezoelectric), the design of VBMPGs must include two important considerations that limits their usability in today's market:

- *Narrow frequency band*: The frequency of ambient or waste vibrations is either predetermined; well characterized; or probabilistic; random and wideband. If the frequency is predetermined, then the resonant frequency of the VBMPG has to be tuned to the main frequency component of the environment, in which case the design must be optimized with respect to the amount of *power* generated. However, if the frequency of the environment is probabilistic, the traditionally designed VBMPG fails to collect the required amount of energy. The structure of the VBMPG must be modified in such way that its resonant frequency is self-tuned to match the excitation frequency. Such resonant frequency self-tuning can be either active or passive. For active self-tuning, additional actuation system and/or additional circuitry must be added to the MPG, which will add more energy requirements to the MPG. However, for passive self-tuning, the structure is able to change its resonant frequency according to the excitation frequency without adding any active elements to the system. In both active and passive self-tuning techniques, the MPG has a wider frequency bandwidth, and the collected *energy* is the parameter that is optimized.

- *Power density* ($\mu\,\mathrm{W/cm^3}$): Most of the currently available VBMPGs designs

suffer from low power density, which is the amount of useful power output (μ Watts) divided by the generator's total volume (cm^3). This problem stems from the large volume of the VBMPG structure, usually a few tens of cm^3 to 200 cm^3 and the load optimization. Power density can be improved if the MPG's volume is decreased using a mass-production fabrication technique, such as MicroElectroMechanical Systems (MEMS) fabrication techniques. Utilizing a mass fabrication technique not only improves the generator's power density, but also decreases the cost per unit and reduces its size so that it fits better in applications that have space restrictions. Also the load is optimized by matching the electric damping coefficient with the mechanical damping coefficient.

Therefore, the efficient design of a VBMPG requires that its performance be enhanced and its size reduced, while keeping its power density as large as possible.

1.2 Research Objectives

MPGs used in environments characterized with random excitation frequency pattern suffer from low useful generated power due to their narrow frequency bandwidth. Enhancing the performance of vibration-based MPGs is the main focus of this research.

The main objectives of this research are as follows:

- To develop and optimize a novel passive resonant frequency self-tuning technique for widening the frequency bandwidth of a VBMPG that will harvest the vibration energy from the surrounding environment. As a passive technique, the proposed wideband technique in this research requires no additional actuation circuitries. In addition, it utilizes an inexpensive technology which will keep the cost of the products down.

- To implement the wideband technique on an inexpensive miniaturized VBMPG based on MEMS fabrication technology.

1.2.1 Approach

To realize these objectives, research has been conducted in four stages, explained below.

In the first stage, a standard, cantilever-based VBMPG prototype based on electromagnetic transduction was designed and built. The basic analytical model was developed and the parameters of the MPG were calculated using finite element analysis and the model was then verified experimentally.

In the second stage, a novel technique for widening the frequency bandwidth was proposed. The technique developed is based on inserting a nonlinear element into the linear oscillator, that is, the spring in this case, a piecewise-linear spring. Piecewise linearity can be achieved by either adding extra spring stiffness or increasing the stiffness of the spring after a specific stroke size is achieved. This kind of nonlinearity is known as hardening nonlinearity, which leads to a shift in the structure's resonant frequency to the right as the excitation frequency sweeps up beyond the resonant frequency of the VBMPG. It was found that using this kind of hardening nonlinearity increases the bandwidth, that is the level at which half power is generated, when the frequency sweeps up, while maintaining the same frequency band when the frequency sweeps down. An analytical model was then developed in order to predict the system's performance. A numerical model based on MATLAB was created for verifying the analytical model. To test the principle, the MPG was modified to accommodate for a stopper with variable vertical and horizontal positions. Good agreement among the analytical, numerical, and experimental results was obtained.

In the third stage, a design of MEMS-based electromagnetic MPGs utilize the

proposed technique is presented. A novel electromagnetic MEMS-based MPG was designed, built, and simulated. The design procedure was divided into sections, including an energy conversion concept in addition to the structure of the generator . In addition, both the magnetic field system and the mechanical structure were modeled and simulated using the Finite Element Analysis (FEA). Challenges with the technology were overcome in order to produce a working electromagnetic MEMS-based vibration-to-electricity generator with the highest possible energy conversion efficiency. Although the power density is not higher than stat-of-the-art designs, the proposed design was built using MEMS technologies with an inexpensive process that facilitates mass production. In addition, the novel wideband technique developed can be implemented on fabricated MEMS designs.

The final stage involved the study of the parameters that control the performance of the modified VBMPG, which utilizes a piecewise-linear oscillator: the bandwidth and the power level. Four controlling parameters were found: the stiffness ratio, the linear system damping ratio, the contact (or impact) damping ratio, and the stroke size at the moment of stiffness changes. In this stage, the linear system damping ratio was the first to be optimized. It was then found that the other three parameters are dependent on one another, so performance was optimized in order to maximize the amount of energy collected rather than the amount of power generated. Different stiffness ratios and stroke sizes were examined experimentally in order to extract an optimized configuration of the piecewise-linear oscillator. It was found that the optimized configuration depends on the frequency pattern of the random excitation in the environment.

1.3 Thesis Outline

The remainder of the thesis is organized as follows. Chapter 2 provides the necessary background and a literature review of the topics related to this research.

It provides an introduction to potential power sources for modern wireless sensor network applications, with a special focus on vibration-based energy harvesting and a general view of VBMPGs along with a description of different types. For each type, the working principles, a literature review of the most important work performed with respect to this type, advantages and drawbacks are reported and discussed. Finally a comparison is presented and a conclusion is drawn, which will demonstrate the reasons for the choice of electromagnetic MPG's for this study. Finally, a comprehensive literature review of the most recent work done with respect to the wideband issue is presented. Chapter 3 discuses a general analysis of VBMPGs. Chapter 4, describes the design, analysis, simulation, and testing of a standard electromagnetic prototype used to verify the new technique. Chapter 5 explains the dynamics of the proposed piecewise-linear oscillator and presents the analytical model, the numerical simulations, and the experimental results for an electromagnetic VBMPG that utilizes such kind of oscillators. A design and a fabrication road map for implementing the new technique on MEMS-fabricated MPGs is also proposed. Chapter 6 presents an optimization procedure for maximizing the amount of energy harvested for a certain random excitation. Finally, Chapter 7 provides the conclusions of this research and highlights possible future work.

Chapter 2

Literature Review and Background

The field of vibration-based energy harvesting has been recognized as an area of intensive research for the past few years. The current limitations on powering wireless sensor network nodes and the desire for a robust, reliable, and sustainable alternative power source are the driving forces behind this research.

This chapter provides a literature survey of alternative power sources for wireless sensors, with a special focus on vibration energy harvesting. A mechanical-to-electrical energy conversion transducer must be deployed in order to harvest vibration energy. The transduction mechanism could be electromagnetic, electrostatic, or piezoelectric. Therefore, the survey begins with a brief general classification of potential power sources, followed by an introduction of the vibration energy harvesting classifications and techniques that are closely related to this work, which focuses on electromagnetic VBMPGs. A literature review of the recent research work on the wideband frequency operation of VBMPGs is then provided.

2.1 Potential Power Sources

The powering of modern wireless sensor network applications can be achieved through two approaches. The first method is to enhance the energy density of the energy storage systems in order to increase their lifespan; such systems are called *constant energy systems or energy reservoirs*. The second technique is to develop novel techniques to collect waste energy in the application's environment and converting it to useful electrical energy; such systems are called *constant power systems*.

In constant energy systems that depend mainly on energy storage devices, the efficiency of the system is measured by its energy density. Therefore, the output power is a function of the amount of the energy stored, which means that the system can provide power to the load as long as the stored energy is still available. Once the stored energy vanishes, power is no longer provided to the load, and the powering system must be either replaced or recharged. Energy-harvesting techniques, on the other hand, are constant power sources, which means that the energy delivered to the load is a function of the converted power. As long as the source of power is available, energy is provided to the load. Consequently, for projects or applications that have long lifespan, constant power sources, or energy harvesting techniques, are desirable. the following is a brief introduction to the most important techniques used for both powering approaches.

1- Constant energy sources: Energy can be stored in powering devices in the form of electrochemical energy, as in batteries and micro-batteries; in a chemical energy storage mechanism, as in combustion fuel systems; or as electrical energy, as in capacitor systems.

- *Batteries and micro-batteries*: Although batteries provide the significant advantage of producing a regulated voltage without the need for additional power electronic circuits, they may not be a convenient means of powering

the modern applications previously mentioned for the following reasons. First, batteries have a limited lifespan that is dependent on the amount of the stored energy. They can also contain environmentally hazardous contents. In addition, as the amount of stored energy decreases, the output voltage may not be stable enough to provide the power required for the application and the energy remaining in the battery is thus wasted. Finally, the replacement or recharging of batteries in embedded environments or large networks is unfeasible task. Thin-film technologies are being used to develop micro-batteries, which are on-chip batteries with an overall thickness of 10s of micrometers and a surface area in the range of cm^2 [8]; however, they are still energy-limited devices.

- *Micro-fuel cells*: Micro-fuel cells convert chemical energy to electrical energy. They have the advantage of a higher surface-to-volume ratio. A micro-fuel cell capable of producing approximately 25 mA and $1-1.5$ V from a thin film with an area of $2\,\mathrm{cm}^2$ was designed and fabricated in [7]. Although micro-fuel cells have the advantage of high energy density, they have very low efficiency on the millimeter scale. In addition, the voltage level is not stable when the cell is being loaded.

- *Ultracapacitors*: Ultracapacitors are a category of devices that lie between standard capacitors and rechargeable batteries. Their energy density is higher than that of standard capacitors and lower than that of rechargeable batteries [8]. However, these ultracapacitors provide very low current and thus can be used as a secondary power source, but not as the primary power source for applications with long lifespan.

Other constant energy sources include micro-heat engines and radioactive power sources, which are outside the scope of this thesis.

2- Constant power sources:

An alternative to energy reservoirs, constant energy sources are based on energy harvesting technology. With this approach, an energy converter, an MPG, is used to harvest, or scavenge, and then convert energy that exists in the application's environment into useful form of electric power that can be utilized by a circuit or system. The most interesting advantage of energy harvesting is that the electric load, circuit, system, or sensor, has a lifespan limited only by the failure of its own components. However, energy harvesting might be the most difficult realizable powering technique because the environment is unique to each application. Consequently, no one solution will fit all or even most applications. Forms of waste energy available for harvesting are solar/light energy; temperature gradient energy; human power; fluid flow; and vibration energies which are the most important classes of kinetic energy.

- *Solar/light energy*: Solar and light energy can provide approximately 100 $\mathrm{mW/cm^2}$ at midday on a sunny day [8]; however, indoor lighting conditions have a far lower power density, in the order of $100\,\mu\mathrm{W/cm^2}$. Single crystal silicon solar cells are convenient for outdoor applications as they have a spectral response close to that of outdoor light and they provide efficiencies of 15% to 20% [9]. For indoor applications, thin film amorphous silicon solar cells provide higher efficiency than single crystal silicon solar cells because their spectral response closely matches indoor light, and they offer about 10% efficiency [8]. Therefore, the power density available from solar cells is 15 $\mathrm{mW/cm^2}$ for outdoor applications and $10\,\mu\mathrm{W/cm^2}$ for indoor applications. Although solar cells offer relatively high power density, they are not suitable for embedded systems in structures or buildings.

- *Temperature gradient energy*: Temperature differences can be used to generate an electric current utilizing, the Seebeck effect. However, this method requires that the two ends of the generator be placed in different locations that have

different temperatures, which may place constraints on the usefulness of this energy conversion technique.

- *Human power*: Energy is emitted from the human body in several forms, such as heat flow through the surface of the skin or mechanical energy as a result of body movements. However, extracting this energy from the generation location and transporting it to the application location could be a challenge.

- *Kinetic energy*: Kinetic energy harvesters are divided into two main categories, rotary (rotational-based) and linear (vibration-based) (Figure 2.1). The transduction mechanism (energy conversion from mechanical to electrical energy) can be realized using either electromagnetic, electrostatic, or piezoelectric energy converters.

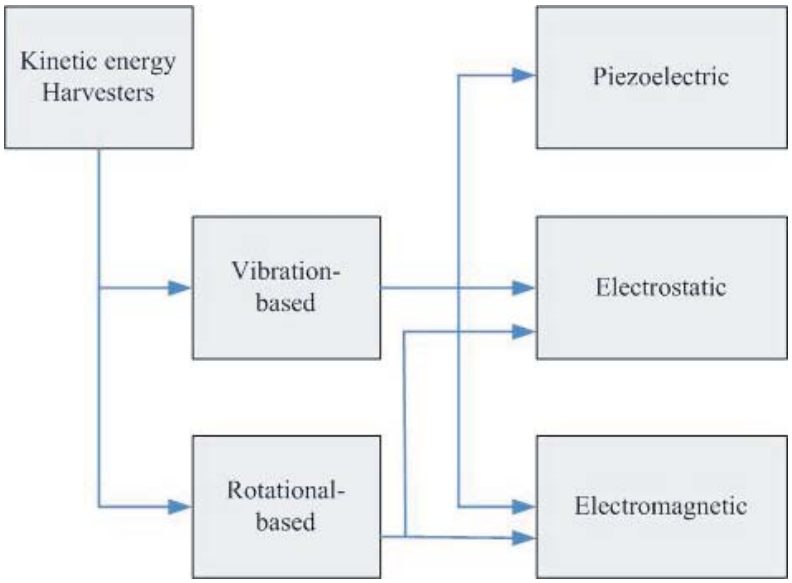

Figure 2.1: A general classification of kinetic energy harvesters.

  - *Rotational-based*: The rotation is produced by a fluid, which can be either a gas or a liquid. The flow of the fluid is used to rotate a turbine, which transmits the input mechanical power into electrical energy. This process requires that an energy converter be inserted into the flow path

of the fluid, such as exhaust pipes, air conditioning and heating systems, or blood vessels. The main drawback of this scenario is the complexity of the mechanical system , i.e., the turbine/rotor coupling.

– *Vibration-based*: Low-level vibrations occur in many environments, such as large commercial buildings, trains, ships, aircrafts, automobiles, and rotating machinery. It has been reported that electric power of about $300\,\mu$ W/cm^3 can be extracted from these low-level vibrations [9]. The amount of power depends on factors such as the frequency and the acceleration of the input vibrations as well as the design of the structure of the energy converter itself. An MPG based on mechanical vibrations has distinct advantages: it can be attached to an embedded system inside a structure or building, it works in a constant temperature environment, and it can be portable and can operate outdoors or indoors as long as the source of vibration is available.

Figure 2.2 shows a comparison of the power produced by batteries, as energy reservoirs, and that produced by solar and vibration energy sources, as constant power sources [9]. For long term projects or applications, harvesting either solar or vibration energies is preferable in order to provide constant power to those loads. Solar energy offers higher power density than mechanical vibration energy, but because of several constraints associated with solar cells, this research focuses on vibration energy harvesting as a constant power source.

2.2 Vibration as a Constant Power Source

Vibrations cab be either random or constant. Constant vibration sources are characterized by their fixed displacement magnitude (or acceleration magnitude), and vibration frequency. Reference [10] showed that low level constant vibrations occur in many environments. Table 2.1 lists sample sources of vibration according

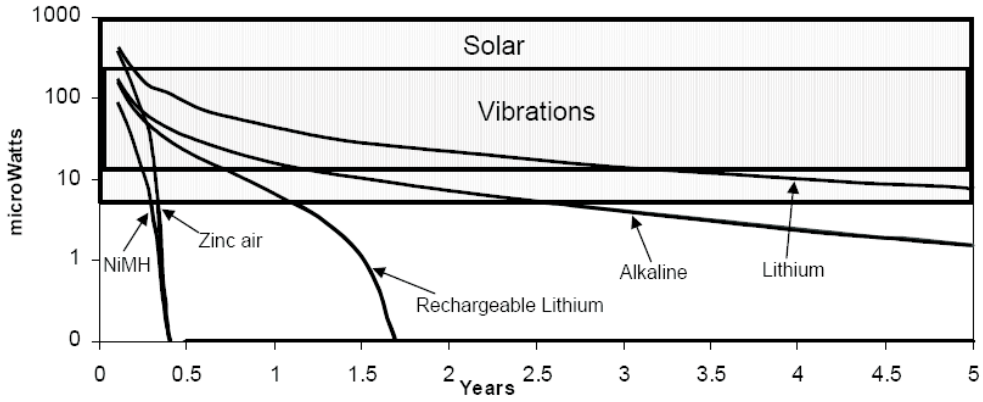

Figure 2.2: A comparison of the power produced by batteries, solar energy and vibration energy harvesting.

to the magnitude of the frequency and acceleration of the fundamental vibration mode. On the other hand, random vibrations are produced from irregular motion, such as a human walking energy. Random vibrations are characterized by varying magnitude or frequency, or both, over the time and occur in many industrial applications where the frequency of the environment changes randomly within a certain range. This work focuses on random vibration sources characterized by constant magnitude and varying frequency.

2.3 Vibration-Based Micro-Power Generators

To couple the environmental vibrations to the transduction method, vibration energy harvesting requires a transducer, an energy converter. Such transducers must be designed carefully in order to maximize the energy converted with minimum loss. To date, the method reported for collecting wasted vibration energy is an inertial structure with simple mass-spring-damper system attached to a fixed frame. It operates by damping the motion of the mass with respect to the fixed frame. In simple terms, when the fixed frame, or housing, vibrates due to environmental vibrations, the mass-spring system vibrates as well, thus creating a relative displacement with

Table 2.1: Magnitude of the acceleration and frequency of the fundamental vibration mode for sample vibration sources.

Vibration source	**Acceleration (m/sec^2)**	**Mean frequency (Hz)**
Car engine compartment	12	200
Base of a 3-axis machine tool	10	70
Blender casing	6.4	121
Clothes dryer	3.5	121
Car instrument panel	3	13
Small microwave oven	2.5	120
Windows next to a busy street	0.7	100
CD on a notebook computer	0.6	75
Second-story floor of a busy office	0.2	100

respect to the housing. If the mass-spring system's resonant frequency does not match the input excitation frequency, the mass's stroke is negligible and almost no power is generated. However, if its resonant frequency matches the excitation frequency, then the mass's stroke is magnified by the system's total damping ratio, and a considerable amount of energy is converted to useful electrical energy.

The transduction mechanism may utilize either the mechanical strain produced from a deformation of active materials, such as piezoelectric materials, or the relative displacement of moving structures such as electromagnetic transduction mechanism, which utilizes the relative velocity, or electrostatic transduction mechanism, which utilizes the relative position [11]. Each transduction mechanism has advantages and drawbacks, which are discussed in the following subsections. As well, the principle of operation, and the most important previous research with respect to each mechanism are presented, with a special focus on the electromagnetic transduction mechanism. A comparison of the three transduction mechanisms is also

provided.

2.3.1 Piezoelectric MPGs

Piezoelectric materials are materials that deform when subjected to differences in electrical potential or alternatively, produce potential difference (charge separation) when subjected to input mechanical deformation. This method of transduction is used to convert vibration energy to electrical energy by applying periodic forces or stresses to a piezoelectric material. The direction and amount of force applied affect the polarization of the material and hence determine the amount of the voltage generated [12]. Piezoelectric materials are found in a variety of forms, such as single crystal (e.g., quartz), piezoceramics (e.g., lead zirconate titanate PZT), and thin or thick films [13].

Basic analysis of piezoelectric MPGs was presented in [8]; however, more advanced analysis that considered more mathematical issues was provided in [14]. Human-powered piezoelectric MPGs were proposed in [15]-[19]. The generators were fabricated from lead zirconate titanate (PZT) wafers and flexible multi-layer polyvinylidene fluoride (PVDF) films inside shoes in order to convert the mechanical energy produced by humans walking into electricity. Other research has shown the potential of piezoelectric energy harvesting at the MEMS scale for biomedical applications [20]-[23].

Inertial piezoelectric energy harvesters have been studied at both the macro size [24] and MEMS scale [25]-[26]; reference [8] concluded that the piezoelectric coupling degrades when it is scaled down, resulting in reduced power density.

2.3.2 Electrostatic MPGs

Another transduction mechanism is based on electrostatic energy conversion. Simply, the total electrical energy stored in a variable capacitor increases if precharged

capacitor plates are separated by an external mechanical force. The work done against the electrostatic force between the charged electrodes is part of the harvested mechanical energy. Two architectures can form an electrostatic energy harvester based on the way the capacitor's plates are charged: battery-based and electret-based designs. In general, as shown in Figure 2.3, two energy conversion cycles are possible: voltage-constrained and charge-constrained cycles [27] [28].

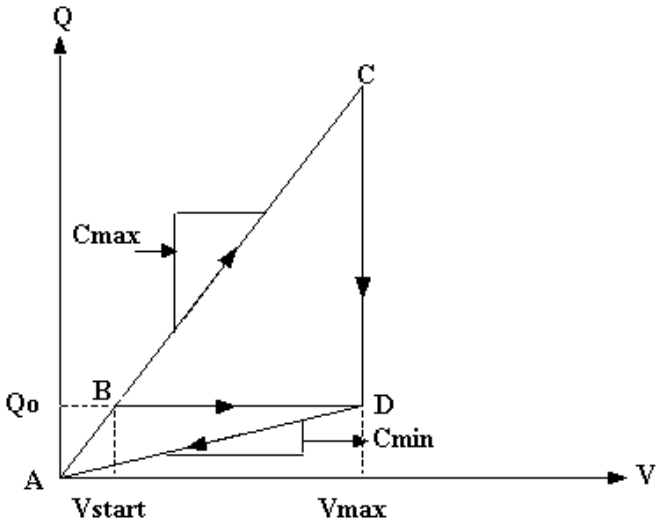

Figure 2.3: Energy conversion cycles.

a voltage-constrained cycle is represented in Figure 2.3 by the closed path ACDA, while the closed path ABDA represents a charge-constrained cycle. As shown in Figure 2.3, the increase in the energy stored in the variable capacitor, that is due to the separation of its plates can be expressed as follows [27]:

$$E_{\text{voltageconstrained}} = \frac{1}{2}(C_{\max} - C_{\min})V_{\max}^2 \tag{2.1}$$

$$E_{\text{chargeconstrained}} = \frac{1}{2}(C_{\max} - C_{\min})V_{\max}V_{start} \tag{2.2}$$

From equations 2.1 and 2.2, the energy converted from the voltage-constrained cycle is much larger than that converted from the charge-constrained cycle. How-

ever, voltage-constrained cycles require two reservoirs with different voltage levels: one with a high level to keep the voltage constant across the variable capacitor during the change from maximum to minimum capacitance values and one with a low level to supply the load with the required power (Figure 2.3). Furthermore, a voltage-constrained cycle requires a power electronics that is much more complicated than that required by a charge-constrained cycle. A voltage-constrained conversion cycle also requires a large current conduction period, i.e., path CD in Figure 2.3, which is associated with larger power losses. It was concluded that a charge-constrained cycle is more feasible than a voltage-constrained cycle [27] and that the energy collected from a charge-constrained cycle could be close to that collected from a voltage-constrained cycle by adding a parallel capacitor with a very high value [11].

Battery-based electrostatic MPGs can be classified into three types according the movement of the capacitor's plates with respect to each other [9] as shown in Figure 2.4. In-plane overlap structures with a predicted generated power of $8\,\mu$W were discussed in [28] and [29], and in-plane closing gap structures with a predicted output power density of $200\,\mu\mathrm{W/cm^3}$ were presented in [30]. Out-of-plane structures with a predicted power density of $100\,\mu\mathrm{W/cm^3}$ were presented in [9] and [31]. Another type of in-plane closing gap MEMS-based capacitive MPG was demonstrated in [32]. With an area constraint of $1\,\mathrm{cm^2}$ and an auxiliary battery supply of $3.6\,\mathrm{V}$, the device was designed to generate $31\,\mu$W of output power with an output saturation voltage of $40\,\mathrm{V}$ and a load of $5\,\mathrm{M\Omega}$. An external mass of $4\,$grams was needed in order to adjust the resonance of the device to match the input vibration of $2.25\,\mathrm{m/s^2}$ at $120\,\mathrm{Hz}$.

In an electret-based electrostatic MPG, a highly precharged electret, which is a dielectric material that traps a high number of charges within it, replaces the regular battery to provide charges for the moving plate capacitors. This kind of electrostatic harvesters with a predicted power in the order of a few μW was presented in [33]-

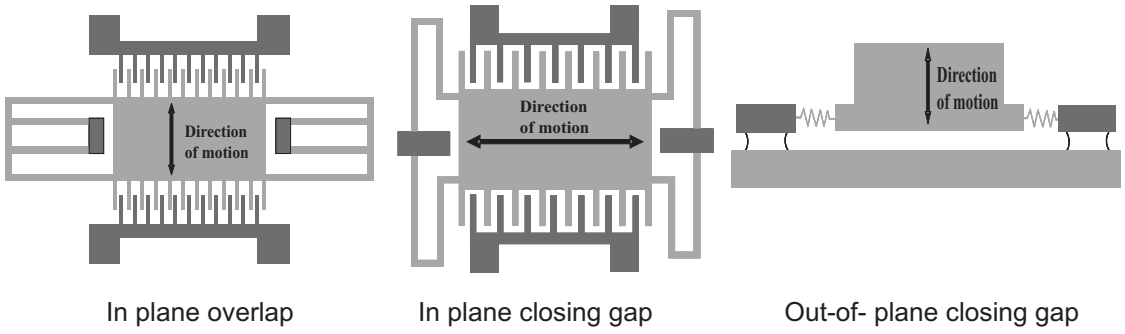

Figure 2.4: Variable capacitor configurations [8].

[35].

2.3.3 Electromagnetic MPGs

The operating principle of electromagnetic MPGs is based on Faraday's law, which states that a relative motion between a magnetic field and an electrical wire or a change in the flux linkage with a wire induces an electromotive force (EMF) in that wire. As is discussed in details in the next chapter, the EMF value depends on the strength of the magnetic field, the length of the wire, and the relative velocity (or flux linkage rate) between the magnetic field and the wire (figure 2.5), equation 2.3 represents this relationship:

$$EMF = \frac{d\Phi}{dt} = Bl\frac{dD}{dt} \tag{2.3}$$

where Φ is the total flux linkage in $Weber$; t is the time in seconds, and B, l, and D are the flux density in Tesla, the effective length of the wire in meters and the relative motion between the magnets and the coil in meter respectively.

The relative motion between the magnetic field and the coil can be produced by moving the magnets with respect to the coil or vice versa. The coil can be either wire-wound or micromachined. The electromagnetic MPGs, EMPGs, that have been researched are either macro-sized structures or miniaturized structures utilizing a microelectromechanical system (MEMS) fabrication techniques. How-

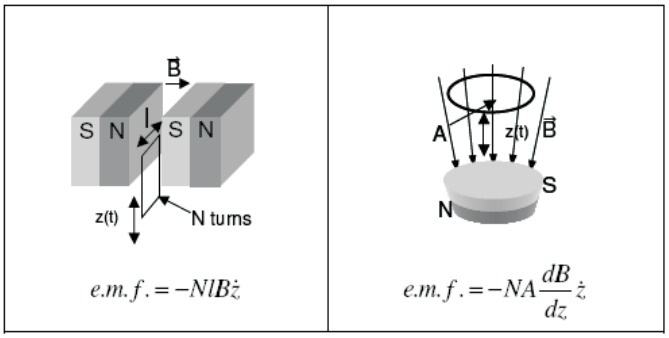

Figure 2.5: Electromagnetic induction [41].

ever, a common aspect of the EMPGs developed is that macro-sized permanent magnets (PM) are used to provide the required magnetic field. The PMs can be micromachined; however, it is reported in [36] that the maximum residual flux in a micromachined PM ranges from 0.2 T to 0.4 T, and the coercive force ranges from 100 KA/m to 400 KA/m. Unfortunately, these parameters are not comparable to those associated with the available rare earth PMs available for this research (1.27 T residual flux and at least 1 MA/m coercive force). The utilization of such micromachined PMs will produce a generator with low power density.

2.3.4 Scaling of Electromagnetic MPGs

An electromagnetic system can be based either on PMs or on electrically excited magnetic systems. Electrically excited magnetic systems, i.e., switched-reluctance or induction, perform poorly when scaled down because of the poor scaling of the currents required in order to establish the magnetic field [37] and [38]. On the other hand, the magnetic fields produced from PM magnetic systems are independent of size. The PM EMPGs seem to be a very attractive area of research as long as micromachined PMs are not used. The advances in MEMS technology have resulted in a variety of microfabricated structures that can be hybrid-integrated with a PM system in order to produce a new generation of miniaturized MEMS-based EMPGs. However, the practical implementation of MEMS-based EMPGs

involves many challenges, such as the manufacturing of the small and accurate parts that must be assembled with the PMs in order for such systems to operate. Regarding the scaling of the physical dimensions of the generator, it was concluded in [39] and [40] that power density decreases as the dimensions are reduced.

The following subsections discuses the most important work with respect to both macro and miniaturized MESM-based EMPGs.

2.3.4.1 Macro-Sized EMPGs

A moving coil with an attached 0.5 grams mass and a fixed permanent magnet was presented in [42]. The generator was 160 cm^3 and incorporated an attached transformer with a 1:10 turns ratio. Simulations showed that a maximum power of 400 μW could be generated from vibrations of about 2 Hz and a displacement amplitude of 2 cm due to humans walking, which is equivalent to an acceleration of 0.3 g (g represents the acceleration of gravity). The voltage generated was 180 mV before transformation and 1.8 V at the secondary terminals of the transformer. An 18 μW electrical load was successfully powered by such a generator. The primary drawback of this design is that the magnetic flux linkage cutting the coils, the main reason for which is that the magnetic field produced by the north pole of the magnet has to return to the south pole through a huge reluctance, i.e. air reluctance. Such a magnetic circuit is called an open magnetic circuit. Another disadvantage of an open magnetic circuit is the effect of the magnetic field on any surrounding electronics. The maximum power produced by the simulation assumed a steady state input vibration, which is not a realistic assumption in the case of a human walking. In addition, the generator was large, which is not practical for many modern applications such as embedded sensors/systems.

The modeling, simulation, manufacturing and testing of a cantilever spring-based moving magnet EMPG was described in [43] and [44]. A C-shape core of a soft magnetic material enclosed by a pair of NdFeB PMs was attached to the free

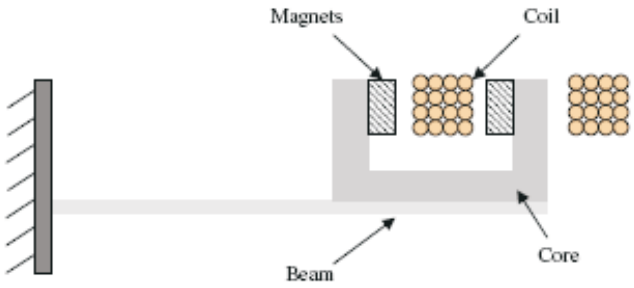

Figure 2.6: Electromagnetic MPG developed by [44].

end of a cantilever whose other end was anchored to a fixed frame. The C-shape core acts as an easy return path for the magnetic field so that the flux density in the air gap is increased (Figure 2.6). A fixed copper coil with 27 turns was attached to the fixed frame, thus allowing a relative displacement between the coil and the PMs when a base excitation is applied to the structure. A 530 μW power was generated of a 0.24 cm^3 total volume at 322 Hz and an excitation amplitude of 25 μm, i.e., $\approx$ 10 g. The excitation acceleration level used was very large and is not realized in many applications. The same structure generated approximately 40 μW at 1.2 g.

A moving magnet electromagnetic MPG capable of generating 10 μW with an input frequency of 64 Hz and a displacement amplitude of 100 μm, 16 g, has been proposed and tested, as presented in [45]-[48]. The induced voltage was relatively high about 2 V peak to peak with an overall volume about 1 cm^3. A spiral laser micromachined spring was used as the resonating structure. The mass of the magnet was 210 m grams, and concentric windings of 1500 turns were used. This huge number of turns in such a small volume results in a resistance that might be large enough to decrease the generated voltage and output load power when the generator is loaded. In addition, in [45], the authors were able to produce a micro-generator capable of generating 4 V peak to peak from a frequency input ranging from 60 Hz to 110 Hz with 200 μm displacement amplitude (28g-95g) and with a maximum RMS power of 680 μW. A strong PM was used in this structure, and the magnetic circuit was open circuited, which resulted in weak magnetic field. Moreover, the

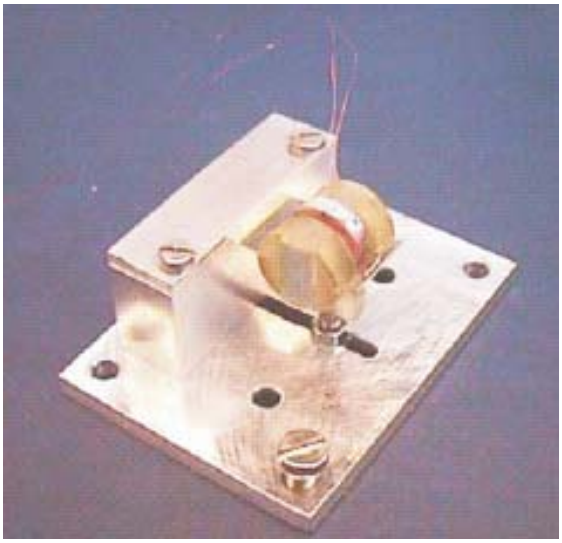

Figure 2.7: Improved electromagnetic MPG described in [49].

effect of the magnetic field on the surrounding microelectronics was not addressed. The acceleration levels used for this design were also very high due to the stiff spring design used.

The proposal and testing of another moving magnet electromagnetic MPG was presented in [49]. The generator is composed of a set of four PMs with a steel core attached to a cantilever and a fixed coil, as shown in Figure 2.7. A generator with an overall volume of 3.15 cm^3 was capable of producing an average power level of 157 μW at 250 mV when placed on a car engine with 3000 rev/min, which is equivalent to a 322 Hz vibration frequency. Both the voltage and the output power are at relatively high levels.

A smaller version of the EMPG presented in [49] was described in [50] and [51], Figure 2.8. The generator is only 150 mm^3 and generates 46 μW at an excitation frequency of 52 Hz and a 0.59 m/sec^2 acceleration level ($\approx 310\,\mu W/cm^3$).

The theoretical analysis and experimental results of another 500 cm^3 moving PM vibration energy harvester were presented in [52]. The prototype utilizes a PM suspended by a set of springs. The design assumes that the excitation frequency always matches the resonant frequency of the generator, but the amplitude of the

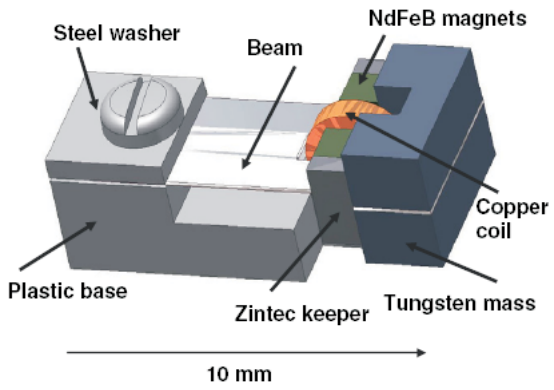

Figure 2.8: Small electromagnetic MPG developed in [50].

applied oscillatory motion varies, which has a direct impact on the generator's stroke and, in turn, on the amount of power generated. A micro controller was added in order to change the value of the electrical damping coefficient so that the output power from the generator would be maximized. A micro controller changes the connection of the generator coils, which in turn, changes the electrical damping coefficient in order to keep the amplitude of the vibration within the allowable limits of the stroke. Although using a micro controller and switch reduces the amount of output power and increases the complexity of the system, the generator produced a relatively high amount of power that reached 95 mW from 6 Hz and a 2.75 mm vibration source.

A linear EMPG powered from a human body was described in [53]. The generator consisted of a moving cylindrical translator that carries a set of separated PMs and that is positioned within a series of stationary coils placed on the stator. The power output was reported to be 2-25μW, depending on the position of the generator on the human body. When the generator was mounted just below the knee, it was able to generate an average power of 35 μW with a total device volume of 30 cm^3.

A prototype of a human-driven electromagnetic MPG was presented in [54]. The generator replaces the mechanical part of the resonator, i.e., the spring, with

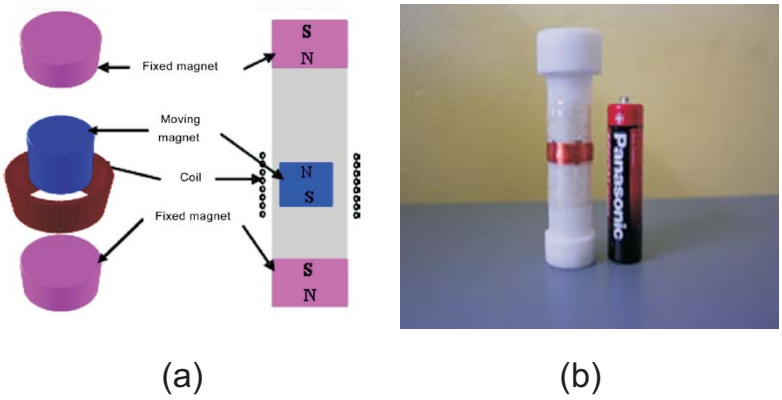

Figure 2.9: A tube electromagnetic MPG: (a) Construction, (b) General view [54].

a magnetic spring based on the repulsion force between same-polarity PMs. Figure 2.9 shows the construction of this generator. It consists of two alike PMs fixed on the two ends of the generator. In the middle is another moving back-to-back PM so that the repulsion force between the magnets keeps the moving magnets suspended between the two fixed magnets. A coil is wrapped around the housing of the generator. When the housing vibrates, the suspended moving magnets start to vibrate, and an induced EMF is generated in the coil when the flux linkage cuts the coil. The experimental results show that the prototype could generate 300 μW to 2.5 mW power from the motion of a human body.

In [55], a moving magnet electromagnetic MPG was designed and tested. A PM set with the magnetic circuit was attached to the end of an aluminum cantilever. The total generator volume was reported to be 45 cm^3. The load power delivered to a 1 KΩ resistive load was 6.5 mW with an excitation frequency of 34.5 Hz and 0.5 g of acceleration. The total power density was about 145 $\mu W/cm^3$.

2.3.4.2 Miniaturized MEMS-Based EMPGs

This section presents a comprehensive survey of the most important reported work on the MEMS-based EMPG, including the working principles and configurations

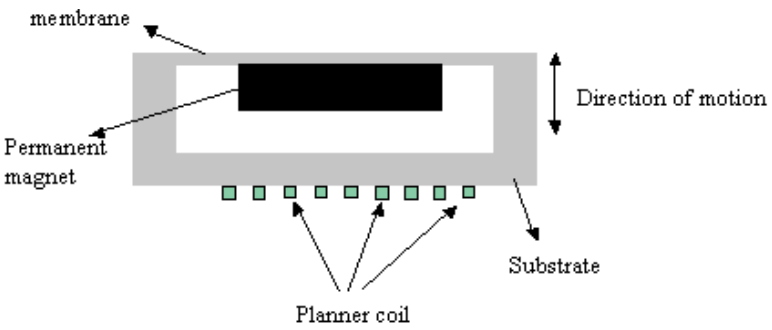

Figure 2.10: Illustration of the first vibration-based electromagnetic MPG.

utilized.

The first vibration-based electromagnetic MPG capable of generating 0.3 μW at an excitation frequency of 4.4 KHz and 0.5 μm vibration level, i.e. 39 g, was described in [56]-[58] with a generated voltage of only 8 mV. As shown in Figure 2.10, the structure used a fixed planar micromachined gold coil with 13 turns, and a seismic 0.3 mm^3 SmCo permanent magnet weighing 2.4 mgrams was attached to a micromachined membrane using a polymide solution. The total volume of 25 mm^3 resulted in a small power density of 12 μW/cm^3. The design demonstrated that power generation of about 1 μW and 100 μW at 70 Hz and 330 Hz, respectively, was feasible. The main drawback of that design is the low induced voltage, which is the result of the low number of turns of the coil and the low magnetic field cutting the coils due to the open-circuited magnetic circuit design.

Another vibration-based electromagnetic MPG was developed in [59], a schematic diagram of which is shown in Figure 2.11. From an input vibration source of 0.1 μm and 58 KHz, the analysis predicted a 1.4 mV and 6 nW output power with a 82 Ω load for a generator of 500$\times$100$\times$20μm^3 volume with 12 coil turns and a 30$\times$10$\times$6mm NdFeB PM. This design was not fabricated or tested and also this design suffers from low voltage because a counter EMF, but with lower value, is induced in the other side of the coil.

A two bonded wafers structure with two resonating structures was presented in

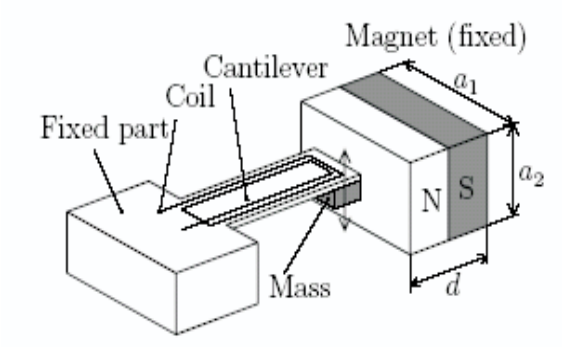

Figure 2.11: Schematic diagram of the vibration-electromagnetic MPG presented in [59].

[60]. The upper resonator consists of a diaphragm that supports an NdFeB PM and both of them form a low-frequency resonating structure, in the order of 1-100 Hz. However, the cantilevers that support the coils for the electromagnetic generation and the magnetic tips for the magnetic actuation form the lower resonators, with a high resonance frequency, in the order of 1-10 KHz. As the diaphragm resonates in response to input vibrations, it moves closer to the resonators below. The displacement between them is designed so that the magnetic tip, and hence, the lower cantilever resonators, are caught by the PM at s specific point and released from the magnet at another point. After the cantilever is released, it resonates according to its own resonance frequency, i.e., 1-10 KHz, and a generated voltage is induced in the coil due to the relative velocity between the magnet and the coil. The expected power was reported to be in the range of 2.5 μW per cantilever in a vacuum, with a maximum voltage of 150 mV from a $400\times300\times10\mu m^3$ cantilever. The complete microstructure was not fabricated, but a milli-scale prototype was produced and tested. The prototype showed an output power of only 4 nW at 6 mV per cantilever from a 700 Hz frequency and 0.64 μm vibration source. However, this structure is very complicated and requires complicated design and fabrication techniques. In addition, the induced voltage has an irregular waveform because of the

variation in the cantilever's resonance frequency over time, and the problem of an open magnetic circuit again arises.

An improved design to that presented in [56] is illustrated in [61]. The generator consits of a 1 mm thick Si wafer with a $20\times15\mu m^2$ cross section electroplated copper coil with 52 turns and a resistance of $100\,\Omega$. The mass-spring element is formed by attaching a bonded PM to a Kapton membrane. The device generates about $55\,\mu W$ at 380Hz from a $5\,\mu m$ excitation amplitude, which equates to 3 g. Unfortunately, the power generated results from the device's hysteresis. Also, Kapton as a polymer membrane material has the potential to suffer from creep and fatigue.

A magnetic micro-generator with a planar Cu coil and a micromachined spiral membrane is presented in [62]. A vibratory magnet is sputtered on the bottom of the spiral membrane using a sputtering process. The reported size is $0.45\,cm^3$. The generator is capable of producing maximum power of $100\,\mu W$ and a voltage of 40 mV, which are induced experimentally from excitation at 60 Hz with unreported acceleration level.

Reference [63] describes the development and the testing of a new laterally cantilever-based wound coil moving between a set of PMs. A copper coil with 600 turns is attached to a paddle supported by a micromachined beam cantilever, as shown in Figure 2.12. A housing of two perspex chips was constructed to accommodate the NeFeB PMs. The structure was designed to oscillate laterally, cutting the magnetic field to produce electric power. A total generator size of $100\,mm^3$ produces $0.1\,\mu W$ of power at 1.6 KHz with a 0.4 g vibration source. As reported in [64], the same structure produced $0.148\,\mu W$ at a 8.08 kHz resonant frequency and a $3.9\,m/s^2$ acceleration. This design suffers from high parasitic damping between the copper wires and the housing, which in turn, leads to a very small amount of generated power. An improved design using an electrodeposited copper coil rather than the wound coil was tested, as described in [64]. A $2\,\mu m$ copper seed layer was sputtered on the paddle surface and then a mold $10\,\mu m$ thick was spun, patterned

and developed before the electrodeposition. A 65-turn coil with a silicon paddle resulted in a total oscillating mass of 0.014 grams. The micro-generator generated a maximum power of 23 nW on a load of 52.7 Ω for an acceleration of 9.8 m/s^2, at a resonant frequency of 9.83 kHz. It should be recognized that in both these designs the generated power is very small due to the parasitic damping and small moving mass, which directly affects the amplitude of the power generated and the level of the required excitation frequency.

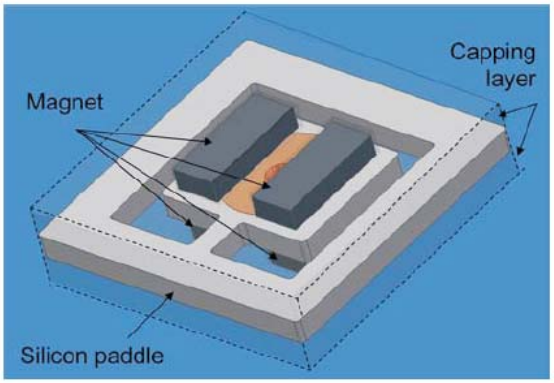

Figure 2.12: Micromachined moving coil vibration-based electromagnetic MPG [63].

Lastly, in [65], a moving NeFeB PM attached to a micromachined spiral copper spring that oscillates with respect to a two-layer fixed micromachined spiral copper coil when a sinusoidal excitation is applied. Experimental results show that the prototype micro-generator can generate an open-circuit voltage of 60 mV AC peak to peak with 121.25 Hz input frequency and an acceleration of 1.5 g. Because the generator was tested with an open circuit, no generated power was reported.

Although the previous devices show the feasibility of micro-scale EMPGs, still more research and investigation are required in order to develop a fully integrated magnetic generator. Permanent magnet integration; permanent magnet patterning and microfabrication; and the development of soft magnetic materials, e.g., ferrite, are the most important challenges in the production of EMPGs by means of low-cost batch fabrication processes.

2.3.5 Comparison of the vibration-based MPGs

Each transduction mechanism discussed above has advantages and disadvantages. This section presents a comparison of the three transduction mechanisms.

2.3.5.1 Piezoelectric Transduction

The piezoelectric transduction mechanism represents the simplest approach to convert mechanical vibration energy to electrical energy without complicated geometries or structures. Many piezoelectric materials are available, in the form of either ceramics or films. Thin-film micromachined piezoelectric elements are being developed as well. However, deposited piezoelectric thin films have a poor coupling coefficient [8] which directly decreases the power generated. In addition, although the generated voltage level is reasonable, i.e., $> 5\,\mathrm{V}$, the output current is usually very small, in the order of n Amp to few 10s of μAmp, because its output impedance is typically very high (>100 KΩ) [11].

2.3.5.2 Electrostatic Transduction

The electrostatic transduction mechanism is the approach that can most easily be implemented in the MEMS-scale devices due to the well-known fabrication technology used with variable capacitors, i.e., in-plane and out-of-plane capacitors. In addition, the fabrication techniques are compatible with CMOS technology, which may lead to a fully integrated VBMPG with the sensor and the microelectronics included on the same chip. However, it is the most complicated vibration energy conversion approach since it needs an external power supply to initiate its operation: either a battery or an electret element. The microfabrication of electrets could represent a significant challenge with respect to this kind of harvesters. The voltage generated is also very high, $> 100\,\mathrm{V}$, which again, may restrict its applicability in low-voltage-circuit environments. The output current is very low, which requires a

special circuit design. When the capacitors are designed and fabricated, particular care must also be taken into account in order to reduce the effect of the parasitic capacitors and to avoid stiction or shorting of the electrodes.

2.3.5.3 Electromagnetic Transduction

The electromagnetic transduction mechanism is the most well-known approach since it has been used in electrical power generation for many years. a variety of configurations have been designed, implemented, and tested. The voltage induced is below 1 V, but output currents are large, i.e., hundreds of μAmp to few 10s of m Amp. To provide high field density, high quality, and very inexpensive rare earth permanent magnates are available. However, micromachined permanent magnets are still in the development phase, and such machining processes are also incompatible with current CMOS processes. Planar magnets still provide relatively low magnetic properties in comparison with currently available bulk magnets. The limited number of planar deposited coils also limits the amount of induced voltage. Both the low magnetic field density and the low number of coil turns result in a low electromechanical coupling coefficient, which in turn, reduces the amount of power generated.

In conclusion, it was reported in [66] that for low-frequency applications, piezoelectric generators offer a wider operating range than electromagnetic generators. However, as the size increases, electromagnetic generators outperform piezoelectric generators and for high-frequency applications, electromagnetic generators have the highest power density.

At this point, it should be mentioned that a generator is designed so that its natural frequency matches the environmental excitation frequency; however, unfortunately, even minute departures from the generator's resonant frequency produce a significant drop in the power levels generated, which highlights the importance of designing a wideband MPG. The following section emphasizes on the most signifi-

cant research in the field of wideband, or broadband, vibration energy harvesters.

2.4 Wideband Vibration Energy Harvesters

This section discusses different techniques for increasing the operating frequency bandwidth of VBMPGs. The main approaches to this problem are based on two different techniques:

- *Multifrequency cantilever array.*
- *Resonance frequency tuning.*

The following subsections present the most significant work with respect to each of these techniques along with the main advantages and disadvantages.

2.4.1 Multifrequency Cantilever Array

Using an array of cantilevers that have a slightly different resonant frequency from one another results in an overlapping frequency spectrum, with the peak powers at close but different frequencies. The adjustment of the resonant frequency can be achieved by using either identical cantilevers and different masses, or identical masses and different cantilever dimensions. connecting the multifrequency cantilever array in series widens the frequency operating band and increases the power level of the overall system to a specific limit, which is determined by how far the resonant frequencies are from each other. The phase shift between the generated signals is the main factor that destroy the overall output signal. The maximum power is smaller than that produced when all the cantilevers are tuned to the same frequency but over a wider band.

In [67] and [68], a multifrequency MEMS-based electromagnetic MPG is presented. The generator consists of multiple cantilevers with different resonant fre-

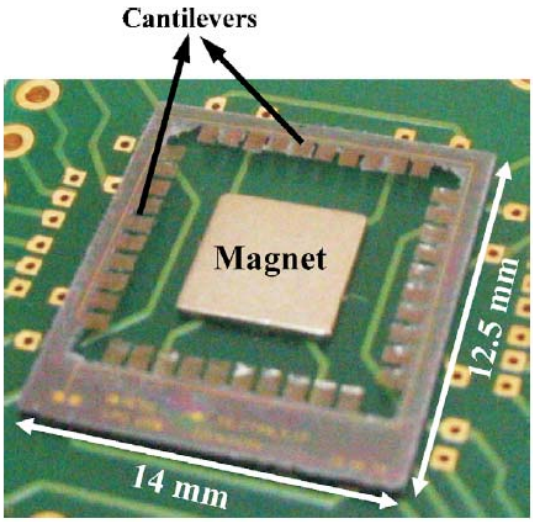

Figure 2.13: Multifrequency, micromachined moving-coil vibration-based EMPG [68].

quencies (different beam lengths). Identical coils have been deposited on the cantilevers. An NdFeB permanent magnet has been fixed in the center of the chip in order to provide the magnetic field necessary for the transduction as shown in Figure 2.13. The load voltage of one cantilever is measured as 3.5 mV; when 40 beams are connected in series, the total load voltage is about 18 mV, with an output power of 0.4 μW over a frequency band of 300 Hz. Although the operating frequency band is fairly large, the output power is only less than 2% of the output power if all the cantilevers are tuned to the same frequency. In addition, the reported excitation acceleration level is very high, e.g., $\approx$49 g.

In [69]-[72], the analysis and modeling of a multifrequency piezoelectric cantilever array are presented. The author showed the possibility of widening the frequency bandwidth by utilizing mechanical band-pass filters. The mechanical coupling effect of the cantilevers was taken into consideration; however, the signal distortion due to electrical coupling that stems from connecting the generated signals directly in series, was not addressed. The mathematical models were also not verified experimentally.

A multifrequency array similar to the one described in [72] is reported in [73]. The generator is composed of an array of three bimorph cantilevers with different resonant frequencies (using different masses). To avoid the destructive effect created by the series connection, the generated voltage of each cantilever is rectified to a DC voltage before they are added together. Thus, although the generators are not working in phase, their voltages are summed algebraically. The resonant frequencies of the cantilevers are adjusted using the appropriate tip masses to be 113 Hz, 183 Hz, and 281 Hz with maximum power of 89 μW, 57 μW, and 57 μW, respectively, if each generator is excited with its own natural frequency. To validate this concept, a capacitor of 1.5 n F was charged to 7.7 V first by exciting only the second cantilever alone at an excitation frequency that matches its natural frequency, i.e., 183 Hz with an excitation level of 1 g. Then, the whole system was used to charge the same capacitor to the same voltage level. It was found that the time taken to charge the capacitor from the whole system is almost half the time taken to charge it from the second cantilever alone, which reflects the fact that the effectiveness of overall energy conversion is an improvement over the case of a single converter. Although this approach overcomes the destruction of the generated signal when the outputs of the cantilevers are connected in series, it requires more complicated systems, and additional cost because the addition of a rectifying circuit to each cantilever, which will be associated with more losses. If there is a large number of cantilevers, it will therefor not be a realistic solution. It is also inconvenient to be used with electromagnetic MPGs because the voltage generated is too small to be conditioned.

Another approach that adapts the same transduction mechanism as the previous one is presented in [74]. The three piezoelectric cantilevers were adjusted to resonate at different but close frequencies. It was found that the operating frequency band covers 226 Hz-234 Hz. The system was excited at a frequency of 229 Hz, and the generated voltages of the cantilevers were 2.01 V, 1.64 V, and 1.606 V. The DC

output voltage after direct serial connection, with only one rectifier circuit, was about 2.51 V with maximum power of 3.15 μW, which is still less than the algebraic summation of the three voltages due to the phase shift of the generated signals. If the three signals are rectified before being accumulated, then the DC voltage will be 3.93 V with maximum power of 3.98 μW, which represents an improvement in the power provided because the destructive effect is avoided.

2.4.2 Resonance Frequency Tuning

The resonance frequency of a device can be tuned by altering either the mass or the stiffness of the oscillating structure; however, it would be challenging to alter these parameters while the device is operational. This section discusses methods of tuning the MPG's natural frequency, which can be classified as mainly active or passive resonance frequency tuning methods, depending on whether the tuning technique consumes energy (active) or not (passive).

2.4.2.1 Active Resonant Frequency Tuning

In [75], a novel method based on applying an axial load on a piezoelectric bimorph to tune its resonant frequency is demonstrated and validated. The author chose to apply compression rather than tensile axial loads in order to avoid the problems that may arise from the brittle nature of piezoelectric ceramics. Applying an axial compression load on a piezoelectric bimorph was found to reduce its natural frequency, which can be considered a softening effect. The structure examined consists of a proof-mass attached by means of a screw and nut to the center of a brass shim that is sandwiched between two piezoelectric films. An axial preload was applied using a differential micrometer drive mounted at one end of the structure with a force sensor mounted on the other end to measure the applied force. Data were measured for two prototypes that have the same bimorph flexure but

different masses, i.e., 7.1 grams and 12.2 grams, at an acceleration level of approximately 1 g. For the 7.1 grams proof-mass, the resonant frequency of the MPG was reduced from about 250 Hz to about 200 Hz, a reduction in the resonant frequency of about 24 %. However, for the 12.2 grams proof-mass, the resonant frequency of the MPG was reduced from about 190 Hz to about 160 Hz, a reduction in the resonant frequency of about 19 %. The device's coupling coeffecient was found to increase from an avearge of 0.367 with a preload of 8 N to an average of 0.461 with a 64 N preload. On the other hand however, there was a trend for the generated power to be reduced as the resonant frequency decreases because the mechanical damping, which represents pure losses, increases with an increasing axial preload. Both designs failed at an axial load of more than 65 N. In this technique, the preload must be changed manually every time the excitation frequency changes; otherwise, a closed-loop controller and an actuator are required so that it is a self-tunned device. Adding more electronics, such as a sensor and actuator, applies an extra drain on the net power produced and, the system must be designed in such a way that some power will survive after all losses are taken into account. In addition, the authors used an optimum resistive load for each optimized operating frequency, which is not easy to achieve in a real case because the load is always fixed.

A tuning technique similar to the one previously discussed is presented in [76]. The kinematic origin of stiffness modification adopts a pre-displacement adjustment rather than a preload compression adjustment. The system is made up of two sets of two circular bimorphs that consist of PZT-5A and brass shims used as the plate elements. The plates in each pair are connected to each other along their outer perimeters, and the centre of one plate is rigidly attached to an external housing while the centre of the other plate is attached to the moving mass. The outer housing can move up and down to allow pre-displacement adjustments to be applied to the bimorph flexure. Using a mass of 150 grams and as a result to applying pre-displacement of the housing, the resonant frequency was continuously

changed from 56 Hz to 62 Hz over a 0.5 mm displacement variation range. The amount of power generated for each resonant frequency was not reported. This design needs an external force along with a controller so that the displacement on the outer housing can be adjusted in order to tune its resonant frequency.

Another resonance frequency tuning technique based on attractive and/or repulsive magnetic forces is discussed in [77]. Applying an attractive magnetic force to a vibrating device causes its natural frequency to shift to a lower value and vice versa. In that work, the author used four permanent magnets: two magnets fixed on a piezoelectric cantilever tip and the other two magnets fixed to the device's enclosure just above and below the moving magnets. The cantilever is anchored to a slide that can move up and down between the fixed magnets in order to change the vertical position of the cantilever with respect to the fixed magnets. Additional stiffness arises from the magnetic field established between the fixed and moving magnets, which leads to the altering of the resonant frequency to a higher or lower value than the original resonant frequency according to the kind of magnetic force,i.e., repulsive or attractive force respectively. An adjustment of two piezoelectric layers sandwiched between three electrodes with an original resonance frequency of 26.2 Hz was tested at 0.82 g. When the vertical displacement of the cantilever was tuned, the device was capable of providing power in the range of 240 -280 μW over a frequency range of 22 -32 Hz. Tuning the structure to a frequency lower than 22 Hz was limited by the collapse between the fixed and moving magnets. In every test, two manual adjustments were required: the vertical position of the cantilever and the optimal resistance load. Closed-loop circuits with a linear actuator are required in order to change both the position and the load, which again places severe limitations on the efficiency of implementing that type of tuning because the control circuits along with the actuator may consume more power than is generated.

The same research group presented in [78] another design for improving the power density of the system. The system is composed of two single degree of

freedom piezoelectric cantilevers are coupled by means of either an attractive of repulsive magnetic force; in this way the resonant frequency is tuned. One of the cantilevers is fixed and the other moves vertically; the distance between them controls the tuning of the resonance frequency. The cantilevers were originally designed to resonate at 22.5 Hz, and a total power of 320 μW was measured from both of them. When an attraction force is applied between them and the vertical distance of the moving cantilever is changed, the resonant frequency of the fixed beam shifts from 22.5 Hz to 32 Hz, whereas the power output from both beams is recorded at each of the tuned resonance frequencies of the fixed cantilever beam and was found to decrease from 320 μW to 200 μW over this frequency range. When a repulsive force is applied, it was found that the resonant frequency of the fixed beam shifts from 23.5 Hz to 34 Hz, whereas the power output from both beams as recorded at each of the tuned resonance frequencies of the fixed cantilever beam and found to decrease from 320 μW to 200 μW over this frequency range. In each step, the optimal load was applied by changing the amount of the resistive load. In addition to the drawbacks listed for the former design, a phase difference exists between the generated voltage of each beam: almost 170 degrees. This difference results in a destructive effect on the total signal generated if the two output signals are connected in series. To avoid this effect, a conditioning circuit that converts each signal to a DC signal is required before they are summed, which increases the amount of energy lost and leads to decreased efficiency.

2.4.2.2 Passive Resonant Frequency Tuning

In [79] and [80] a nonlinear compliance is used to cause the MPG to respond to broadband frequency variations. The MPG consists of a magnet attached to a cantilever that moves with respect to a coil fixed on a laminated iron core in order to increase the flux density in a very small airgap. As a result of this small airgap, significant nonlinear compliance is added to the linear compliance of the cantilever in

order to produce a linear and a cubic nonlinear system. Such a phenomenon causes the nonlinear frequency response of the MPG to be folded over while sweeping up the frequency, while the MPG responds to the down sweep of the frequency with another curve, which represents a hysteresis in the response. The system showed an up-sweep bandwidth of 27 Hz and a down-sweep bandwidth of approximately 15 Hz. This design suffers from high nonlinearity, which causes the system to be very close to unstable behavior. Another issue is that it must be used in environments with high level of vibration in order to overcome the strong force between the stator and the moving magnetic circuit. In addition, the mechanical parameters of the MPG cannot be modified to meet any modification that occurs in the surrounding environment.

Recently, harvesting energy from vibrations with multiple frequencies was discussed in [81]. The structure consists of three permanent magnets attached to an acrylic beam. In opposite to each magnet, a printed coil with 10 turns is placed on a substrate using the PCB technology. The authors claim that energy can be harvested under the first, second, and third vibration resonant modes of 369 Hz, 938 Hz, and 1184 Hz respectively. The maximum output voltage and power from the first and second modes are 1.38 mV and 0.6 μW, 3.2 mV and 3.2 μW respectively for an excitation level of 14 μm. Although the authors showed the feasibility of harvesting energy from multiple frequencies, many design considerations were missed. First, at the second mode, the voltage generated from the first and third coils are 180 degrees out of phase, which requires the implementation of special circuitries in order to avoid signal destruction. Second, the voltage generated at the third mode is too low to be utilized, i.e., 0.0012 mV. Finally, the acceleration used was high, 0.76 g, and the nonlinearity effect that stems from the clamped-clamped supporting beam was not taken into account.

2.5 Summary

This chapter has presented a literature review of alternative power sources for wireless sensor networks. Potential power sources that use a variety of different transduction mechanisms were reviewed, followed by a detailed study of the authors' research on vibration-based energy harvesters, with, a special focus on electromagnetic-based energy harvesters, or micro-power generators. an extensive survey of all work conducted in the area of frequency broadband, or wideband, operation was provided, which included the advantage and drawbacks of each system developed.

Chapter 3

Basic MPG Mathematical Model

This chapter provides a basic mathematical analysis of inertial or vibration-based MPGs. A general overview of VBMPG system is first presented. Then the equation of motion of a mass-spring-damper model with different MPG's resonant to vibration frequency ratios is extracted . The maximum extracted power occurs when the frequency ratio is 1. Such analysis is used to derive the power equations at the end of this chapter.

3.1 General analysis of Vibration based MPG's

The system of vibration-to-electric energy converter/transducer is shown in Figure 3.1 [27]. The ambient vibration energy existing in the environment of a microsystem is coupled onto a resonator, i.e., a spring-mass-damper system. Some of this energy is lost in viscous and/or friction damping losses, and the rest is converted to electric energy by the electromechanical transducer. Power electronics is then used to condition the output power before it supplies the electric load or is stored in an energy reservoir.

The system shown in Figure 3.1 can be physically modeled as a mass-spring-damper system, as shown in Figure 3.2. It consists of a seismic mass m attached at

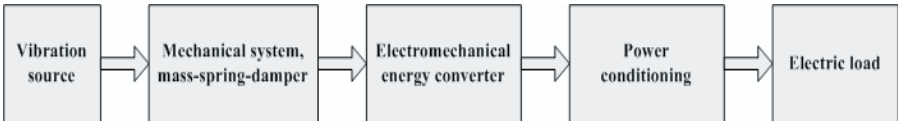

Figure 3.1: Overview of a vibration-to-electric energy converter.

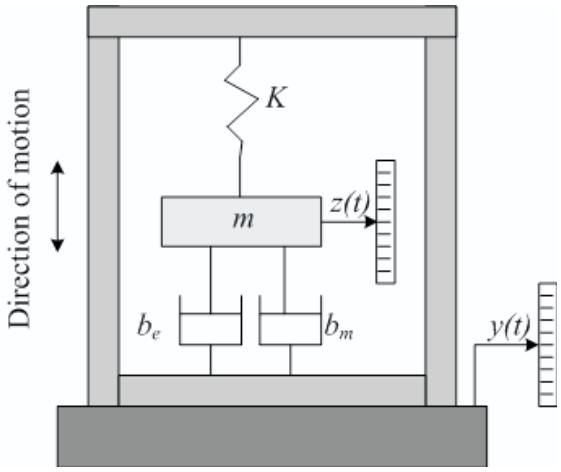

Figure 3.2: Mass-spring-damper model for vibration-based MPGs.

one end point to the generator's housing frame by a spring that has a stiffness K. Mechanical and electrical damping systems, as will be discussed later, damp the motion of the seismic mass within the housing frame. The mechanical and electrical motion dampers are symbolized by dashpots with damping coefficients of b_m and b_e, respectively.

Considering a seismic mass whose housing frame experiences a displacement motion $y(t)$, and let the relative displacement motion between the mass and the housing frame be $z(t)$. The motion of the seismic mass with respect to a fixed frame in space is then $z(t) + y(t)$, and its acceleration causes a force of $m(\ddot{z}(t) + \ddot{y}(t))$. The force applied by the mass to the spring and dashpots assembly is thus $-m(\ddot{z}(t) + \ddot{y}(t))$, the force applied by the spring is $-Kz(t)$, and the force applied by the damper is $-(b_m + b_e)\dot{z}(t)$. The equation of motion can then be written as follows:

$$-m\frac{d^2(z(t) + y(t))}{dt^2} - b_t\frac{dz(t)}{dt} - Kz(t) = 0 \tag{3.1}$$

where b_t is the total damping coefficient and is equal to $b_m + b_e$.

If equation 3.1 is rearranged,

$$m\frac{d^2z(t)}{dt^2} + b_t\frac{dz(t)}{dt} + Kz(t) = -m\frac{d^2y(t)}{dt^2} \tag{3.2}$$

The input vibration motion $y(t)$ can be then assumed to be sinusoidal and can be given as $Y_{max}cos(\Omega t)$, where Ω is the angular frequency. The response of the generator's seismic mass can be defined by

$$z(t) = Z_{max}cos(\Omega t + \Phi) \tag{3.3}$$

where Z_{max} and Φ are defined as follows:

$$Z_o = \frac{Y_{max}(\frac{\Omega}{\omega})^2}{\sqrt{(1-(\frac{\Omega}{\omega})^2)^2 + (\frac{2\zeta_t\Omega}{\omega})^2}} \tag{3.4}$$

$$\Phi = \tan^{-1}\left(\frac{2\zeta_t\frac{\Omega}{\omega}}{1-(\frac{\Omega}{\omega})^2}\right) \tag{3.5}$$

where ζ_t is the total damping ratio and ω is the structure's resonant frequency.

To determine the system's response to different frequency ratio values, $y(t)$ and $z(t)$ are replaced in equation 3.2 to get

$$Z_{max}cos(\Omega t - \Phi + \pi) + \left(\frac{b_t Z_{max}}{m\Omega}\right)cos(\Omega t - \Phi + \frac{\pi}{2}) + \left(\frac{KZ_{max}}{m\Omega^2}\right)cos(\Omega t - \Phi) = Y_{max}cos(\Omega t) \tag{3.6}$$

Now, the following three cases can be considered

- If $\Omega/\omega << 1$, the first and second terms of the left-hand side of equation 3.6 are negligible with respect to the third term, and $\Phi = 0$; hence,

  $$Z_{max} = \frac{m\Omega^2 Y_{max}}{K} = \frac{acceleration}{\omega^2}$$

  In this region, the device is working as an accelerometer to measure the level of acceleration of the excitation vibration.

- If $\Omega/\omega >> 1$, the second and third terms of the left-hand side of equation 3.6 are negligible with respect to the first term, and $\Phi = \pi$; hence,

$$Z_{max} = Y_{max}$$

  In this region, the device is working as a vibrometer to measure the vibration level.

- If $\Omega/\omega = 1$, the first and third terms of the left-hand side of equation 3.6 are equal and cancel each other, and $\Phi = \frac{\pi}{2}$; hence,

$$Z_{max} = \frac{Y_{max}}{2\zeta_t} \tag{3.7}$$

  In this region, the device's stroke is magnified by dividing the excitation source amplitude, i.e., Y_{max}, by the damping ratio of the system, which is a small fraction in most cases. As a result, it is preferable to operate the MPG in this region, i.e. when its resonant or natural frequency matches the excitation frequency, in order to generate an appreciable amount of power.

It can be concluded that the response of the generator's mass to the input vibration displacement is highly dependent on the ratio between the excitation frequency and the resonant frequency of the mass-spring system. As is shown in the next section, the power generated is linearly proportional to the generator's maximum mass displacement, which means that the higher the displacement, the higher the output power. Thus one restriction is that the spring-mass system is designed such that its resonant frequency matches the excitation vibration frequency.

3.2 Power Calculations

To calculate the power output from the MPG, it is necessary to separate the electrical damping system from the mechanical one. Figure 3.2 shows the electromechanical model used to calculate the generated and output power. The energy

converted from the mechanical to the electrical system is the amount of energy dissipated in the electrical damper, whereas the mechanical damper represents pure mechanical loss. The energy dissipated in the electrical damper is determined by first calculating the energy dissipated in b_e per cycle, i.e., E_{cyc}:

$$E_{cyc} = 4 \int_{z=0}^{z=Z_{max}} b_e \dot{z} dz \tag{3.8}$$

or

$$E_{cyc} = b_e \int_{0}^{T} (\dot{z})^2 dt \tag{3.9}$$

where T is the time period of the input vibration frequency. Substituting from equation 3.4 into equation 3.3 and then substituting into equation 3.9 results in:

$$E_{cyc} = \frac{2\zeta_e m Y_{max}^2 \Omega^2 \pi \left(\frac{\Omega}{\omega}\right)^3}{\left[1 - \left(\frac{\Omega}{\omega}\right)^2\right]^2 + \left[\frac{2\zeta_t \Omega}{\omega}\right]^2} \tag{3.10}$$

where ζ_e and ζ_t are the electrical and total damping ratios, respectively.

Thus the power dissipated in the electrical damper,P, is given by

$$P = \frac{2\zeta_e m Y_{max}^2 \Omega^2 \pi \left(\frac{\Omega}{\omega}\right)^3}{\left[1 - \left(\frac{\Omega}{\omega}\right)^2\right]^2 + \left[\frac{2\zeta_t \Omega}{\omega}\right]^2} \times \frac{\Omega}{2\pi} = \frac{m Y_{max}^2 \zeta_e \Omega^3 \left(\frac{\Omega}{\omega}\right)^3}{\left[1 - \left(\frac{\Omega}{\omega}\right)^2\right]^2 + \left[\frac{2\zeta_t \Omega}{\omega}\right]^2} \tag{3.11}$$

Figure 3.3 shows the dependency of the output power on the input vibration frequency for different damping ratios, ζ_t. It is shown that the maximum power level depends on both the damping ratio and the frequency ratio, $\frac{\Omega}{\omega}$. The lower the damping ratio, the higher the maximum power; however, the half power bandwidth will also be proportionally narrower. A common aspect for all cases is that maximum power occurs when the excitation frequency matches the resonant frequency, and just a small deviation in the excitation frequency from the resonant frequency results in a dramatical drop in the power generated.

When the excitation frequency matches the resonant frequency, i.e., $\frac{\Omega}{\omega}$, equation 3.4 can be rewritten as follows:

$$Z_{omax} = \frac{m \Omega Y_{max}}{b_e + b_m} \tag{3.12}$$

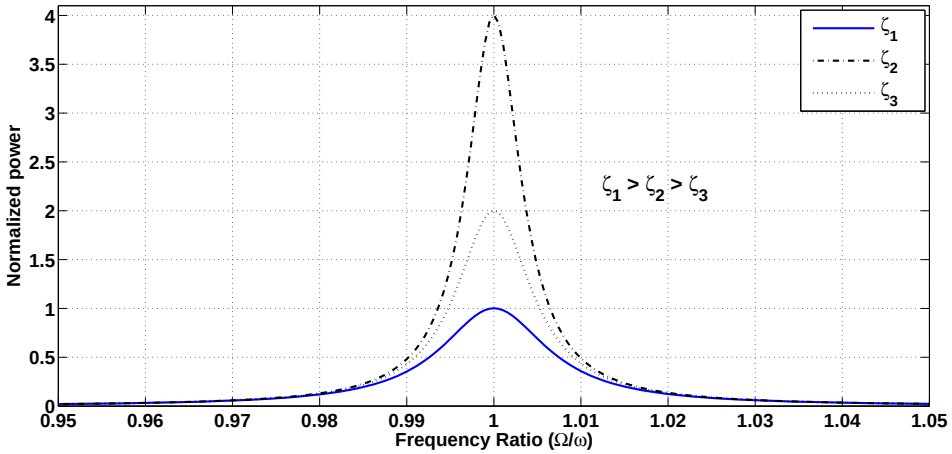

Figure 3.3: Frequency response of power generated for different damping ratios.

where Z_{omax} is the maximum stroke at resonance. Substituting from equation 3.12 into equation 3.11 results in

$$P_{max} = \frac{1}{2}\frac{b_e}{b_e + b_m} m\omega^3 Y_{max} Z_{omax} \tag{3.13}$$

The magnitude of the input vibration acceleration A is $\omega^2 Y_{max}$. Finally, the maximum converted power can be expressed as follows:

$$P_{max} = \frac{1}{2}\frac{b_e}{b_e + b_m} m\omega A Z_{omax} \tag{3.14}$$

An interesting point that can be noticed from equation 3.14 is that P_{max} is optimized when the electrical damping coefficient equals the mechanical damping coefficient, i.e., $b_e = b_m$, which could be a challenging restriction, especially for small structures where the value of b_m is very small.

3.3 Summary

This chapter has reviewed the basic model of the VBMPGs. It is worth mentioning that in both electrostatic and piezoelectric transduction methods, the electrical damping coefficient, b_e, is not linear and affects the dynamics of the total MPG system, which is beyond the scope of this work.

Chapter 4

Linear Electromagnetic MPGs

This chapter introduces the linear model of electromagnetic VBMPGs. Both analytical and numerical models based on the FEA are presented. A standard electromagnetic VBMPG has been built in order to verify the linear model experimentally. Analytical calculations and finite element results are compared to actual measurements from the power generator; conclusions are then drawn from the comparison.

4.1 Linear Model of Electromagnetic VBMPG

The electromechanical model shown in Figure 4.1 is used to achieve the transfer function of the generator system shown in Figure 3.1. The model utilizes electromagnetic transduction mechanism to convert the mechanical vibration energy to electrical energy. In the model, m is the mass of a permanent magnet, L_c is the coil inductance, R_c is the internal coil resistance, R_L is the load resistance, and $v(t)$ is the load voltage.

The electromechanical model is composed of two main systems: mechanical (the mass-spring-damper system) and electrical (the load resistance and the coil's inductance and internal resistance). With an input mechanical force f_m, the mass, which is the permanent magnet in this case, displaces a displacement z relative to

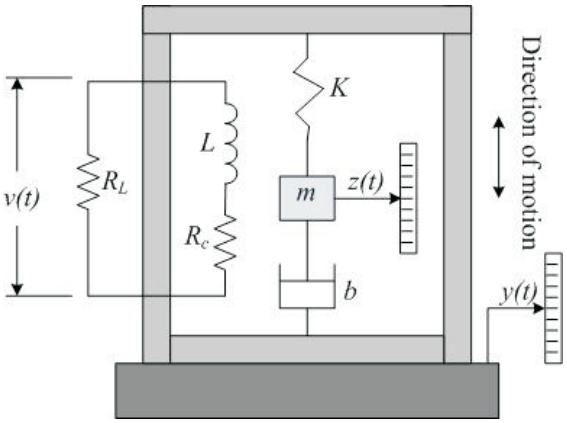

Figure 4.1: Electromechanical model.

the fixed frame and to the coil. The transfer function for this mechanical system can be derived as follows [46]:

$$\frac{Z(s)}{F_m(s)} = \frac{1}{ms^2 + bs + k} \tag{4.1}$$

where $Z(s)$ and $F_m(s)$ are the Laplace transform of the relative displacement and the input mechanical force, respectively.

According to Faraday's law, the voltage induced in the coil wires is $B\ell\dot{z}(t)$, where B and ℓ are the magnetic field density and the total effective conductor length cut by the magnetic field lines, respectively. The behaviour of the electrical system can then be described by the following differential equation:

$$B\ell\dot{z}(t) = L\frac{di(t)}{dt} + (R + R_c)i(t) \tag{4.2}$$

where $i(t)$ is the induced current in the generator's coil.

The current, $i(t)$, can be defined in terms of Ohm's law as follows:

$$i(t) = \frac{v(t)}{R_L} \tag{4.3}$$

where $i(t)$ is the current induced in the generator's coil and $v(t)$ is the output load voltage of the generator. Taking the Laplace transform for both equations 4.2 and 4.3 and then substituting from equation 4.3 into 4.2 results in the following equation

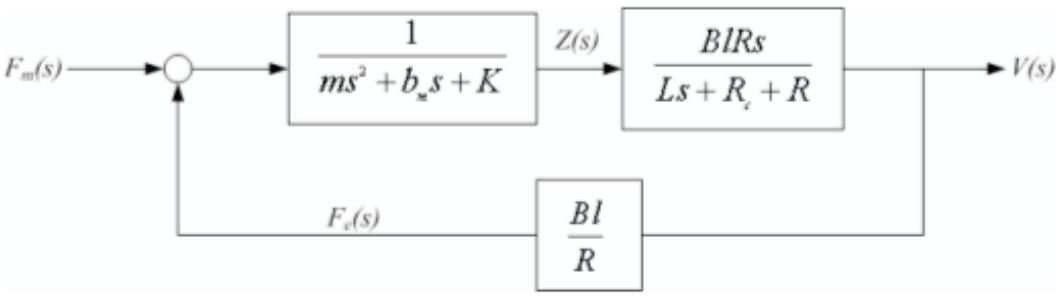

Figure 4.2: Block diagram of the electromechanical model.

representing the transfer function for the relative displacement of the mass to the output voltage:

$$\frac{V(s)}{Z(s)} = \frac{BlR_L s}{Ls + R_L + R_c} \tag{4.4}$$

where $V(s)$ is the Laplace transform of the output voltage.

As the current flows through the coil, another electromechanical force is generated according to the Lorentz force law, f_e, which can be expressed as follows:

$$f_e(t) = B\ell i = (\frac{B\ell}{R_L})v(t) \tag{4.5}$$

The direction of this force is in the opposite direction to the motion, i.e., the damping force. The total force acting on the seismic mass is then $f_m - f_e$. A block diagram for the whole system can be derived, as shown in Figure 4.2 [82].

The transfer function of the whole system can be found as follows:

$$G(s) = \frac{V(s)}{F_m(s)} = \frac{B\ell R_L s}{(ms^2 + b_m s + k)(Ls + R_L + R_c) + (B\ell)^2 s} \tag{4.6}$$

Equation 4.6 can be reduced to a damped second order system if the inductance of the coil is ignored, which is a reasonable assumption since the dimensions of the coil are in the millimeter range [83]. In addition, since the value of the inductance is small relative to the load resistance, the $\frac{L}{R_L+R_c}$ time constant is also small. The transfer function of the whole system can be reduced as follows:

$$G(s) = \frac{V(s)}{F_m(s)} = \frac{B\ell R_L s}{(R_L + R_c)\left(ms^2 + \left[b_m + \frac{(B\ell)^2}{R_L+R_c}\right] s + k\right)} \tag{4.7}$$

where $\frac{(B\ell)^2}{R_L+R_c}$ is the electrical damping coefficient b_e. The load RMS voltage can then be calculated by assuming a sinusoidal input force [82]:

$$|v(t)| = \frac{B\ell\Omega Y_{max}\left(\frac{\Omega}{\omega}\right)^2}{\sqrt{\left(1-\left(\frac{\Omega}{\omega}\right)^2\right)^2+\left(2\zeta_t\frac{\Omega}{\omega}\right)^2}}\frac{R_L}{\sqrt{2}R_L+R_c} \tag{4.8}$$

at resonance, i.e., Ω=ω, the RMS voltage is expressed as,

$$V_o = \frac{B\ell\omega Y_{max}}{2\zeta_t} \tag{4.9}$$

The maximum average output power at resonance can be calculated as follows:

$$P_{\max} = \frac{V_o^2}{2R_L} = \frac{m\zeta_e Y_{\max}^2\omega^3}{4\zeta_t^2} = \frac{1}{2}\frac{b_e}{b_e+b_m}m\omega AZ_{o\max} \tag{4.10}$$

where ζ_e is the electrical damping factor $\frac{\frac{(B\ell)^2}{R_L+R_c}}{2\sqrt{km}}$, and ζ_t is the total damping factor $\frac{\frac{(B\ell)^2}{R_L+R_c}+b_m}{2\sqrt{km}}$. It should be noticed that equation 4.10 matches equation 3.14.

4.2 Model Verification

This section presents a practical electromagnetic VBMPG developed in order to verify the analytical model of the VBEMPG presented in the previous section. First, the physical model is introduced. Second, the stiffness of the cantilever and the density of the magnetic field in the air gap are calculated using the FEA package ANSYS by performing a 3D static structural analysis and a 2D magnetic analysis, respectively. The mechanical damping coefficient, b_m, is then measured in the experimental setup so that it can be inserted into the analytical model in order to verify all the parameters of the prototype that will be used in the analytical model described in the next chapter. Finally, the experimental results and the analytical results are compared together.

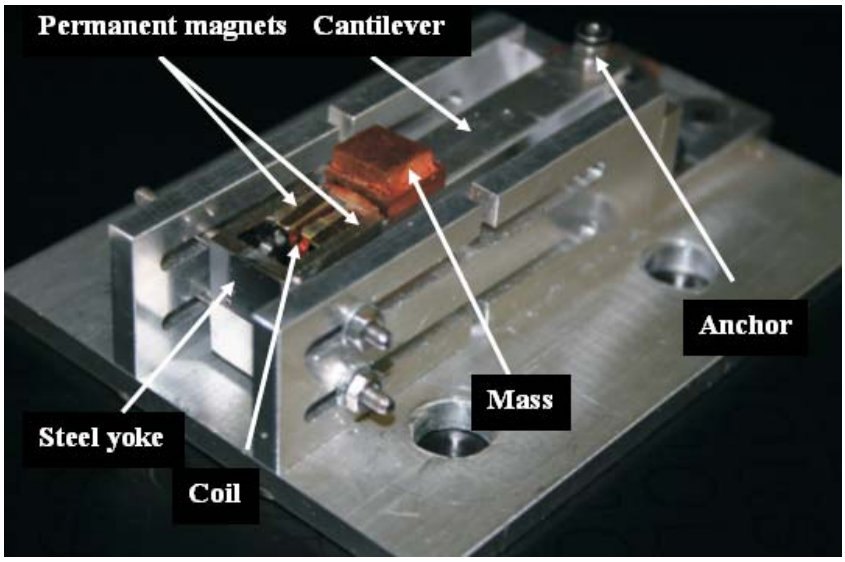

Figure 4.3: The prototype.

4.2.1 Physical Model

Figures 4.3 and 4.4 show a picture as well as top and side view schematics of the prototype. It consists of a seismic mass and a coil supported by a cantilever beam and moving in a magnetic field. The coil has an area of 1 cm^2 and is made of 22 turns of 160μ m copper wire. A system of four permanent magnets, 10 mm$\times$10 mm$\times$3 mm each, maintains the magnetic field in the 4 mm air gap width. The magnets are attached to an external steel yoke in order to increase the flux density in the air gap by providing an easy return path for the magnetic field though the steel yoke. The internal resistance of the coil was measured at 1.2 ohm, and the effective length of the coil is $\ell = 440$ mm. The dimensions and material properties of the prototype are listed in Table 4.1.

4.2.1.1 FE Magnetic Field and Mechanical Analyses

Figure 4.5 shows a nonlinear electromagnetic FEA using the ANSYS software package. It is shown that the magnetic field is not distributed uniformly across the air gap. The analysis also shows that maximum flux density in the air gap is 0.6 Tesla;

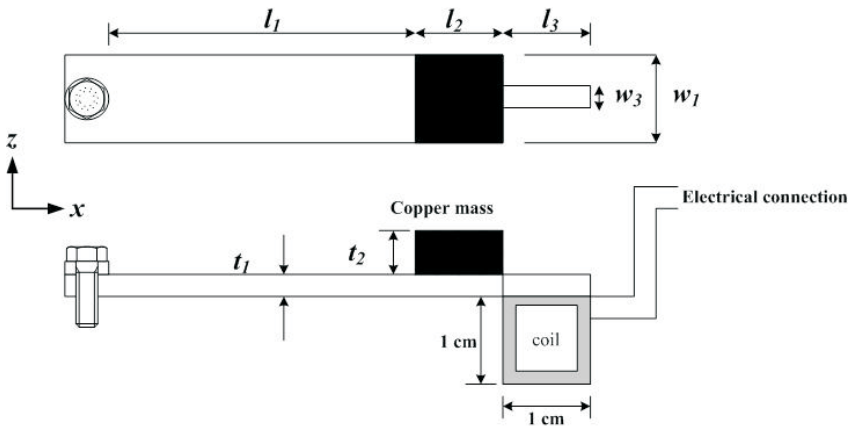

Figure 4.4: Top and side views of the prototype.

Table 4.1: Dimensions and material properties of the prototype.

Parameter	**Description**	**Value**
l_1	Main cantilever length	45.3 mm
l_2	Seismic mass Length	10 mm
l_3	Cantilever tip length	10 mm
w_1	Cantilever & seismic mass width	10 mm
w_3	Cantilever tip width	2 mm
t_1	Cantilever thickness	1.02 mm
t_2	Seismic mass thickness	3.28 mm
ρ_a	Aluminum density	2700 Kg/m^3
ρ_c	Copper density	8912 Kg/m^3
E_a	Aluminum Young's modulus	70×10^9 N/m
r_c	Copper resistivity	$1.7 \times 10^{-8} \Omega$ m

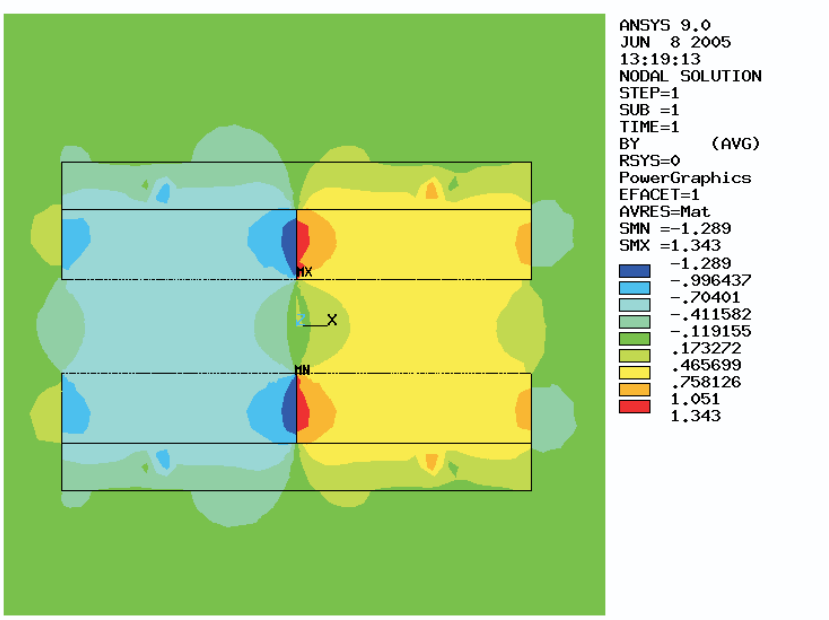

Figure 4.5: Finite element analysis of the magnetic circuit.

however, at the end and in the centre regions the value is lower: about 0.224 Tesla. A nonlinear FEA was performed on a structure having four permanent magnets, each 10 mm × 10 mm × 3 mm, and an air gap of 4 mm. The permanent magnet used in the simulation was Neodymium-Iron-Boron grade N35H with a residual flux of 1.2 T and a coercive force of 950 KA/m [84]. Silicon-steel was used as the soft magnetic material, and its B-H curve was obtained from ANSYS's material library. To validate the FEA results, a magnetometer was used to measure the density of the magnetic field in the air gap: a peak value of $B = 0.57$ Tesla was measured. As shown later in this chapter, due to the magnetic non-uniformity in the air gap, a softening effect occurs when the coil travels large strokes between the magnets, leading to shifting the resonant peak of the voltage generated to the left of the original resonant peak. In addition, the peak voltage is lower than the value expected from the analytical model.

To calculate the linear stiffness of the cantilever , k_1, a 3D static structural analysis was performed in ANSYS . Figure 4.6 shows both the physical and the

finite element model of the cantilever. To determine the stiffness, k_1, a force of 0.1 N was applied to the centre point of the mass attached to the tip of the cantilever and the vertical displacement of this point was then calculated by ANSYS as shown in Figure 4.7. The linear stiffness of the cantilever to be k_1 was calculated to be 1348 N/m. The fundamental natural frequency of the prototype $f = 94.8$ Hz was measured experimentally. Substituting f in the relationship,

$$2\pi f = \sqrt{\frac{k_1}{m}} \tag{4.11}$$

the effective mass of the lumped-mass model as m was determined to be 3.8 grams.

4.2.1.2 Experimental Setup

An electromagnetic shaker was used as a source of base excitations $y(t)$, double-sided adhesive tape was used to attach the MPG to the shaker table, and a resistive load R_L of 2.7 Ω was connected to the coil circuit. To perform a frequency-sweep, the amplitude of the base acceleration was held constant at $\Omega^2 Y = F = 0.1$ g (RMS), while its frequency was swept in the interval $[90.0, 110]$ Hz. The voltage across the load was recorded as the output signal. Figure 4.8 shows the frequency-response curve of the load RMS voltage obtained experimentally using the original prototype. The maximum output power $P = 141\mu W$ occurred at resonance.

The bandwidth at half-power [85]

$$BW = \frac{b_m + b_e}{2\pi m} \tag{4.12}$$

was measured to be 1.4 Hz and the mechanical damping coefficient, b_m was then calculated to be 0.0175 N s/m.

A special aspect of this structure is the fact that the stroke of the moving centre of the coil is larger than the stroke of the centre of the proof mass, which means that equation 4.8 must be multiplied by a factor r_v, which is the ratio between the stroke of the centre of the coil and that of the centre of the mass in order to

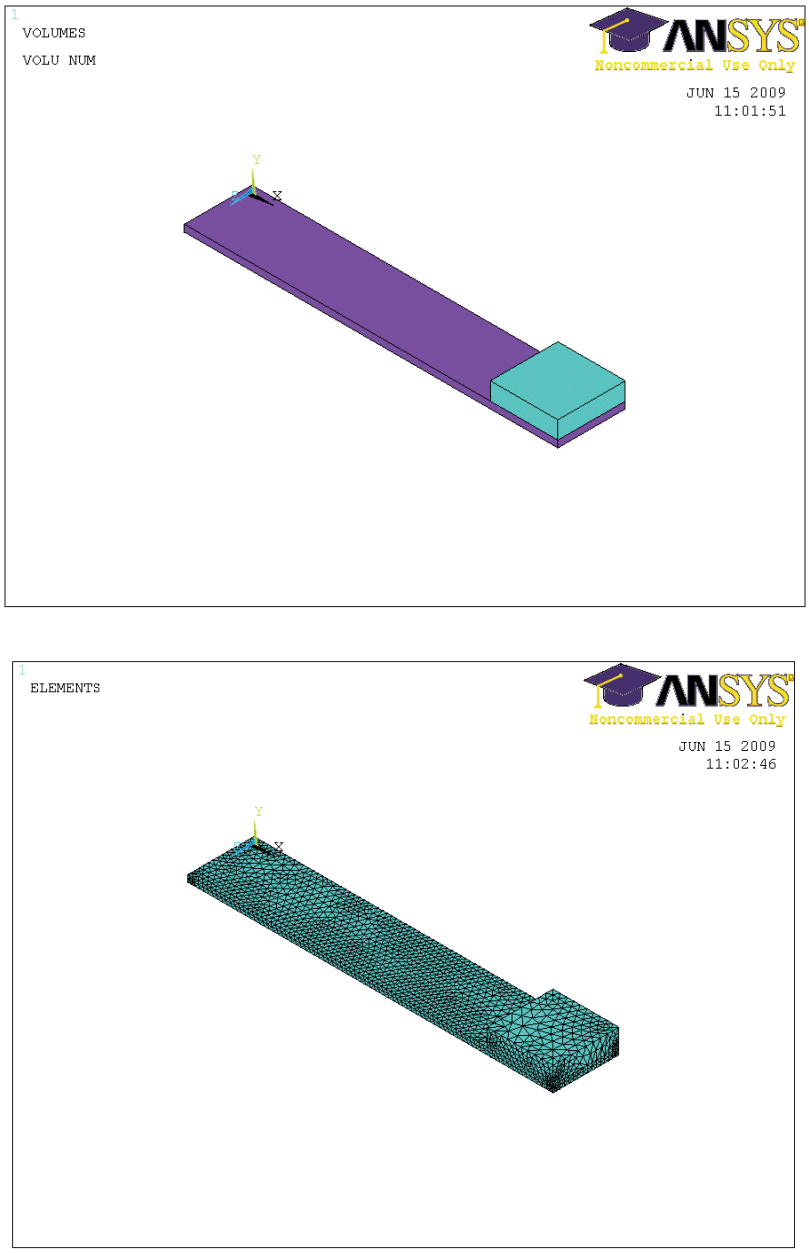

Figure 4.6: Physical and finite element models.

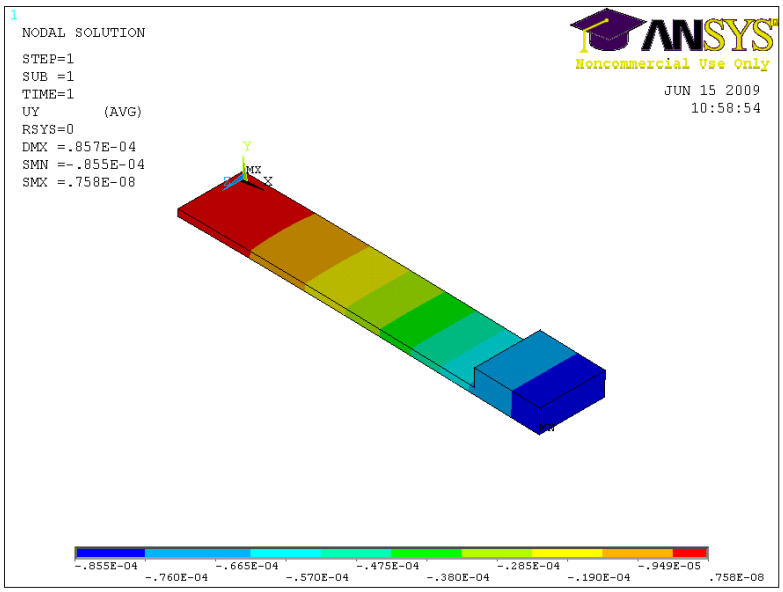

Figure 4.7: Finite element analysis results.

take this discrepancy into consideration. In all cases, the beam oscillates in the first mode of the transverse motion. The shape mode can be obtained by solving the eigenvalue problem of a simple beam with a mass at its tip [86]. Solving the eigenvalue problem results that the ratio r_v is 1.1. Equation 4.8 can be modified as follows:

$$|v(t)| = \frac{B\ell\Omega Y_{max}\left(\frac{\Omega}{\omega}\right)^2}{\sqrt{\left(1-\left(\frac{\Omega}{\omega}\right)^2\right)^2+\left(2\zeta_t\frac{\Omega}{\omega}\right)^2}}\frac{R_L}{\sqrt{2}R_L+R_c}r_v \tag{4.13}$$

The MPG parameters were substituted in equation 4.13 to obtain the frequency-response curve of the RMS output voltage analytically. A comparison of the two curves in Figure 4.8 shows that the analytical results are in good agreement with the experimental results at this excitation level.

The analytical and experimental frequency-response curves were compared at different excitation levels, as shown in Figure 4.9. As the excitation level increases,

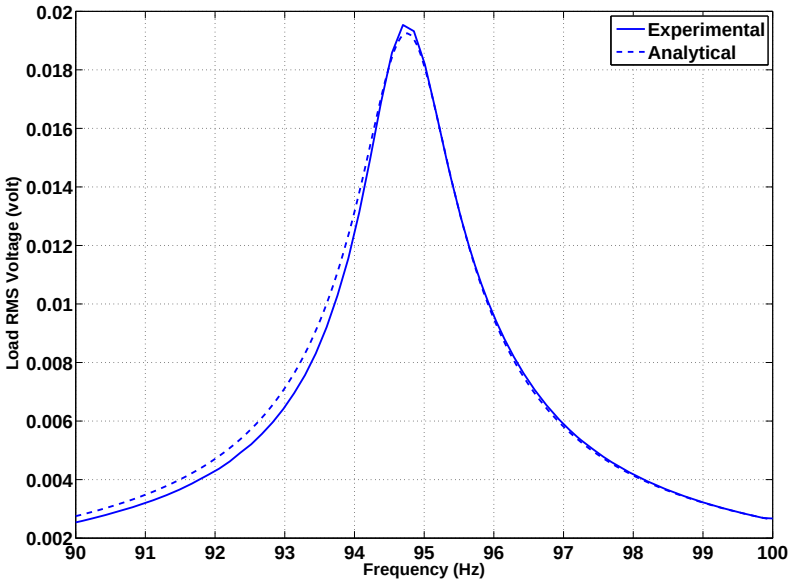

Figure 4.8: Experimental and analytical frequency-response curves of the RMS voltage of the original prototype.

the centre frequency of the experimental curve drifts to the left of the centre frequency of the analytical curve. In addition, the experimental curve bends progressively to the left as the excitation level increases. These results are classical indicators of the presence of a softening-type nonlinearity in the system.

Figure 4.10 shows the measured magnetic field density along the line AB that passes through the centre of the coil. The coil lines cross the magnetic field lines at $z = -5$ and $z = -15$; therefore the density of the field lines encountered by the coil can be approximated as

$$B(z) \approx 0.57 \cos z \approx 0.57 - 0.285 z^2 \tag{4.14}$$

The quadratic nonlinearity in the density of the magnetic field corresponds to a softening-type nonlinearity and explains the experimentally observed shift in the resonant frequency to lower values and the bend to the left in the frequency-response curve with at higher levels of excitation.

The analysis was restricted to small motions that produce less than 0.05 V of

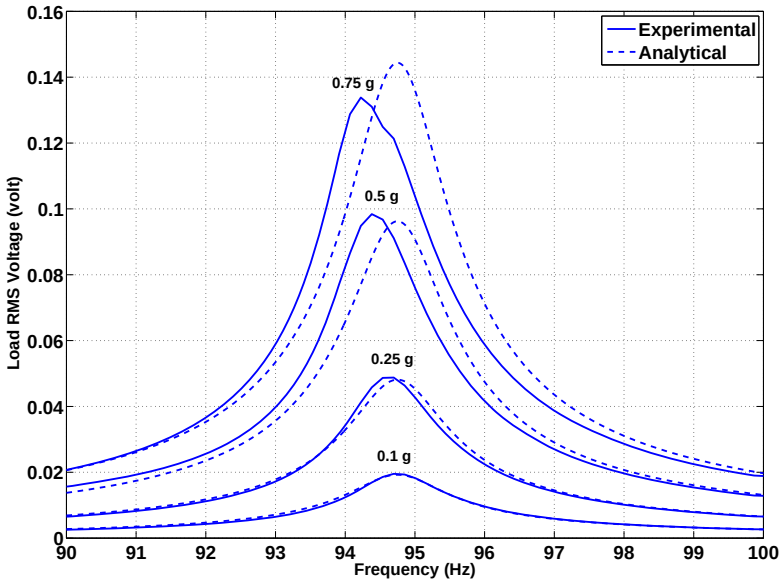

Figure 4.9: Experimental and analytical frequency-response curves at four excitation levels.

RMS load voltage. The results shown in Figure 4.9 indicate that in this regime the effects of nonlinearity on the system response are negligible. The magnetic field density, B, was assumed to be constant at 0.57 T in this domain and the lumped-mass model in equation 3.2 was used to approximate the system response.

4.3 Summary

This chapter has provided an analytical model of electromagnetic VBMPGs. An electromagnetic VBMPG was built and tested in order to validate the analytical model. It was found that the ratio between the centre of the mass and the centre of the coil strokes must be taken into account in order to obtain more accurate results from the analytical model. Both the analytical and the experimental results were compared, and a good agreement was obtained if the motion is restricted to small strokes in order to avoid the nonuniform magnetic field distribution, which leads to

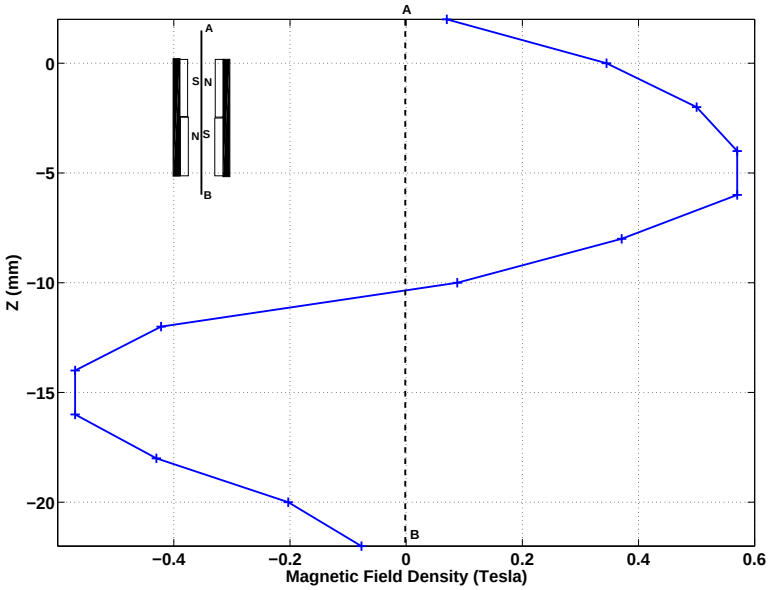

Figure 4.10: Distribution of the density of the magnetic field along line AB.

a softening effect.

Chapter 5

Piecewise-Linear MPGs

This chapter presents a new architecture for wideband MPGs (WMPGs). It replaces a linear oscillator with a piecewise-linear oscillator as the energy harvesting suspension element of the MPG. The prototype of the electromagnetic MPG presented in the previous chapter was modified to accommodate a stopper with adjustable vertical and horizontal positions. This prototype was then analyzed analytically, numerically, and experimentally. It was found that the new architecture increases the bandwidth of the MPG during a frequency up-sweep, while maintaining the same bandwidth in a down-sweep. Closed-form expressions for the response for the modified MPG with the piecewise-linear oscillator are presented and validated experimentally. The simulations showed that under random-frequency excitations, the new MPG collects more energy than the traditional MPG. Finally, a road map is presented for the design of an electromagnetic MEMS-based MPG in order to utilize the main advantages of MEMS structures, such as mass production, low cost, lower energy losses, and high field densities.

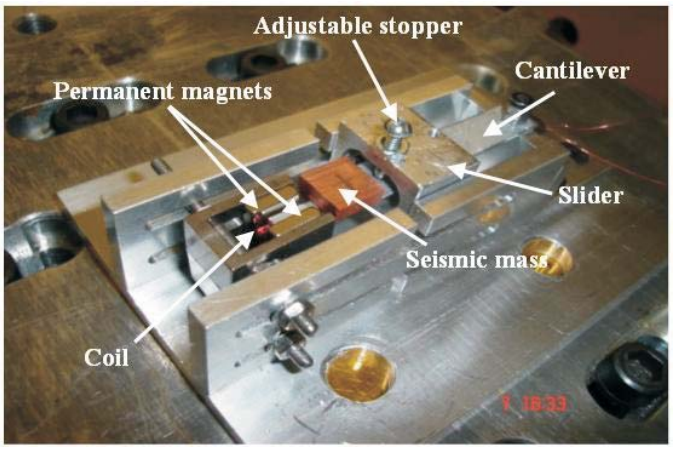

Figure 5.1: Picture of the modified MPG.

5.1 Prototype and Model

Figures 5.1 and 5.2 show a picture and a schematic diagram of the modified MPG, respectively. A slider carries a stopper and moves along a track in order to vary the horizontal position of the stopper l_o while maintaining it at a constant height $h_\circ$ above the beam at rest, as shown in Figure 5.1. As the oscillations z increase, the stopper engages the beam when $z \geq z_\circ$ and changes the effective length of the beam from $(l_1 + \frac{1}{2}l_2)$ to $(l_1 + \frac{1}{2}l_2 - l_o)$. This architecture transforms the harvester from a linear oscillator to a piecewise-linear oscillator. Piecewise-linear oscillators, in which $k_2 > k_1$, exhibit a broad bandwidth in the neighborhood of a natural frequency [87]. It is this behaviour that can exploited to create a wideband MPG.

Acoustic, thermal, frictional, and structural dissipation mechanisms are active during impact and subsequently while the beam and stopper are engaged. To account for bilinear stiffness and additional damping mechanisms, the mechanical restoring F_r and damping F_d forces were modified according to

$$F_r = \begin{cases} k_1 z & z < z_\circ \\ k_2 z + (k_1 - k_2) z_\circ & z \geq z_\circ \end{cases} \tag{5.1}$$

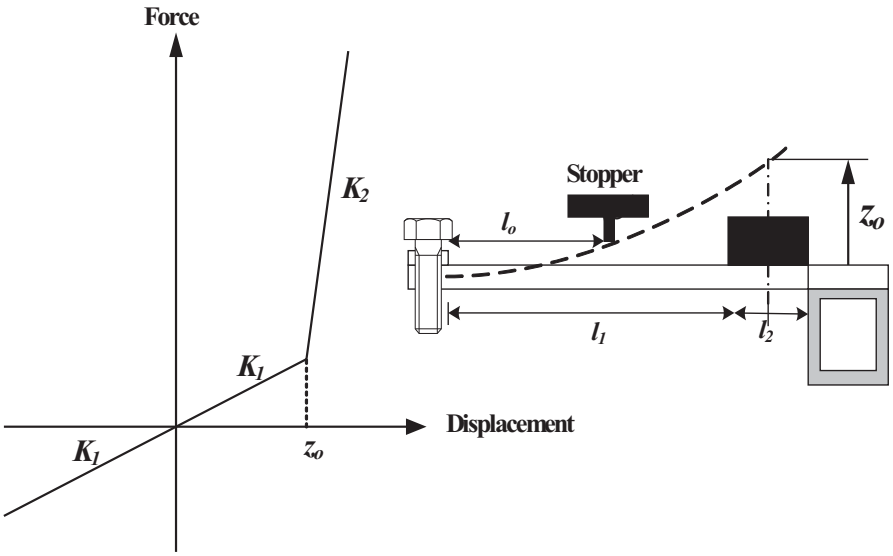

Figure 5.2: Schematic of the modified MPG.

and

$$F_d = \begin{cases} b_1\dot{z} & z < z_\circ \\ b_2\dot{z} & z \geq z_\circ \end{cases} \tag{5.2}$$

where b_1 and b_2 are to be determined experimentally. Therefore, the equation of motion can be written as

$$m\ddot{z} + b\dot{z} + kz = -m\ddot{y} + (k_2 - k_1)z_\circ h(z - z_\circ) \tag{5.3}$$

where $h(z - z_\circ)$ is the Heaviside function; $k = k_1$ or k_2; and $b = b_1$ or b_2, according to the conditions of equations 5.1 and 5.2, respectively. This system has a response identical to that of the linear system, equation 3.2, except when the beam engages the stopper where $z(t) \geq z_\circ$.

The nondimensional variables

$$\hat{z} = \frac{z}{z_\circ}, \quad \hat{y} = \frac{y}{z_\circ}, \quad \hat{t} = \omega_1 t, \quad \hat{\Omega} = \frac{\Omega}{\omega_1}$$

were used to nondimensionalize the equation of motion

$$\omega_1^2 z_\circ \hat{\ddot{z}} + 2\omega_1^2 z_\circ \zeta \hat{\dot{z}} + \omega^2 z_\circ \hat{z} = -\omega_1^2 z_\circ \hat{\ddot{y}} + (\omega_2^2 - \omega_1^2) z_\circ h(\hat{z} - 1) \tag{5.4}$$

where $\omega_1 = \sqrt{\frac{k_1}{m}}$, $\omega_2 = \sqrt{\frac{k_2}{m}}$ and $\omega = \omega_1$ or ω_2 in accordance with the conditions of equation . To simplify the notations, the hats are dropped, which results in

$$\ddot{z} + 2\zeta\dot{z} + r^2 z = -\ddot{y} + (\rho^2 - 1)h(z-1) \tag{5.5}$$

where

$$\begin{cases} r = 1\,, & \zeta = \zeta_1 \quad z < z_\circ \\ r = \rho = \sqrt{\frac{k_2}{k_1}}\,, & \zeta = \zeta_2 \quad z \geq z_\circ \end{cases}$$

An identical stopper can also placed in a symmetric configuration on the other side of the beam. For this research, the architecture discussed above is called a "one-sided stopper" system, and the symmetric configuration is called a "two-sided stopper" system. The dynamics of both systems are examined in the following section.

5.2 System Dynamics

5.2.1 One-Sided Stopper:

The method of averaging was used to obtain a closed-form solution of this equation. A first order approximate solution can be assumed of the form,

$$z(t) \quad = a(t)\sin\phi(t) \tag{5.6}$$

$$\dot{z}(t) \quad = a(t)\Omega\cos\phi(t) \tag{5.7}$$

where $\phi(t) = \Omega t + \beta(t)$. A comparison of equations 5.6 and 5.7 yields the constraint

$$\dot{a}\sin\phi + a\dot{\beta}\cos\phi = 0 \tag{5.8}$$

Substituting equations 5.6 and 5.7 into equation 5.5 results in,

$$\dot{a}\Omega\cos\phi - a\dot{\beta}\Omega\sin\phi = a(\Omega^2 - r^2)\sin\phi - 2\zeta a\Omega\cos\phi - F\sin(\phi-\beta) + (\rho^2-1)h(z-1) \tag{5.9}$$

and solving equations 5.8 and 5.9 for $\dot{a}$ and $\dot{\beta}$ produces

$$\begin{aligned} \dot{a}\Omega = \quad & a(\Omega^2 - r^2)\sin\phi\cos\phi - 2\zeta a\Omega\cos^2\phi + (\rho^2-1)h(z-1)\cos\phi \\ & -F\sin(\phi-\beta)\cos\phi \end{aligned} \tag{5.10}$$

$$\begin{aligned} a\dot{\beta}\Omega = \quad & -a(\Omega^2 - r^2)\sin^2\phi - 2\zeta a\Omega\sin\phi\cos\phi - (\rho^2-1)h(z-1)\sin\phi \\ & +F\sin(\phi-\beta)\sin\phi \end{aligned} \tag{5.11}$$

Since $\dot{a}$ and $\dot{\beta}$ vary slowly with time, their values are assumed to be constant over a period $[-\pi-\phi_s, \pi-\phi_s]$:

$$2\pi\dot{a}\Omega = \int_{-\pi-\phi_s}^{\phi_s} \dot{a}\Omega d\phi + \int_{\phi_s}^{\pi-\phi_s} \dot{a}\Omega d\phi \tag{5.12}$$

$$2\pi a\dot{\beta}\Omega = \int_{-\pi-\phi_s}^{\phi_s} a\dot{\beta}\Omega d\phi + \int_{\phi_s}^{\pi-\phi_s} a\dot{\beta}\Omega d\phi \tag{5.13}$$

where $\phi_s = \sin^{-1}\frac{1}{a}$ is the phase angle when the beam first engages the stopper. Carrying out the integration in equations 5.12 and 5.13 results in the modulation equations

$$\dot{a} = -\tfrac{1}{\pi}(\zeta_1-\zeta_2)(\cos\phi_s + a\phi_s) - \tfrac{1}{2}(\zeta_1+\zeta_2)a + \tfrac{F}{2\Omega}\sin\beta \tag{5.14}$$

$$a\dot{\beta} = \tfrac{a}{4\Omega}\big[(1+\rho^2) + \tfrac{2}{\pi}(1-\rho^2)\phi_s - 2\Omega^2\big] + \tfrac{1-\rho^2}{2\pi\Omega}\cos\phi_s + \tfrac{F}{2\Omega}\cos\beta \tag{5.15}$$

Steady-state periodic solutions correspond to constant a and β, that is, the fixed points $(a_\circ, \beta_\circ)$ of the modulation equations. To find these fixed points, the time derivatives are set to be equal to zero in equations 5.14 and 5.15, producing

$$F\sin\beta_\circ = \tfrac{2\Omega}{\pi}(\zeta_1-\zeta_2)(\cos\phi_s + a\phi_s) + \Omega(\zeta_1+\zeta_2)a \tag{5.16}$$

$$F\cos\beta_\circ = -\tfrac{1}{2}a_\circ\big[(1+\rho^2) + \tfrac{2}{\pi}(1-\rho^2)\phi_s - 2\Omega^2\big] - \tfrac{1-\rho^2}{\pi}\cos\phi_s \tag{5.17}$$

Equations 5.16 and 5.17 can be solved analytically to find the frequency-response equation of the oscillator:

$$F^2 = c_1 + c_2 a_\circ + c_3 a_\circ^2 \tag{5.18}$$

where c_1, c_2, and c_3 are functions of $\Omega, \phi_s, \rho, \zeta_1$, and ζ_2.

Equations 5.18 and 3.2 were used to evaluate the steady-state amplitude of the piecewise-linear oscillator $a_\circ$ and the linear oscillator Z and were then substituted into equation 4.13 in order to generate the frequency-response curves of the RMS voltage of the load, as shown in Figure 5.3, for an acceleration amplitude of $F = 0.1\,\mathrm{g(RMS)}$. The damping ratio during contact, ζ_2, was estimated experimentally to be 0.62 and the stopper height was set to a coil stroke of $z_\circ = 0.189\,\mathrm{mm}$. As a result, the stiffness ratio was set to $\rho^2 = 20$. The stopper height corresponds to a coil stroke amplitude of $\frac{Z_{max}}{\sqrt{2}}$; therefore the stopper is engaged only when the output power exceeds the half-power level $P_e \geq 0.5(P_e)_{max}$ of the linear system.

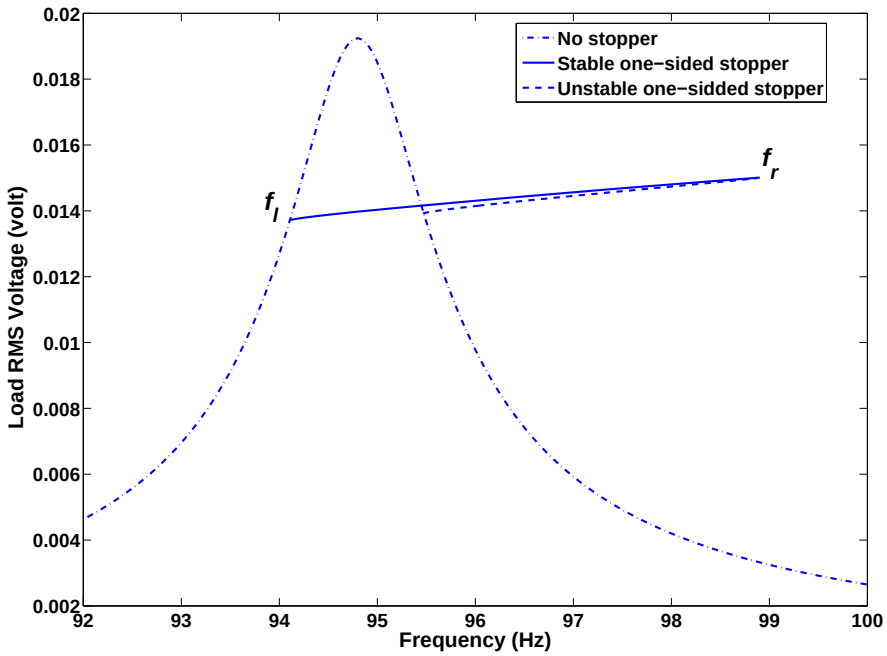

Figure 5.3: Analytical frequency-response curves for the load RMS voltage.

The response of the piecewise-linear and the linear system are identical $a_\circ = Z$ as long as the cantilever beam is not engaging the stopper ($a_\circ < 1$). When the beam engages the stopper, the responses diverge from each other. The effective stiffness of the piecewise-linear system for $z \geq z_\circ$ increases in proportion to the

excursion size $(a_\circ - 1)$ and the interval the beam spends engaged with the stopper each cycle $(\pi - 2\phi_s)$. The higher effective stiffness caps the steady-state amplitude a at a lower level and increases the effective natural frequency beyond ω_1, thus causing the resonance to persist over a wider interval of the frequency spectrum. Figure 5.4 shows the interval the beam spends engaged with the stopper per cycle. Outside the contact region $[94.1, 98.89]$ Hz, the engagement interval is zero. As the frequency increases from 94.1 Hz to 98.89 Hz, the contact interval increases, and the level of the effective stiffness also increases. As a result, the frequency-response curve develops a wider and flatter shape as well as a region of multivalued responses to the right of ω_1. Figure 5.3 shows that placing the stopper at the half-power level increases the bandwidth of the MPG by 240% from 1.4 Hz to 4.79 Hz.

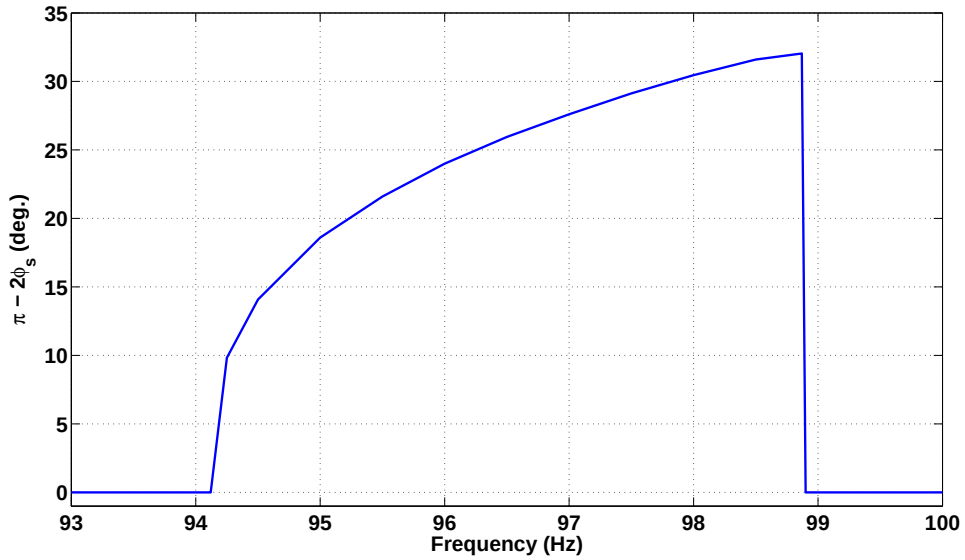

Figure 5.4: The contact interval versus the excitation frequency.

The number of fixed points at each level of the response amplitude $a_\circ$ is always two. To study the stability of those fixed points, the fixed point $(a_\circ, \beta_\circ)$ was substituted in the Jacobian matrix of the right-hand sides of equations 5.14 and 5.15 and the eigenvalues of the resulting matrix were examined [88]. In the ab-

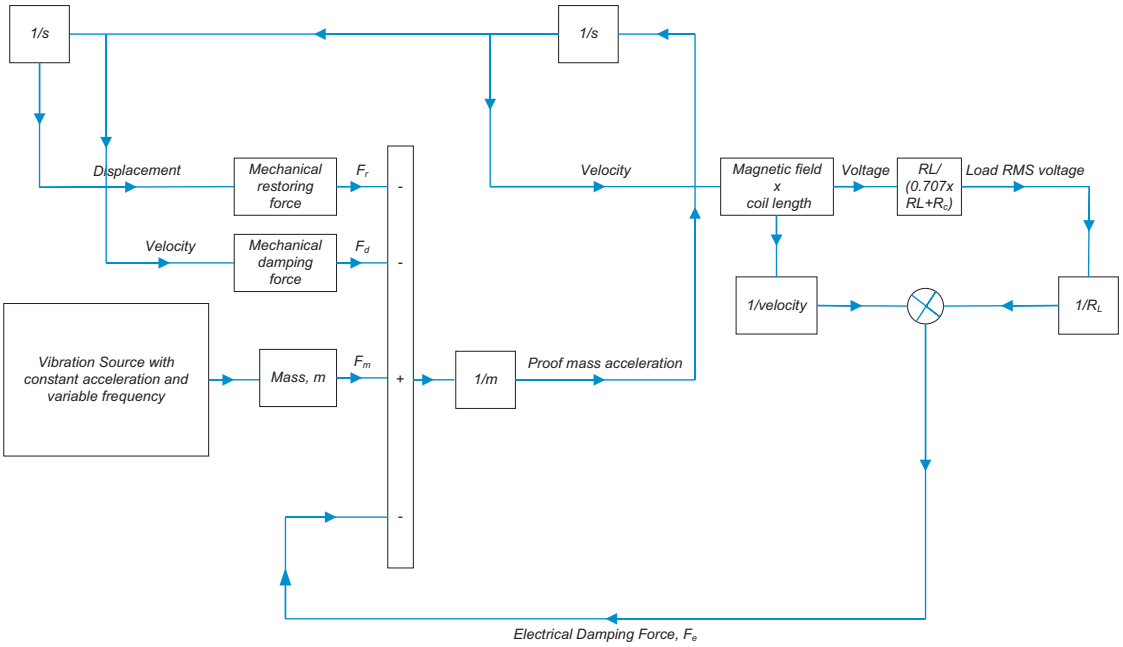

Figure 5.5: SIMULINK block diagram.

sence of stoppers, both fixed points were stable. In the presence of a stopper, the left fixed point was stable, with all its eigenvalues having negative real parts. The right fixed point was unstable, with eigenvalues having a positive real part. At the peak, the two fixed points merged in a saddle-node bifurcation. Therefore, of three solutions co-existing in the frequency interval $[95.5, 98.89]$ Hz, two are stable whereas the third is unstable. This structure of the frequency-response curve leads to hysteresis.

To examine this phenomenon further, MATLAB was used to integrate equation 5.5 numerically and for the same loading conditions of Figure 5.3, which resulted in the frequency-response curve shown in Figure 5.6. The block diagram used for this simulation is shown in figure 5.5 in which both the restoring and mechanical damping forces change according to the conditions of equations 5.1 and 5.2, respectively. The simulation starts at 90.0 Hz, at which point the forcing frequency Ω is increased at a rate of 0.167 Hz/s, and the RMS voltage increases monotonically until point

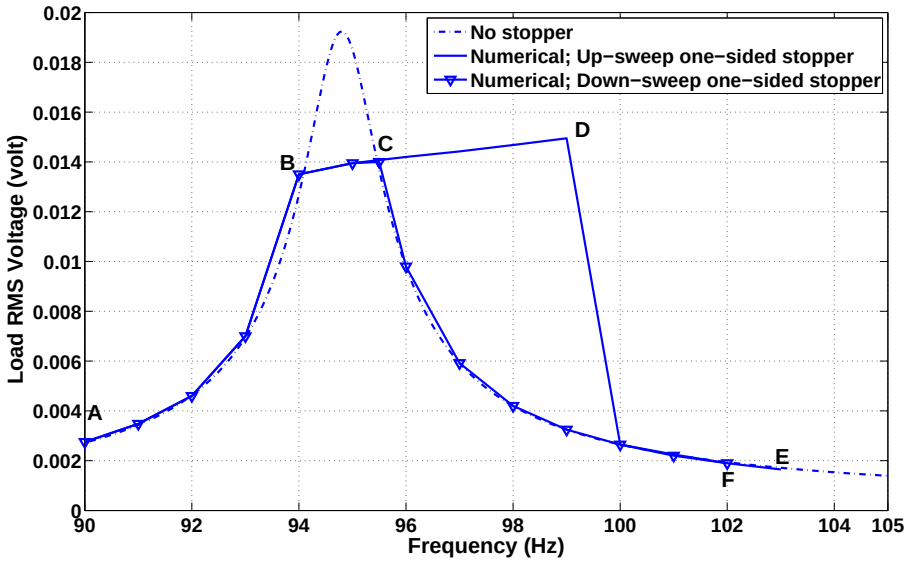

Figure 5.6: Numerical frequency-response curves for the load RMS voltage.

B where the slope of the frequency-response curve drops abruptly as the cantilever beam engages the stopper. For this research, this point was dubbed "the left-end of the up-sweep bandwidth" Ω_l. At point D, the load RMS voltage drops dramatically as the size of the oscillations drops to match that realized by the linear system. Point D was dubbed "the right-end of the up-sweep bandwidth" Ω_r. The responses of the piecewise-linear and the linear systems are identical from this point up to point E. The down-sweep starts at 103 Hz; as the forcing frequency Ω is decreased the voltage increases from point F to point C where the beam starts to engage the stopper, and the slope of the frequency-response curve drops abruptly. An abrupt slope change is seen again at point B, where the response of the piecewise-linear system becomes identical to that of the linear system from this point onward for the rest of the down-sweep. It should be noticed that the up-sweep bandwidth predicted numerically is identical to that predicted analytically. A closed-form expression for Ω_l can be developed by noting that $\Omega = \Omega_l$ when $a_\circ = 1$. Solving the frequency-response equation for $a_\circ = 1$, yields that

$$\Omega_l^2 = 1 - 2\zeta_1^2 - \sqrt{F^2 + 4\zeta_1^2(\zeta_1^2 - 1)} \tag{5.19}$$

Similarly, Ω_r corresponds to the peak of the frequency-response curve (a_{max}, Ω_r). This point is a bifurcation point that satisfies the frequency-response equation and its derivative with respect to $a_\circ$. Therefore, the algebraic system

$$F^2 = c_1 + c_2 a_{max} + c_3 a_{max}^2 \tag{5.20}$$

$$0 = c_2 + 2c_3 a_{max} \tag{5.21}$$

can be solved for the ordered pair (a_{max}, Ω_r), where c_1, c_2, and c_3 are functions of $\Omega_r, \phi_s, \rho, \zeta_1$, and ζ_2.

Theoretically, the cantilever will stay in contact with the stoppers, and half power is produced, as long as the frequency sweeps up or down on curve BCD in Figure 5.6, provided that the excitation frequency starts at any value inside the original BW (94 Hz to 95.4 Hz). If the excitation frequency starts at a value higher than 98.9 Hz, it will follow the normal linear system response until it jumps again in the BW region, when it starts to hit the stopper again and half power is generated. That behaviour is simulated in Figure 5.7. These simulations were verified experimentally using the optimized WMPG, as discussed in section 6.4.

5.2.2 Two-Sided Stopper:

Placing two identical stoppers in a symmetric configuration on either side of the beam merely changes the switching conditions of the equation of motion, equation 5.5, to the following form:

$$\begin{cases} r = 1\,, \quad \zeta = \zeta_1 & |z| < z_\circ \\ r = \rho\,, \quad \zeta = \zeta_2 & |z| \geq z_\circ \end{cases}$$

Following an analysis similar to that used in the previous subsection, the following time-averaged equations are obtained:

$$2\pi \dot{a}\Omega = \int_{-\pi-\phi_s}^{-\pi+\phi_s} \dot{a}\Omega d\phi + \int_{-\pi+\phi_s}^{-\phi_s} \dot{a}\Omega d\phi \int_{-\phi_s}^{\phi_s} \dot{a}\Omega d\phi + \int_{\phi_s}^{\pi-\phi_s} \dot{a}\Omega d\phi \tag{5.22}$$

$$2\pi a\dot{\beta}\Omega = \int_{-\pi-\phi_s}^{-\pi+\phi_s} a\dot{\beta}\Omega d\phi + \int_{-\pi+\phi_s}^{-\phi_s} a\dot{\beta}\Omega d\phi + \int_{-\phi_s}^{\phi_s} a\dot{\beta}\Omega d\phi + \int_{\phi_s}^{\pi-\phi_s} a\dot{\beta}\Omega d\phi \tag{5.23}$$

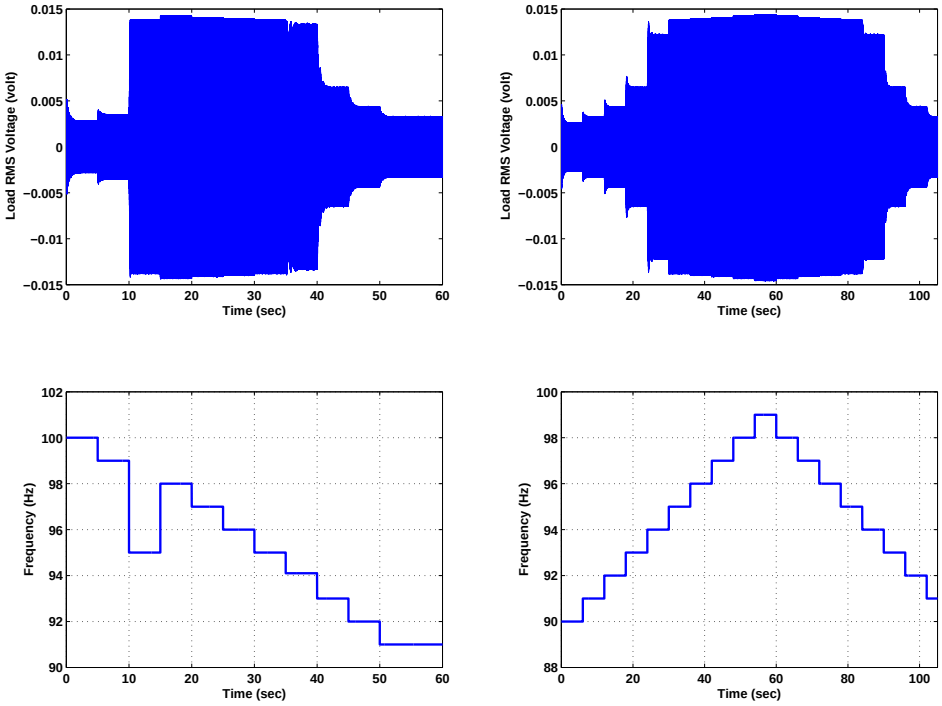

Figure 5.7: Time response for different frequency patterns.

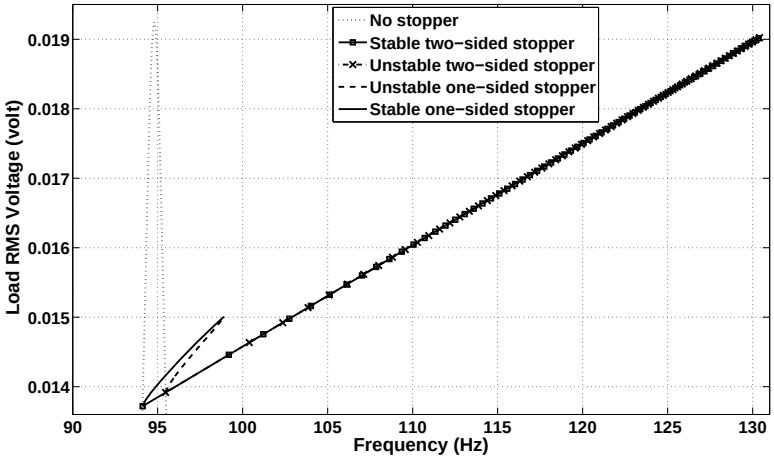

Figure 5.8: Frequency-response curves of the load RMS voltage for the no stopper, one-sided stopper, and two-sided stopper MPGs.

where the period $[-\pi - \phi_s, \pi - \phi_s]$ has been divided into four segments to account for the bilinear switching occurring on both sides of the beam during each period of oscillation. Carrying out the time integration yields the modulation equations

$$\dot{a} \quad = -\tfrac{2}{\pi}(\zeta_1 - \zeta_2)(\cos\phi_s + a\phi_s) - \zeta_2 a + \tfrac{F}{2\Omega}\sin\beta \tag{5.24}$$

$$\dot{\beta} \quad = \tfrac{1}{a\pi\Omega}(1-\rho^2)(a\phi_s - \cos\phi_s) + \tfrac{\rho^2}{2\Omega} - \tfrac{\Omega}{2} + \tfrac{F}{2\Omega}\cos\beta \tag{5.25}$$

Placing two stoppers at equal coil stroke distances ($z_\circ = 0.189\,\text{mm}$) above and below the beam, equations 5.24 and 5.25 were solved for the fixed points to obtain the frequency-response curve for the two-sided stopper system. Figure 5.8 shows a comparison of the frequency-response curves for the load RMS voltage of the one-sided, two-sided, and traditional MPGs. The MPG that used a two-sided stopper has a much larger up-sweep bandwidth than the one-sided stopper or linear MPG.

Using a procedure similar to that implemented in equations 5.19-5.20, the up-sweep bandwidth of the two-stopper MPG was obtained. Figure 5.9 shows a comparison of the variations in the up-sweep bandwidth of the one-sided stopper and the two-sided stopper MPGs to the bandwidth of the no-stopper MPG for coil

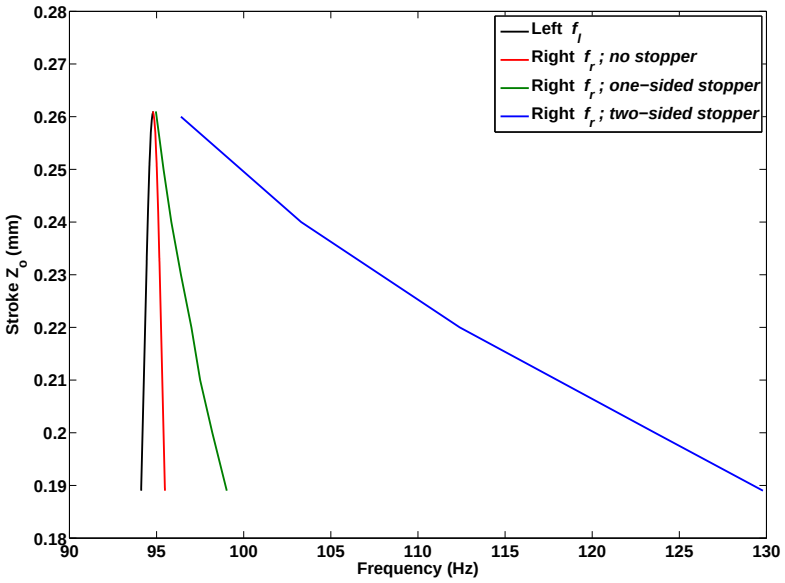

Figure 5.9: The bandwidth of the no stopper, one-sided stopper, and two-sided stopper MPGs.

strockes ranging from the half-power level ($z_\circ = 0.189\,\text{mm}$) to the peak stroke amplitude ($z_\circ = 0.261\,\text{mm}$) of the no stopper MPG. It should be mentioned here that we assumed a fixed contact damping ratio, ζ_2 all through the calculations. At any given stopper height $z_\circ$, the down-sweep bandwidth of the piecewise-linear systems is equal to the bandwidth of the no-stopper system. On the other hand, the up-sweep bandwidth of the piecewise-linear systems shrinks as the stopper height increases. However, as long as $z_\circ \in [0.189, 0.248]$mm for the one-sided stopper or $z_\circ \in [0.189, 0.259]$mm for the two-sided stopper, the up-sweep bandwidth of the piecewise-linear systems is wider than the half-power bandwidth of the no-stopper MPG. When $z_\circ$ is in this interval, the piecewise-linear systems deliver more power P_{elc} for those time stretches when the frequency of the base excitation is different from a value inside the no-stopper MPG bandwidth in any pattern that includes values exceeding the right end of that bandwidth.

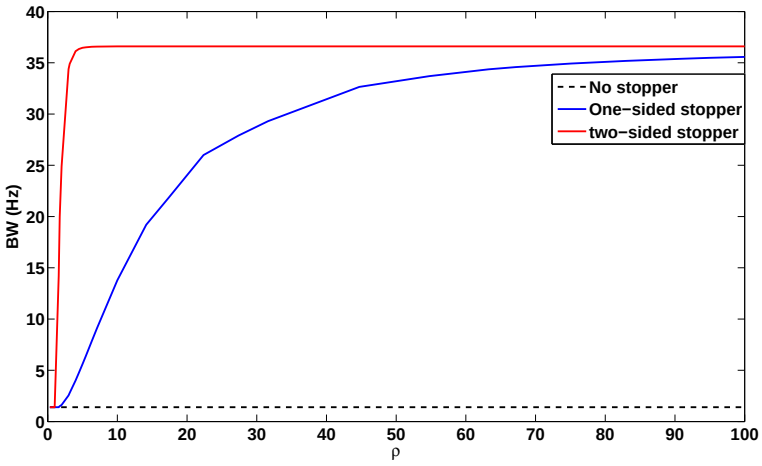

Figure 5.10: Variations in the up-sweep bandwidth $BW = f_r - f_l$ with a stiffness ratio ρ.

Holding the stopper height $z_\circ$ constant at the half-power level and using the damping ratios listed above, equations 5.19-5.20 were solved for a variable stiffness ratio ρ^2, representing the variations in the horizontal position of the stopper $\ell_\circ$, and obtained the variation of the up-sweep bandwidth with the stiffness ratio for the one-sided stopper MPG. Again fixed contact damping ratio was assumed. This procedure was repeated for the two-sided MPG in order to generate a comparison of the up-sweep bandwidths, as shown in Figure 5.10. The results indicate that increasing the stiffness ratio ρ^2 initially increases the up-sweep bandwidth before it saturates at about 35 Hz for both of piecewise-linear systems. The bandwidth of the two-sided stopper MPG saturates much faster than that of the one-sided stopper MPG. On the other hand, decreasing the stiffness ratio to $\rho < 1$, which corresponds to a softening bilinear spring where $k_2 \leq k_1$, was found to have no effect on the bandwidth, which remained constant at 1.4 Hz. It can be concluded that any nonlinear spring with a hardening nonlinearity of $\rho > 1$, including impact oscillators in which $\rho \to \infty$, can be used to increase the up-sweep bandwidth and enhance the performance of the MPG under random base excitations.

5.3 Validation

The test procedure described in section 4.2.1.2 was used to perform up- and down-sweeps of the frequency interval $[90.0, 110]$ Hz at a constant base acceleration of $F = 0.1\,\mathrm{g}$ (RMS). A one-sided stopper was then inserted such that half-power is generated, and the experiment was repeated. The damping ratio during contact between the stopper and the beam ζ_2 was estimated by matching the bandwidth of the analytical and experimental up-sweeps and it was found to be 0.62. Figure 5.11 shows the experimental frequency-response curves for the load RMS voltage compared to the analytical and numerical curves obtained above for a one-sided stopper system.

In the presence of a stopper, all three sets of results have the same structure, with multivalued responses in a region of the frequency-spectrum to the right of ω_1, leading to hysteretic behaviour and a wider up-sweep bandwidth than down-sweep. The down-sweep bandwidth of the one-sided stopper system is equal to that of the no-stopper system in all three cases. The experimentally measured up-sweep bandwidth was 4.79 Hz, an improvement of 240% over that of the no-stopper, or original, system.

Longer contact intervals ($\pi - 2\phi_s$) enhance the bilinear character of the stiffness, that rendering the overall nonlinearity of the system more pronounced. Figure 5.12 shows the power spectra at three points along the up-sweep band. At the left end of the band, where $f = 94.2\,\mathrm{Hz}$, the beam spends $\pi - 2\phi_s = 6.05\,^\circ$ per cycle in contact with the stopper. It spends increasingly longer times per cycle in contact with the stopper at higher frequencies, namely, $\pi - 2\phi_s = 24\ ^\circ$ at $f = 96.0\,\mathrm{Hz}$ and $\pi - 2\phi_s = 31.9\ ^\circ$ at $f = 98.8\,\mathrm{Hz}$. The longer engagement with the stopper enhances the bilinear character of the oscillator, thus the overall nonlinearity of the system more pronounced. This fact can be seen in the increase in the power level at higher harmonics, $2f$ and $3f$, as the forcing frequency Ω and thus the contact

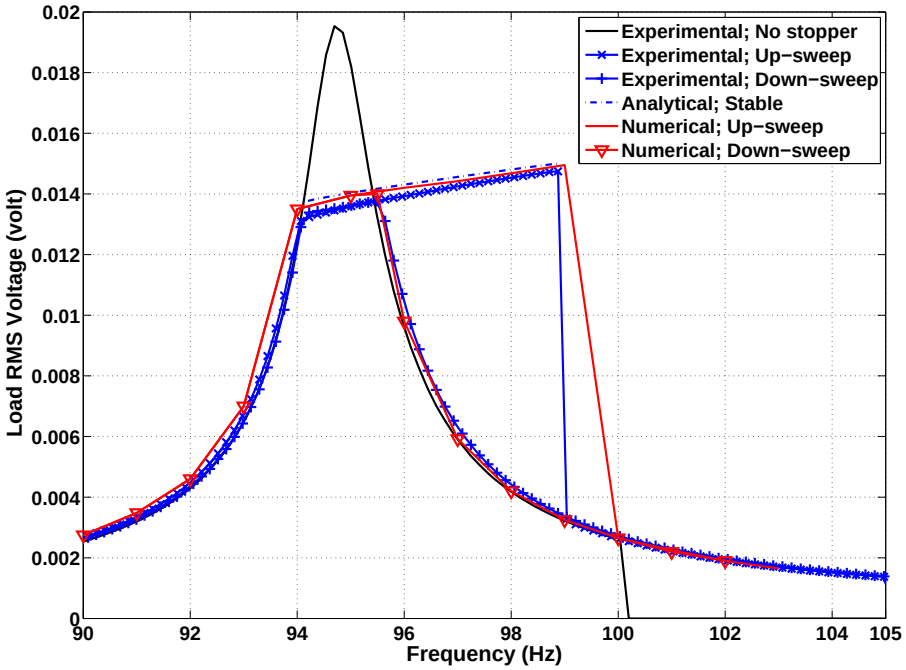

Figure 5.11: Comparison of analytical, numerical, and experimental frequency-response curves for the load RMS voltage.

interval $\pi - 2\phi_s$ increase. The qualitative agreement between the experimental and numerical power spectra indicates that the new model correctly captures the nonlinearity in the system.

To validate the model, we used the modulation equations and the value of ζ_2 estimated above in order to predict the response of the one-sided stopper system at two additional base excitation levels: $F = 0.25\,\mathrm{g}$ and $F = 0.5\,\mathrm{g}$ (RMS). The corresponding frequency-response curves for the one-sided stopper MPG were measured experimentally. The stiffness ratio was held constant at $\rho^2 = 20$ by fixing $\ell_\circ$ for all three cases. The stopper height $z_\circ$ was adjusted to keep the bilinear switching point at the half-power level $z_\circ = \frac{Z_{max}}{\sqrt{2}}$ for all three loading cases. The analytical and experimental results for all three cases are shown in Figure 5.13. The model accurately predicts the up-sweep bandwidth to within 0.5 Hz of the measured value. It overestimates the bandwidth because at higher excitation levels, the impact oc-

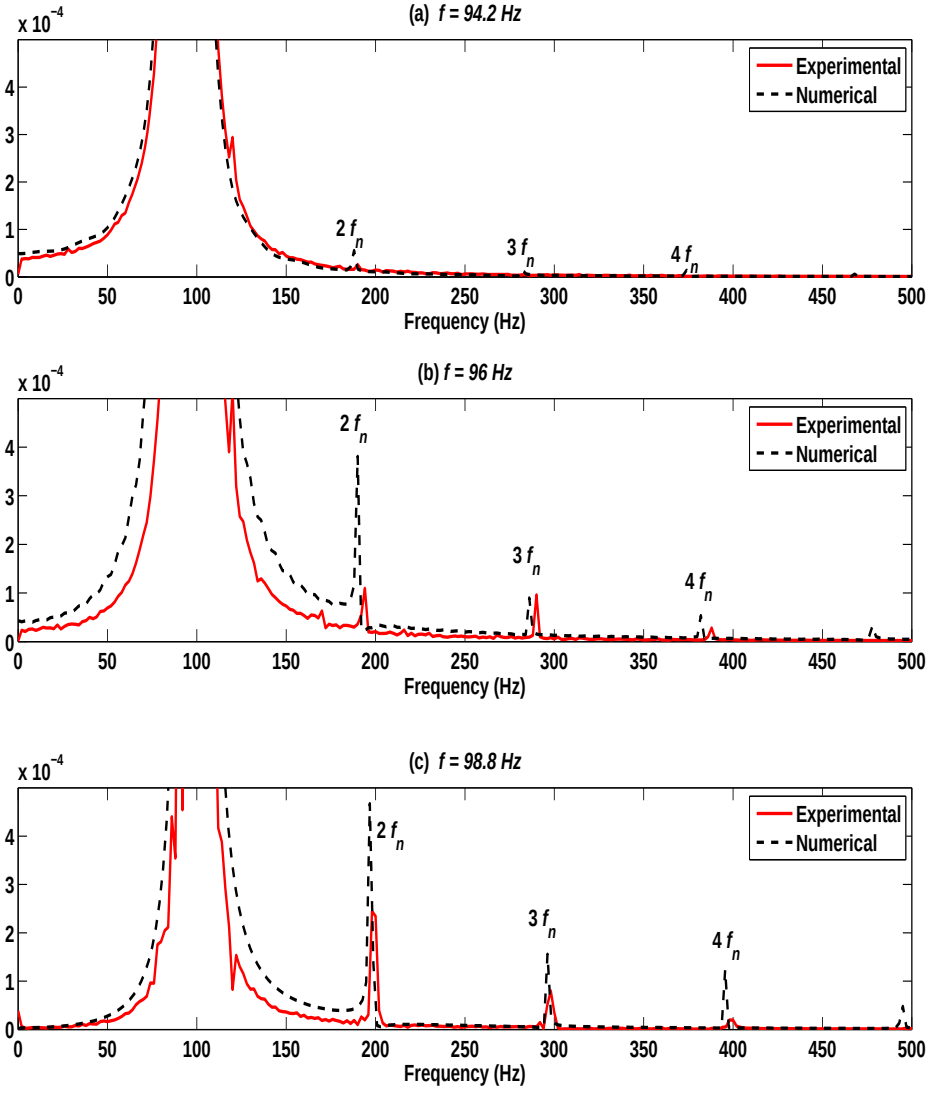

Figure 5.12: Power spectra for three different points in the up-sweep region.

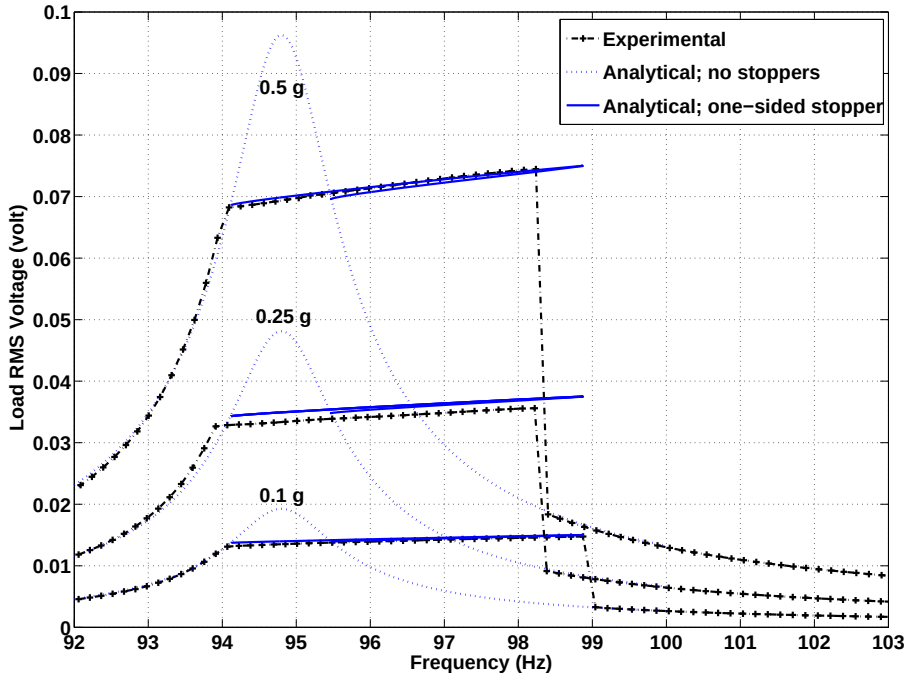

Figure 5.13: Comparison of the analytical and experimental frequency-response curves for $F = 0.1, 0.25$, and 0.5g (RMS).

curs at higher velocities as a result of the higher input force, thus causing more energy losses and a larger ζ_2. Therefore, the constant damping ratio $\zeta_2 = 0.62$ underestimates the damping for the $F = 0.25\,\mathrm{g}$ and $F = 0.5\,\mathrm{g}$ (RMS) cases.

Reducing energy dissipation during impact and contact with one or more stoppers therefore increases the bandwidth and enhances the performance of the wideband MPG.

The performance of the WMPGs was examined under random base excitations by simulating the responses of the no-stopper and one-sided stopper MPGs in SIMULINK under base excitations with a Gaussian-distributed frequency over a 13.8 Hz range centred around the natural frequency of the MPG, i.e. standard deviation (σ) of 2.3 Hz. The stopper height of the one-sided stopper MPG was set to the half-power height of the no-stopper MPG. The energy was collected only when the power was higher than the half-power level. The simulations were run six

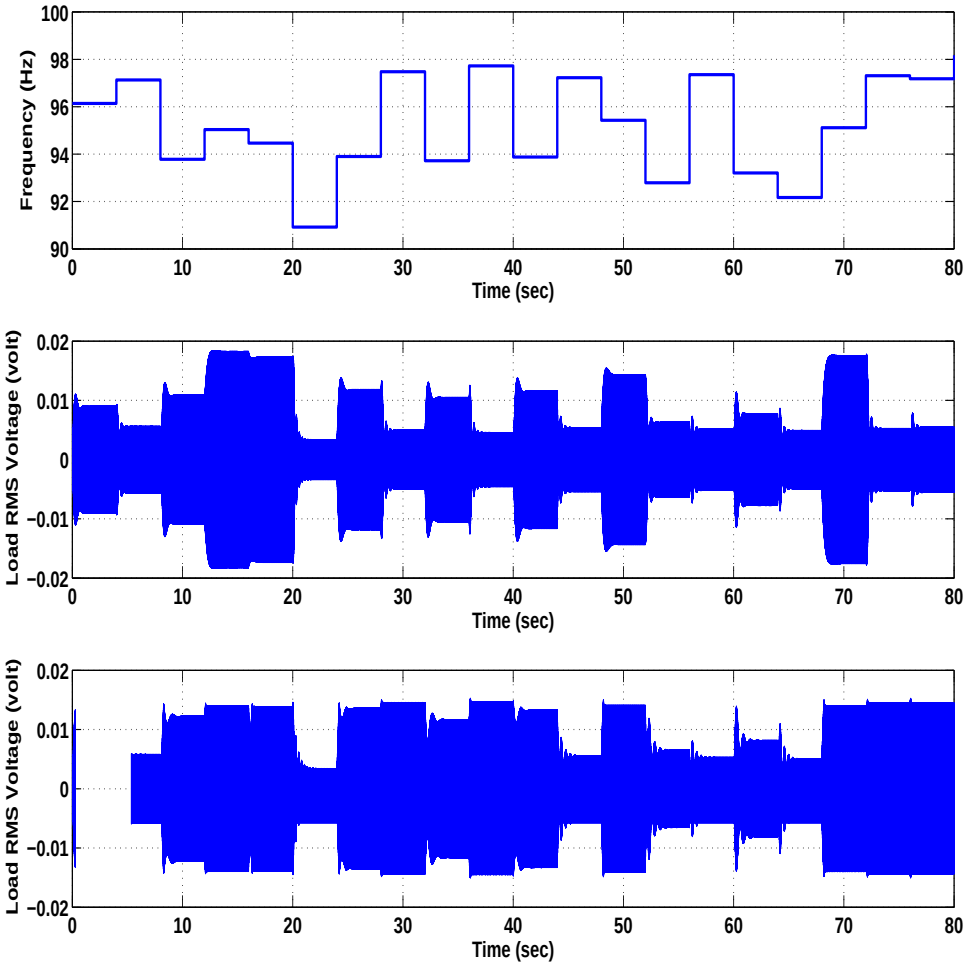

Figure 5.14: The time-history of the base excitation frequency (a) and the load RMS voltage of the no-stopper (b) and the one-sided stopper (c) MPGs, all obtained by numerical simulation.

times each using a different random seed and lasting for 80 seconds. It was found that the one-sided stopper MPG collected 30% more energy than the no-stopper MPG. Figure 5.14 shows the frequency of the base excitations and the reponses of both MPGs during one of these numerical experiments.

Although the one-stopper MPG collects energy at a lower power level, it does so for a larger time fraction, thus resulting in a greater amount of collected energy overall.

The possibility of grazing bifurcation and the appearance of chaos at both ends of the up-sweep bandwidth $[\Omega_l, \Omega_r]$ where the beam arrives at the stopper with approximately zero velocity ($\dot{z} \approx 0$) was investigated. Figure 5.15 shows the time-history of the load RMS voltage as the base excitation frequency Ω increases slowly past the left end Ω_l and right end Ω_r of the up-sweep bandwidth. It was found that the response in both cases was regular and periodic indicating the absence of chaos. These results suggest that the presence of electric damping in addition to mechanical damping results in an overall level of damping in the system significant enough to preclude the possibility of chaos.

5.4 MEMS-Based EMPGs

Although the technique that was proposed and validated applies to all macro-sized EMPGs, however, the efficiency of this kind of WMPGs is reduced by the following restrictions:

- The electrical energy extracted from the vibrations is proportional to B^2. For macro-sized MPGs, the air gap is large, which results in a reduction in the field density and the amount of energy extracted. Also small air gap allows for more uniform magnetic field distribution over the shuttle stroke.
- Large structures suffer from high mechanical damping, which represents pure energy loss, leading to lower energy conversion efficiency.
- Large areas of contact during the impact between the stopper and the cantilever leads to higher loss, especially when the impact occurs at high velocity and the cantilever slides over the stopper; i.e., ζ_2 is very high, which shrinks the up-sweep bandwidth.

All the above problems can be overcome through the use of MEMS fabrication technology. If the moving shuttle is fabricated by this technology, small air gaps can

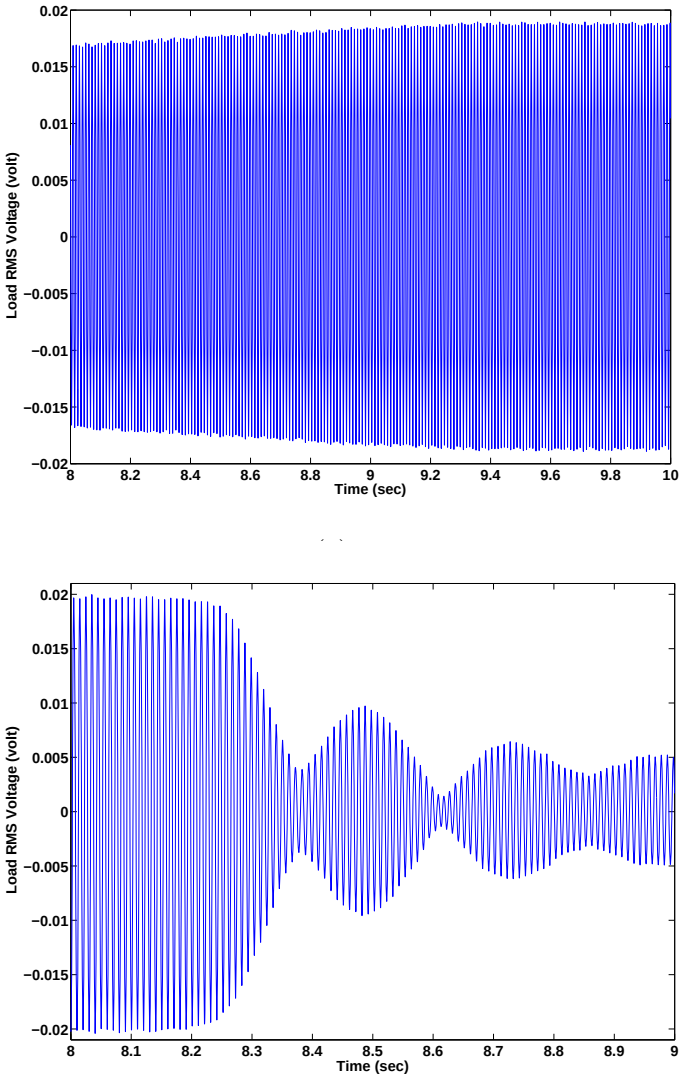

(b)

Figure 5.15: The time-history of the load RMS voltage as the forcing frequency Ω increases past (a) Ω_l and (b) Ω_r.

be obtained, which will provide high magnetic field density in the gap so that the generator can pick up energy more efficiently from even low g vibrations. MEMS structures do not suffer from high mechanical damping and thus have a low b_m. The contact loss, because of ζ_2, is expected to be small because the engaged areas are small and the system can be designed so that no sliding occurs between the engaged areas during the impact. Also, it is easy to microfabricate structures with different number of stoppers with different shapes on the same mask process. This section introduces a road map for designing wideband MEMS-based EMPGs that utilize piecewise-linear oscillators with an inexpensive process. The fabrication of the moving shuttle, coil and external housing are discussed. The mathematical model developed in order to predict the structure's behaviour is also presented.

5.4.1 The MEMS Prototype

Figure 5.16 shows the construction of the proposed MEMS-based EMPG. It consists of a stator and translator (rotor). The stator houses the magnetic parts of the generator and the translator contains both the mechanical suspension and the electrical coil systems. The translator consists of a shuttle supported by a set of beams. When the shuttle and the attached coil move relative to the stationary magnetic field, electrical voltage induced in the moving coils. Folded beam springs were utilized in this work, with the outer beams rather than the inner beams anchored to the housing of the MPG, which allows to remove the substrate underneath the shuttle in order to integrate another coil and/or proof mass on the bottom surface of the shuttle, thus increases the voltage generated.

Four permanet magnets, 5 mm × 5 mm × 2 mm each, were attached to a steel yoke in order to maintain the magnetic field in the 4 mm air gap. A lexan housing was built to hold the whole system, i.e., the magnets and the steel yoke, as shown in Figure 5.17. FEA simulations estimated the field density in the air gap as 0.3 T as shown in Figure 5.18.

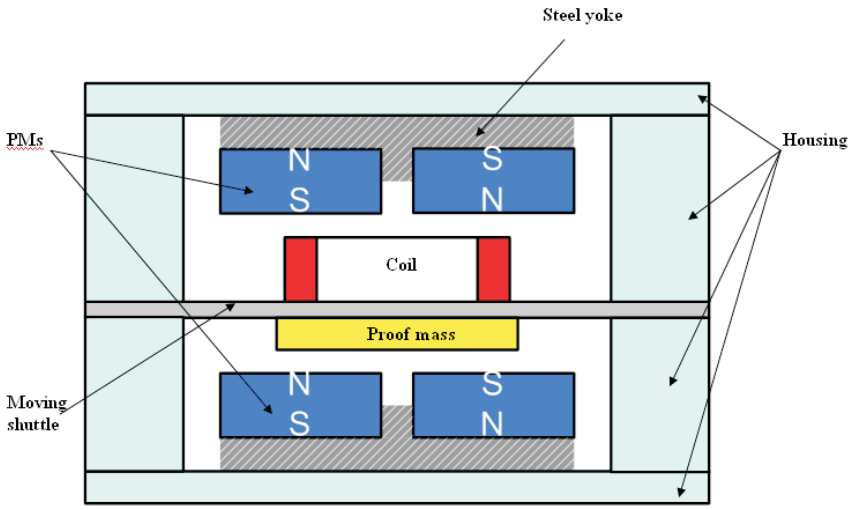

Figure 5.16: Cross section of the MEMS MPG.

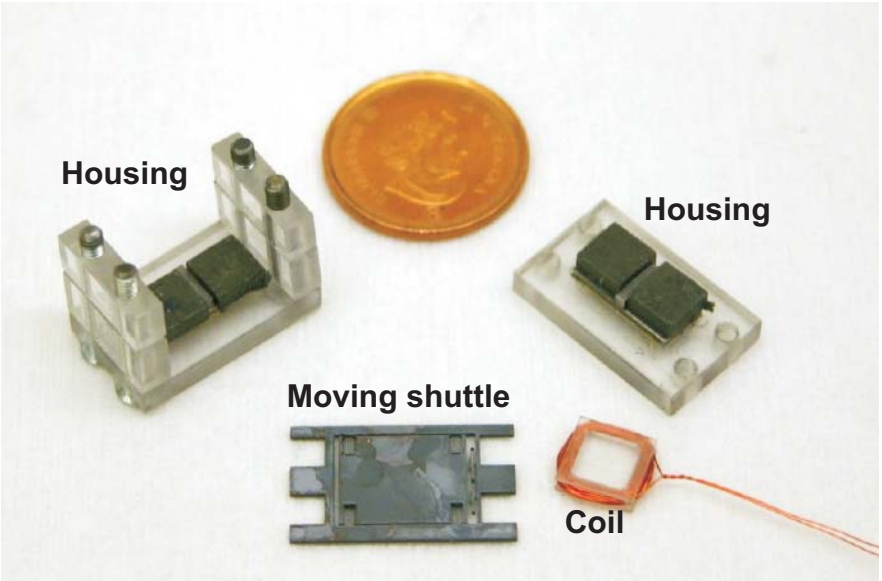

Figure 5.17: Photograph of the MEMS-based MPG.

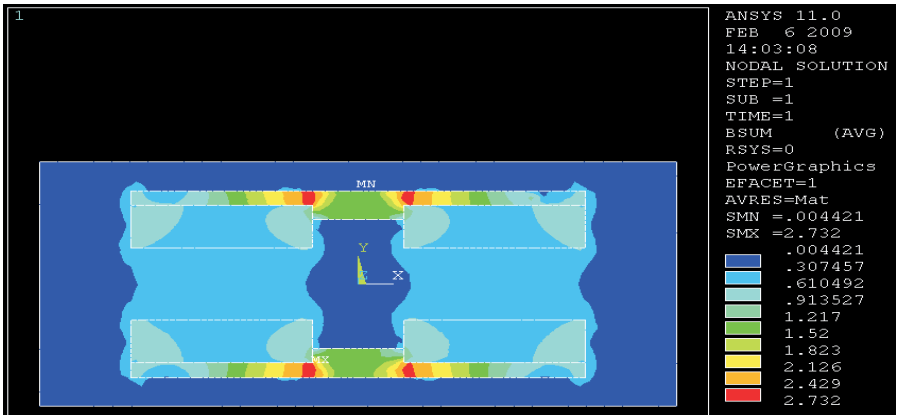

Figure 5.18: Magnetic field calculation for the MEMS MPG.

The shuttle was designed so that the impact occurs with almost no sliding of the moving shuttle over the stopper in order to reduce frictional losses. Figure 5.19 shows a layout of the moving shuttle with four folded-beam springs with a stiffness of k_1, is called main spring, and on the right of the shuttle at a pre-calculated distance; i.e., $z_\circ$ from it, in this case at the half-power position, are the two auxiliary springs that are used to change the total stiffness from k_1 to $k_1 + k_2$. The width of the beams of the auxiliary springs determines the value of the stiffness ratio; i.e., ρ^2.

Two main issues must be taken into consideration when the shuttle is fabricated. First, the aspect ratio of the beams, i.e., the width and the depth of a beam, must be as high as possible in order to avoid out-of-plane motion when it is vibrated in the in-plane direction. Second, the shuttle can not be fabricated using metallic material, which means that electroplating cannot be used to fabricate the shuttle because most of the power generated would be lost in the material of the shuttle as eddy current losses. Therefore, a one-mask DRIE fabrication process with an aspect ratio close to 1:17 was employed. The fabrication process is shown in Figure 5.20, and Figure 5.21 provides a close-up view of the fabricated shuttle. Figure 5.22 shows a close-up picture of both the main and auxiliary springs.

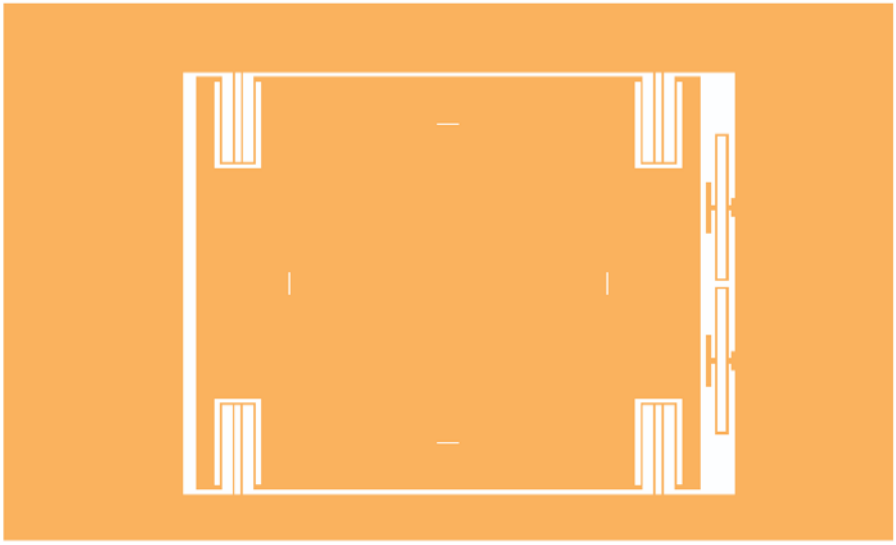

Figure 5.19: MEMS shuttle layout.

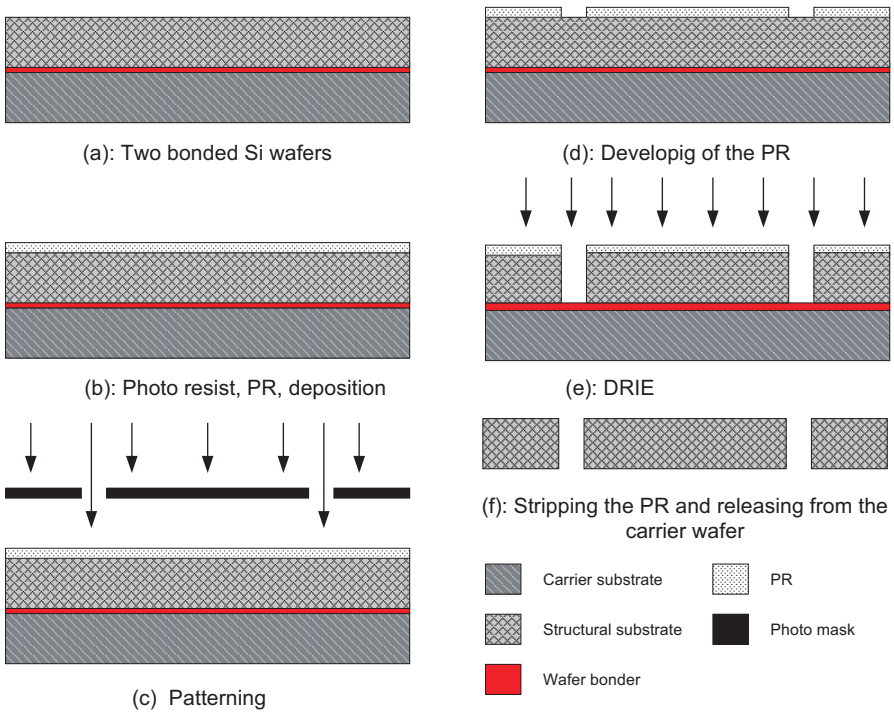

Figure 5.20: MEMS shuttle fabrication process.

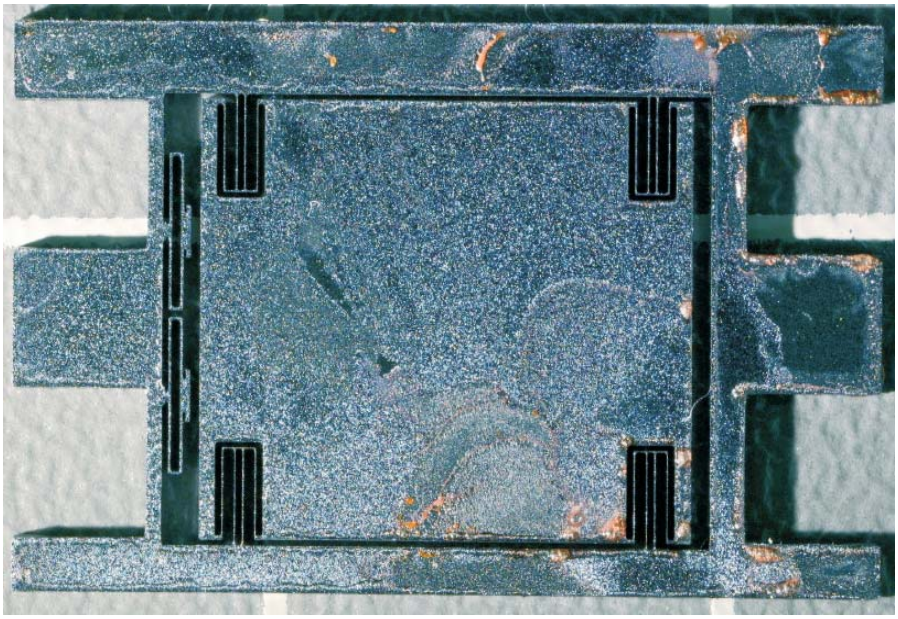

Figure 5.21: Photograph of the MEMS shuttle.

The coil attached to the moving shuttle can be either fabricated using the electroplating technique or manufactured from regular wire. Lexan was used as a core around which the coil was wound (Figure 5.17).

5.4.2 Case Study

The MEMs shuttle was designed with four main folded-beam springs. The main spring beam is 2 mm long and 30 μm wide, and the total structural substrate is 525 μm thick. The auxiliary spring beam is 1.5 mm long and 65 μm wide, with the same thickness as the substrate. ANSYS was used to calculate the stiffness of both the main and auxiliary springs: 925 N/m and 8325 N/m, respectively; i.e., $k_2 = 9k_1$. Figure 5.23 shows the deflection of the MEMS structure under a static load of 0.185 mN. The coil was manufactured by winding 25 turns of 34 AWG wire around a lexan core with an average coil side length of 6 mm, which results in an estimated total mass of 0.425 grams and total effective coil length of 30 cm. The calculations ignored b_m with respect to b_e, which results in ζ_1 having a value

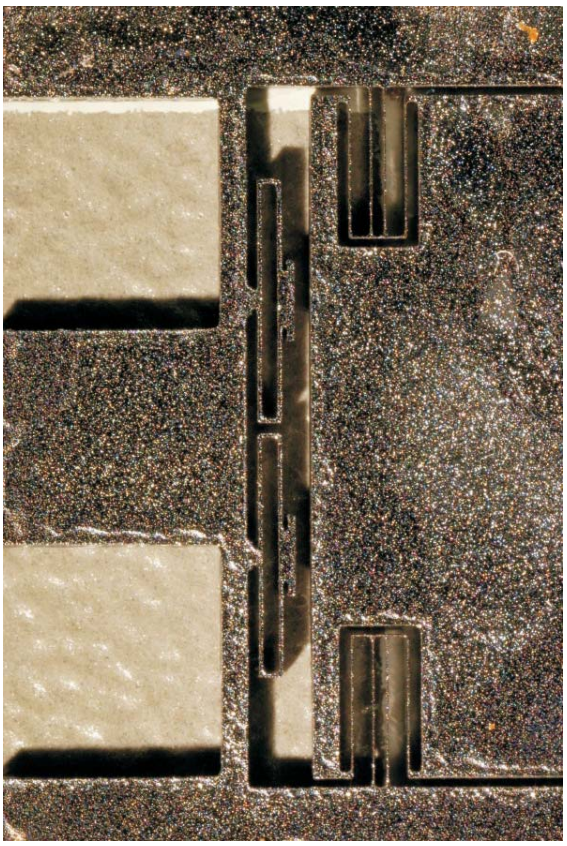

Figure 5.22: Close-up of the main and auxiliary beams with aspect ratios of 1:17.5 and 1:8, respectively.

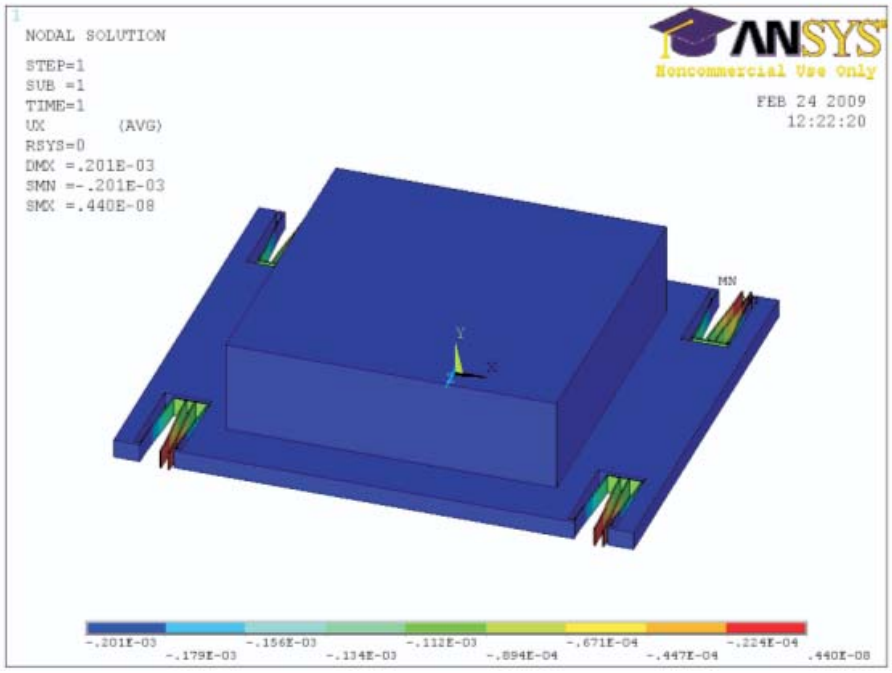

Figure 5.23: FEA of the suspension system.

of 0.003. The estimated power, load RMS voltage, and maximum stroke of the shuttle are shown in Figures 5.24, 5.25 and 5.26, respectively, based on an internal coil resistance of 1.5Ω and a resistive load of same value with an input vibration of 0.2 g (RMS). The half-power bandwidth is estimated to be 1.6 Hz.

5.4.3 Analytical Model

The equation of motion for the new MEMS structure shown in Figure 5.19 can be written as

$$m\ddot{z} + b\dot{z} + kz = -m\ddot{y} + k_2 z_\circ h(z - z_\circ) \tag{5.26}$$

where $h(z - z_\circ)$ is the Heaviside function, $k = k_1$ or $k_1 + k_2$, and $b = b_1$ or b_2 according to $z < z_o$ or $z \geq z_o$, respectively. The nondimentionalized equation of motion can be written as

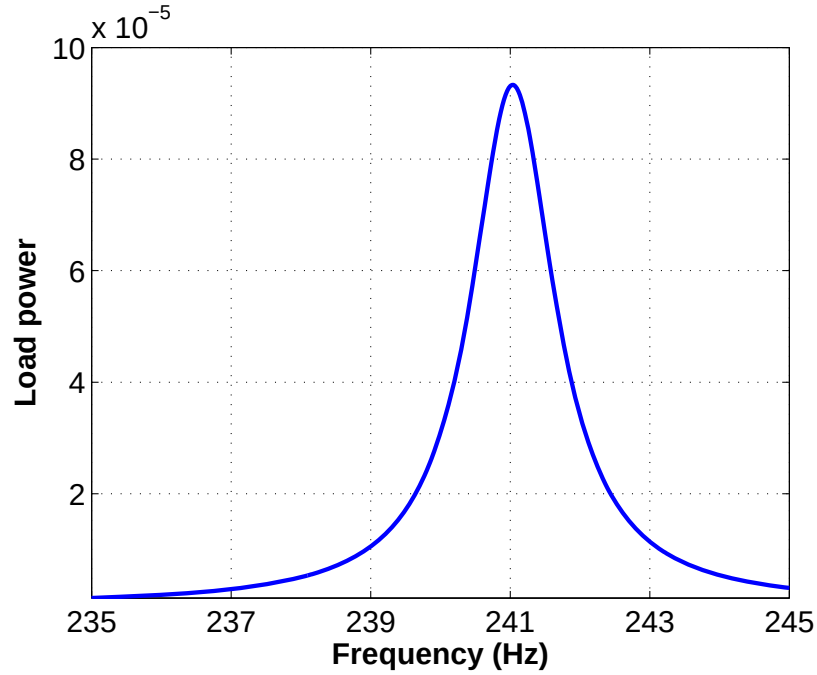

Figure 5.24: Load power versus input frequency.

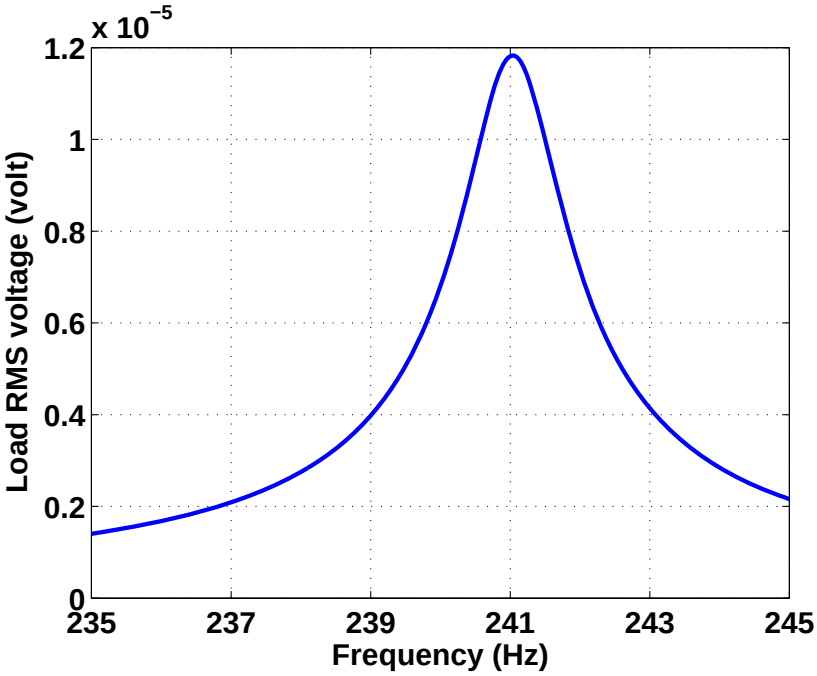

Figure 5.25: Load RMS voltage versus input frequency.

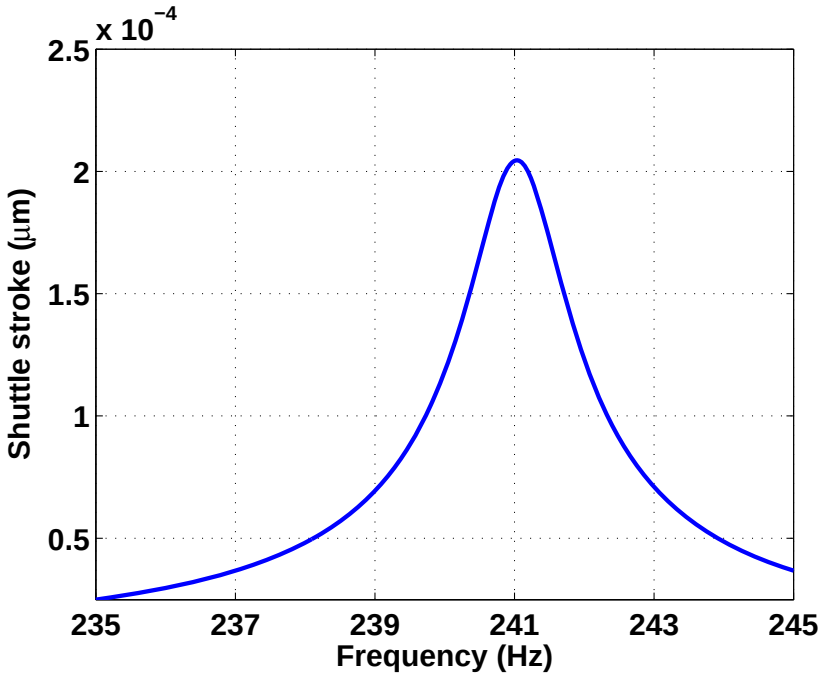

Figure 5.26: Shuttle stroke versus input frequency.

$$\ddot{z} + 2\zeta\dot{z} + r^2 z = -\ddot{y} + {r_s}^2 h(z-1) \tag{5.27}$$

where $r_s = \frac{\omega_s}{\omega_1}$ and $\omega_s = \sqrt{\frac{k_2}{m}}$.

Following the procedure presented in Section 5.2.1, the fixed point can be found by solving the following two equations:

$$F\sin\beta_\circ \quad = \tfrac{2\Omega}{\pi}(\zeta_1 - \zeta_2)(\cos\phi_s + a\phi_s) + \Omega(\zeta_1 + \zeta_2)a \tag{5.28}$$

$$F\cos\beta_\circ \quad = -\tfrac{1}{2}a_\circ\left[(2 - {r_s}^2) + \tfrac{2}{\pi}{r_s}^2\phi_s - 2\Omega^2\right] - \tfrac{{r_s}^2}{\pi}\cos\phi_s \tag{5.29}$$

As per the discussion in Section 5.3, it was found that the contact damping ratio, ζ_2, is much higher than the regular design damping ratio, ζ_1; typically, $\zeta_2 = 138\zeta_1$. This high contact damping ratio dramatically reduces the up-sweep bandwidth. As expected of the MEMS-based MPG, the contact damping ratio should be significantly reduced. The value of ζ_2 was varied from ζ_1 to $10\zeta_1$ and the up-sweep bandwidth was calculated by solving equations 5.28 and 5.29 for each ζ_2 in order

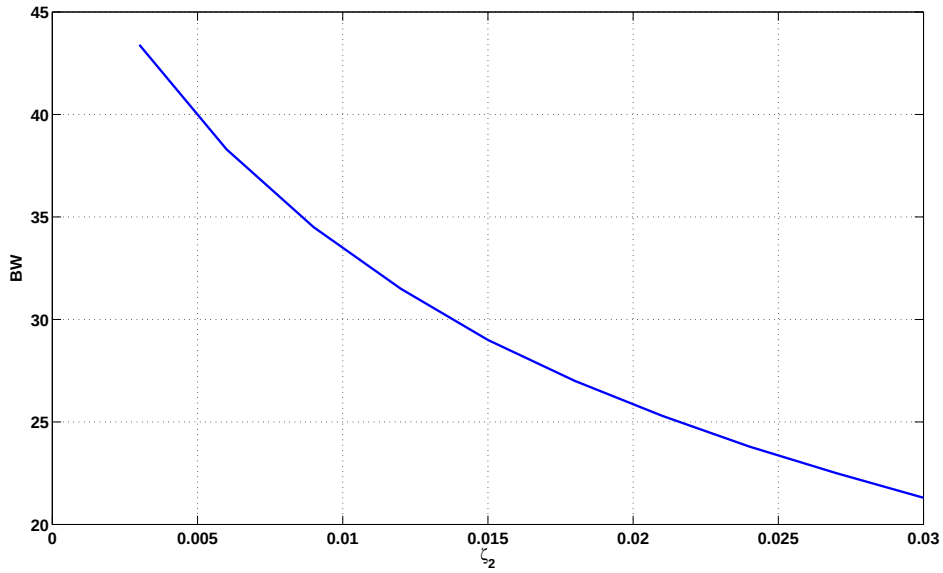

Figure 5.27: Up-sweep bandwidth versus ζ_2.

to show how the response improves when ζ_2 is reduced, the results are shown in Figure 5.27.

5.5 Summary

This chapter has presented a novel architecture for wideband vibration-based MPGs and has explained the process whereby it was validated. In this architecture, the standard linear oscillator is replaced with a piecewise-linear oscillator in order to harvest environmental vibrations. Analytical, numerical, and experimental techniques were used to analyze a prototype of an electromagnetic MPG designed and constructed according to the proposed architecture.

Compared to the results achieved with a traditional MPG, it was found that the new architecture increases the bandwidth of the MPG during an up-sweep, while maintaining the same bandwidth during a down-sweep. Experimental measurements showed that, at half-power level, the up-sweep bandwidth is 240% wider

than that achieved with the traditional architecture. Closed-form expressions for the response of the piecewise-linear MPG as well as for the size of the up-sweep bandwidth were developed and validated experimentally. Further research is needed to increase the up-sweep bandwidth by decreasing energy losses due to impact and contact between the beam and the stopper and to optimize the stroke height $z_\circ$ for maximum power generation.

A MEMS-based MPG along with its coil and magnetic housing was designed, simulated, and fabricated. The shuttle was built using one-mask DRIE process. The analytical model was modified to represent the modified MEMS structure. Based on the analytical model, the half-power up-sweep bandwidth can increase up to 40 Hz with a design has low contact damping ratio, i.e., ζ_2. A more reliable and robust fabrication process is required utilizing other different materials (soft materials to allow for low natural frequency) for the moving part of the MEMS structure.

Chapter 6

Optimization of Piecewise-Linear MPGs

In the previous chapter, it was shown that as $z_\circ$ increases and the bandwidth shrinks, the fraction of time when the MPG collects energy decreases, while the load voltage V_L, and thus P_{elc}, increases. Therefore, an optimization process is required in order to determine the stopper position that will deliver maximum power for a given MPG architecture and probability distribution of the base excitation frequency Ω. This chapter presents design and optimization procedures for enhancing the performance of wideband micro-power generators (WMPGs). Such process requires additional steps beyond those needed in the design of regular, or nominal, MPGs. The extra steps are required in order to match the output power and bandwidth of the WMPG to the Probability Density Function, i.e., PDF, of the environmental vibrations. While these requirements add complexity to the design of WMPGs, they have been shown to significantly increase energy harvested by the MPG. The design objective is to maximize the potential of the wideband MPG to collect energy in an environment that has a known vibration probability density function (PDF). Without loss of generality, a Gaussian PDF $G(f; f_\circ, \sigma)$ with a mean frequency $f_\circ$ and a standard deviation σ is assumed. Further, the size of

the optimal MPG can be considered so that it does not exceed the footprint of the nominal MPG.

6.1 Nominal MPGs

The same prototype shown in Figure 5.1 was used, but here it is called the nominal MPG. However, the stopper, which is a screw in this case, was replaced with different stopper. This modification affected the frequency response of the nominal MPG under wideband operation because the new stopper seems to reduce the losses during the impact with the cantilever, resulting in a wider bandwidth, frequency response is shown later in Figure 6.5. In addition, when the proof-mass was reattached to the cantilever, it seems that the resonant frequency of the system shifted from 94.8 Hz to 94.2 Hz as the centre of the mass shifted a bit from its position in the original structure. All other elements remained as presented in Section 5.1.

The stopper is located at a distance $l_\circ = 28.8$ mm from the root of the cantilever beam, corresponding to a stiffness ratio of $\rho^2 = 20$, and at a height $h_\circ = 81\mu$m above the beam, corresponding to the half-power level of the regular (no-stopper) MPG. The damping ratio during contact between the beam and the stopper was estimated as $\zeta_2 = 0.57$ by matching the up-sweep bandwidth obtained from the model with that measured experimentally.

6.2 Optimization of the Mass and Damping Ratio

Since the MPG is designed for a given vibration PDF, the natural frequency of the MPG f_r must maintain its position in the frequency spectrum with respect to $f_\circ$. To maximize the inertial mass without changing f_r, the ratio between the effective mass m and stiffness k_1 is maintained as the mass increases. Equation 3.2

shows that increasing m and k_1 by a factor s while holding the mechanical damping constant b_m decreases the damping ratio of the unengaged MPG ζ_1 by the same factor. In practice, increasing the size of the mechanical oscillator also increases b_m. Therefore, the process of optimizing the mass and damping ratio is reduced to a one-parameter search for the minimum value of ζ_1.

In a regular MPG, decreasing ζ_1 by a factor of s increases the maximum displacement Z_{max}, and therefore the maximum output power, as shown in Figure 6.1.

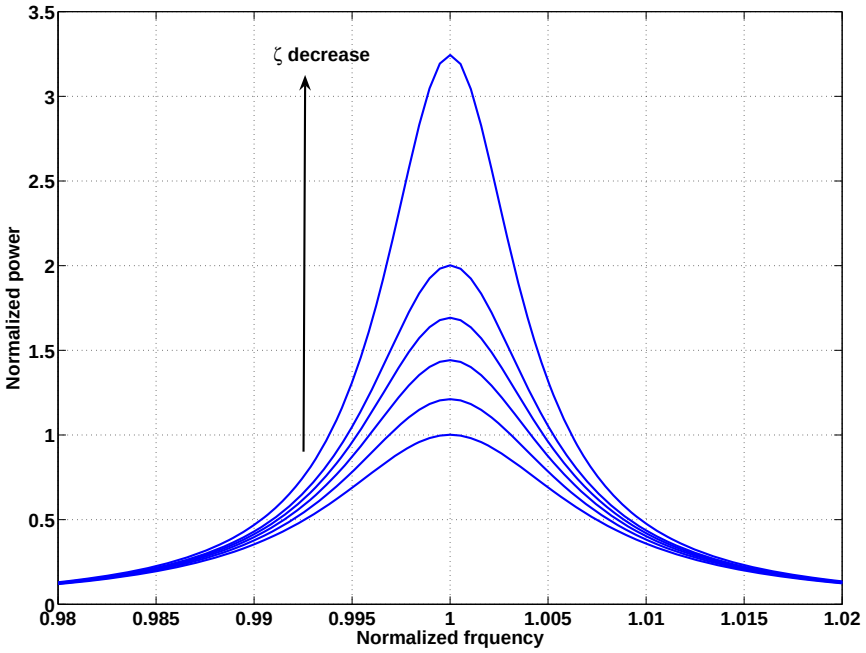

Figure 6.1: Effect of the variation of ζ_1 on the performance of the nominal MPG.

This process induces higher stresses in the suspension beams and requires a larger footprint, thereby violating the optimal design objectives. The wideband MPG avoids these drawbacks by restricting the stroke size ($z_\circ \approx Z_{max}$). Figure 6.2 shows the frequency-response curves of the wideband MPG output power when ζ_1 is reduced by factors of $s = \frac{1}{\sqrt{2}}$ and $s = \frac{1}{2}$ (m and k_1 increased by s), while the

stopper height is held constant at a height corresponding to the half-power level of the regular MPG. The wideband MPG reduces the MPG footprint at the maximum stroke ($s = \frac{1}{2}$) to an area smaller than that of a regular MPG at the minimum stroke ($s = 1$). Although the wideband MPG decreases the maximum realizable output power, it also increases the MPG bandwidth and thus the energy-collection time. The optimization of this trade-off between the level of the output power and the size of the bandwidth in order to maximize the energy collected is addressed in Section 6.3. As discussed earlier, the damping ratio of the MPG increases from ζ_1 to ζ_2 during contact between the cantilever and the stopper due to impact and friction losses. The optimization of the contact damping ratio is considered further in section 6.3.

Figure 6.3 shows the coil-mass-cantilever beam assembly of the nominal MPG and of a modified MPG, dubbed prototype B. The linear stiffness, k_2 of prototype B was calculated as $k_2 = 2539.4\,\mathrm{N/m}$ using 3D static analysis in ANSYS. The resonant frequency, f_r of prototype B was measured at 94.52 Hz. When f_r was substituted in equation (4.11), effective mass, m, was found to be 7.2 grams.

In order to measure the frequency response of the two MPGs, they were connected to a resistive load $R_L = 2.7\,\Omega$ and the frequency of the base acceleration was swept in the interval $[90.0, 110]\,\mathrm{Hz}$, while holding the amplitude of the acceleration constant at $F = 0.1\,\mathrm{g}$ (RMS). Figure 6.4 shows the frequency-response curves for the voltage across R_L for both MPGs operating in regular mode. The half-power bandwidths BW were measured to be 1.39 Hz for the nominal MPG and 0.858 Hz for prototype B, as shown in Figure 6.4. For a regular MPG, the linear model can be used to write

$$BW = \frac{b_m + b_e}{2\pi m} \tag{6.1}$$

The MPGs share the same electrical damping coefficient $b_e = \frac{(B\ell)^2}{R_L} = 0.0161\,\mathrm{N\,s/m}$; therefore, the mechanical damping coefficients for the nominal MPG and prototype

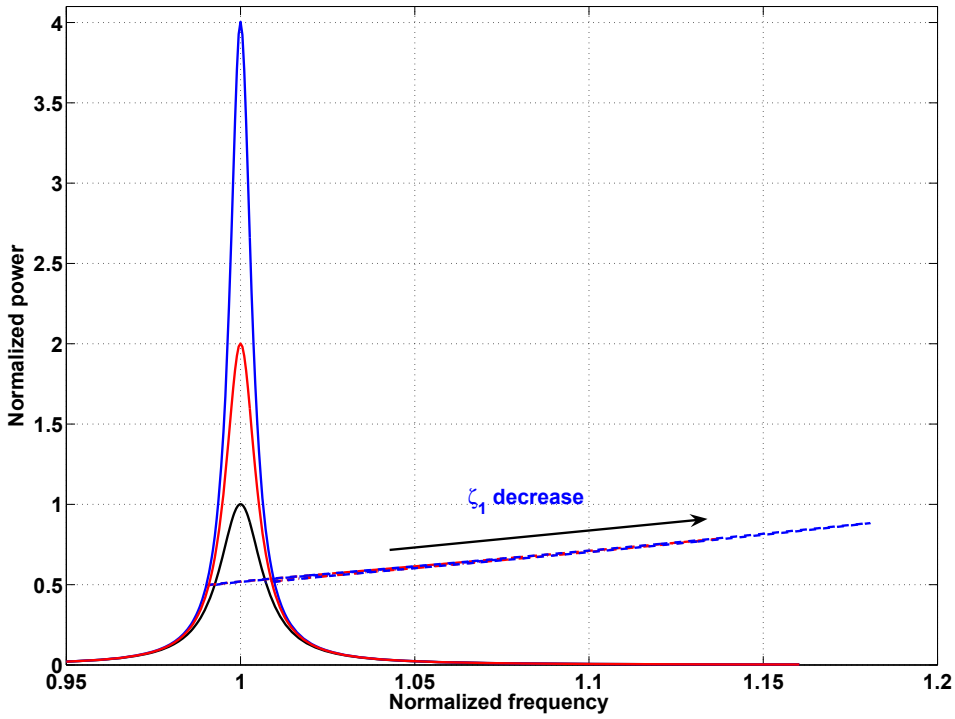

Figure 6.2: Frequency-response curves of the nominal MPG output power in regular mode (solid) and wideband mode with the stopper height set to the half-power level (dashed) and the damping ratio ζ_1 reduced by three factors: $s = 1$ (black), $s = \frac{1}{\sqrt{2}}$ (red), and $s = \frac{1}{2}$ (blue).

B can be calculated as $b_m = 0.0168\,\mathrm{N\,s/m}$ and $0.0225\,\mathrm{N\,s/m}$, respectively. Using equation 6.2, the damping ratio of prototype B was calculated as $\zeta_1 = 0.0045$, that is, 62.5% of the nominal design. Although the effect of size increased mechanical dmaping b_m, the increase in mass and stiffness was more effective in lowering the MPG damping ratio.

$$\zeta = \frac{b_e + b_m}{2\sqrt{km}} \tag{6.2}$$

Figure 6.5 compares the frequency-responses for the load RMS voltage for the nominal MPG in regular mode and the nominal and for prototype B MPGs in

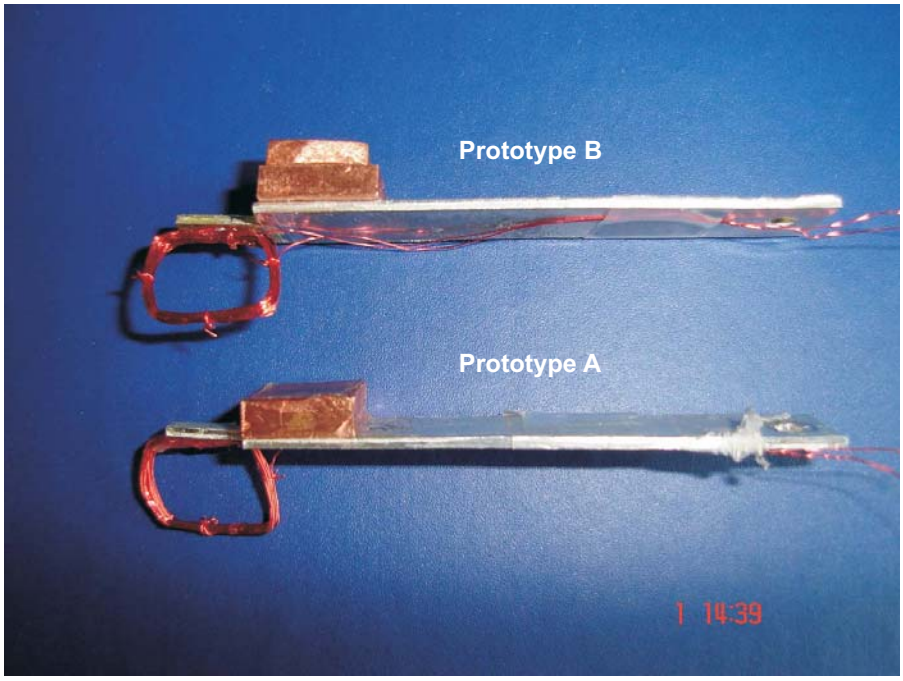

Figure 6.3: The nominal MPG and prototype B.

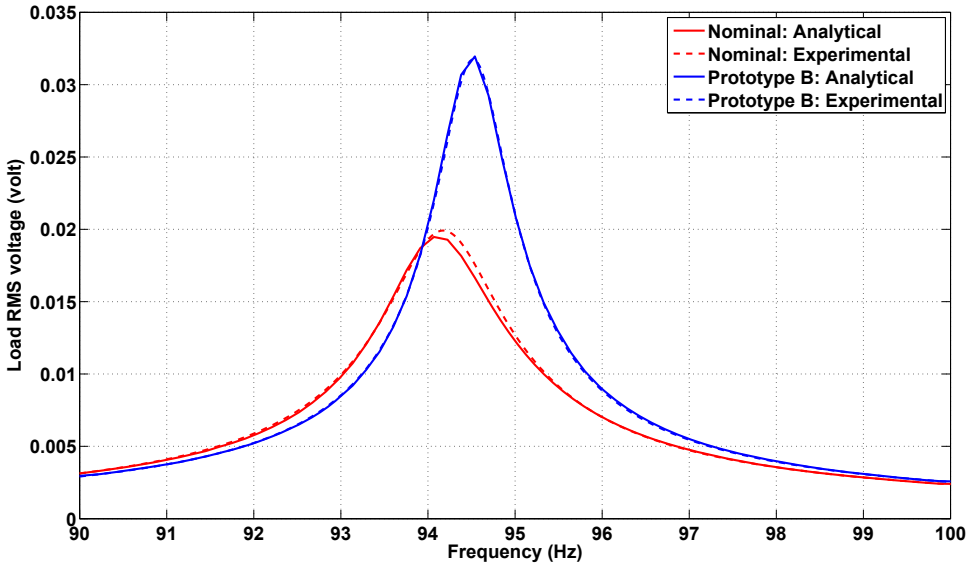

Figure 6.4: Experimental frequency-response curves of the RMS voltage across R_L for the nominal MPG and prototype B operating in regular mode.

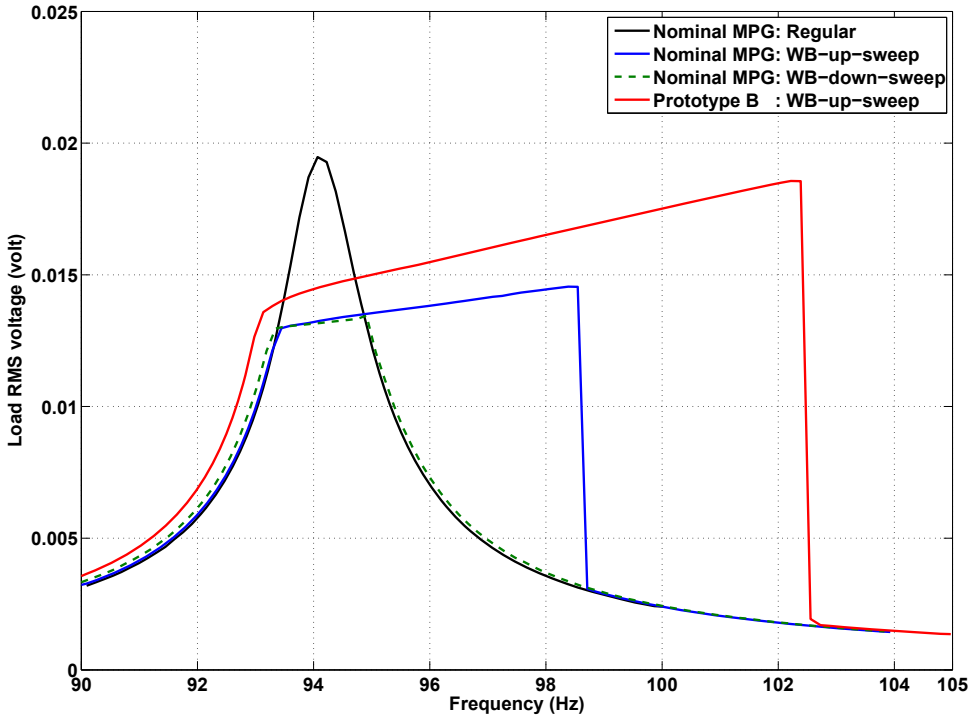

Figure 6.5: Experimental and analytical frequency-response curves for the RMS voltage across R_L for the nominal MPG and prototype B operating in wideband mode.

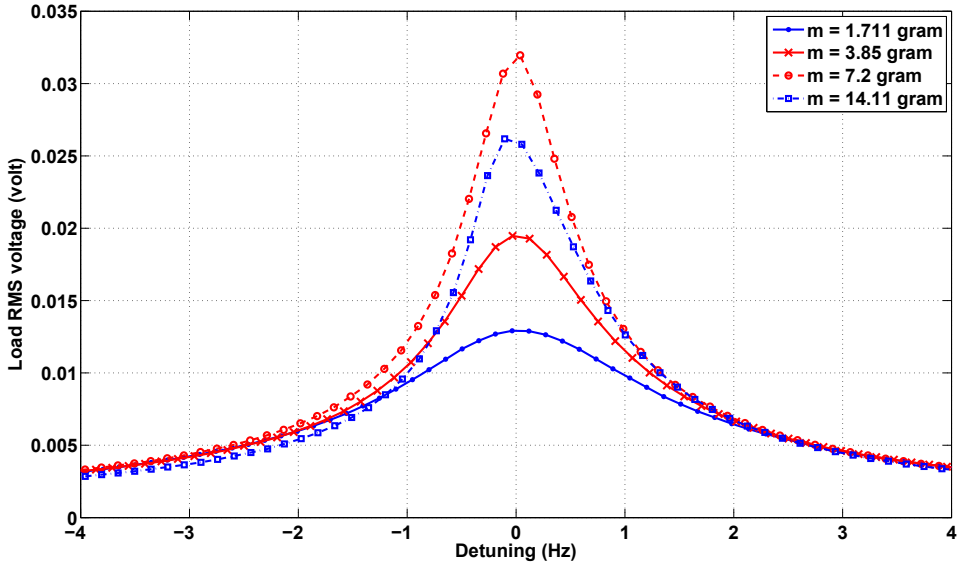

Figure 6.6: The frequency-response curves of the load RMS voltage for the MPGs listed in Table 6.1.

wideband mode. When the beam engages the stopper, the effective stiffness of the MPG increases in proportion to the excursion size $(z-1)$ and time the beam spends engaged with the stopper in each cycle $(\pi - 2\phi_s)$. Higher effective stiffness increases the natural frequency beyond ω_1, causing the resonance to persist in a frequency up-sweep over a wider interval of the frequency spectrum than with a regular MPG. This process is not replicated in a down-sweep, and as a result, both regular and wideband MPGs have the same down-sweep bandwidth. The up-sweep bandwidth as measured with the nominal MPG was 5.75 Hz (from 93.4 Hz to 99.15 Hz), an improvement of 313% over that with the regular MPG. The up-sweep bandwidth as measured with prototype B was 9.4 Hz (from 93.2 Hz to 102.6 Hz), an improvement of 570% over that with the nominal MPG.

In search for the minimum damping ratio ζ_1, we repeated this process for two more prototypes (A and C) with different masses and a similar natural frequency $(\omega = 93.96 \pm 1.08\,\text{Hz})$, Table 6.1. In each case, the beam length and width were

Table 6.1: The mechanical damping coefficient b_m for four MPGs with different masses.

MPG	**Mass grams**	**Stiffness N/m**	**Resonant frequency Hz**	b_m **N s/m**
Prototype A	1.711	576.6	92.4	0.0078
Nominal	3.85	1348	94.1	0.0168
Prototype B	7.2	2539.4	94.52	0.0225
Prototype C	14.11	5024.7	94.8	0.0540

held constant to minimize variation in the mechanical damping coefficient b_m, while the beam thickness was changed to adjust the stiffness. The load resistance and electric damping coefficient were also held constant. Figure 6.6 shows the frequency-response curves of the load RMS voltage for all four MPGs at a base excitation of $F = 0.1\,\mathrm{g}$. The curves are shifted to a common center frequency by plotting them against the detuning frequency; the difference between the excitation frequency and the natural frequency ($\delta = \Omega - \omega$). The load voltage increases with the MPG mass up to a point, then reverses trend to decrease as the mass continues to increase.

Figure 6.7 shows the variations in the mechanical damping coefficient and the damping ratio that occurs with changes in the mass. The mechanical damping coefficient b_m increases monotonically with increasing the MPG mass. The rate of increase accelerates as the mass increases. Since the damping ratio ζ_1 is counter-proportional to the common scaling factor of mass and stiffness s, it decreases initially as the mass increases up to 15 grams; from there on, mechanical damping increases at a faster rate than linear rate, resulting in ζ_1 increasing with increasing the mass. It can be concluded that the damping ratio ζ_1 saturates to a minimum value in the range of $[7.2 - 15]\,\mathrm{gram}$ of the MPG mass Figure 6.7. Therefore, prototype B was adopted as a candidate near optimal MPG design.

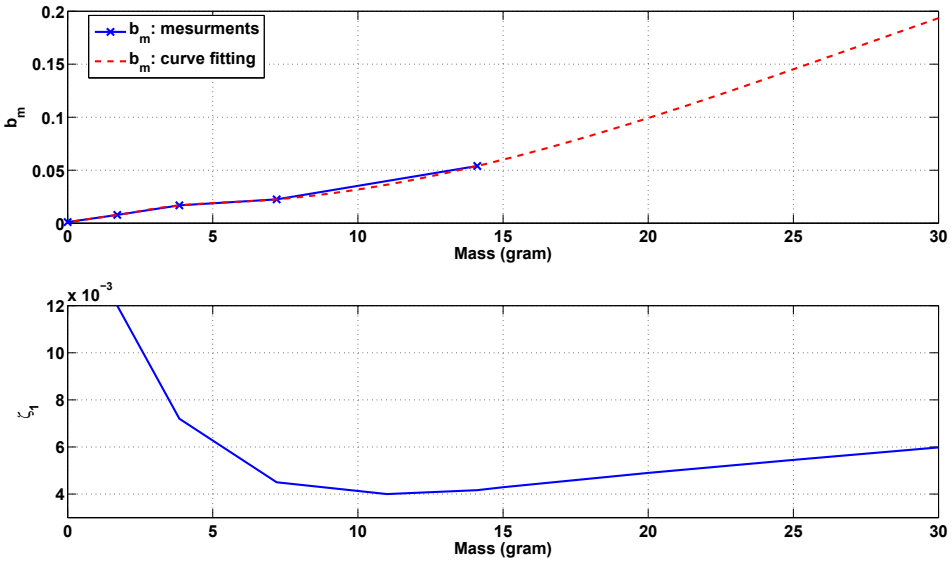

Figure 6.7: Variations in the mechanical damping coefficient b_m and damping ratio (ζ_1) with increasing the MPG mass.

6.3 Optimization of the Output Power and Bandwidth

With the stiffness ratio of the nominal MPG held constant at $\rho^2 = 20$, equations 5.16 and 5.17 were solved for five stopper heights $h_\circ$ distributed at 10 % increments between the half-power ($h_\circ = 81\mu$m) and full-power ($h_\circ = 115\mu$m) levels. Figure 6.8 shows the frequency-response curves for the output power at a base acceleration $F = 0.1$ g (RMS). As the stopper height $h_\circ$ is increased, the stroke becomes larger, leading to larger output power at the expense of a narrower up-sweep bandwidth. This tradeoff continues until the up-sweep bandwidth vanishes when $h_\circ$ corresponds to the full-power level.

To examine this conclusion, the stopper in prototype B was set at four increasing heights $h_\circ$: 80, 98, 114, 130μ m, and a height outside the free stroke. The analytical and experimental results shown in Figure 6.9 confirm the conclusion. The up-sweep

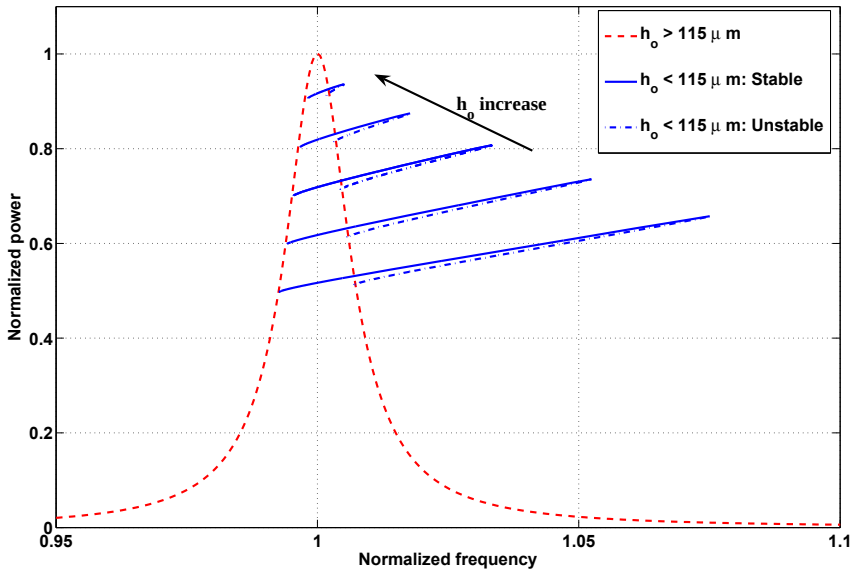

Figure 6.8: Frequency-response curves for the nominal MPG output power as the stopper height increases from $h_\circ = 81\mu$m to 115μm.

bandwidth ranges from a maximum of 9.4 Hz at the shortest height to zero when the stopper does not interfere with the motion of the MPG. As concluded before, the introduction of the stopper has two opposite effects on the energy collected by the MPG. It increases the time during which the MPG collects energy (MPG bandwidth) but decreases the output power level during that time. This section proposes a technique for optimizing the output power level and the bandwidth size with the objective of maximizing the energy collected by the MPG.

It is noticed that the slopes of the experimental frequency-response curves are consistently larger than those of the analytical curves because the analytical model assumes that the rotary inertia is negligible. In fact, the rotary inertia of the larger mass in prototype B has an appreciable effect on the MPG, increasing the size of the MPG excursions beyond the stopper height. In addition, the analytical predictions of the MPG bandwidth gradually underestimate the experimentally measured bandwidth as the stopper is moved to higher locations. The reason for

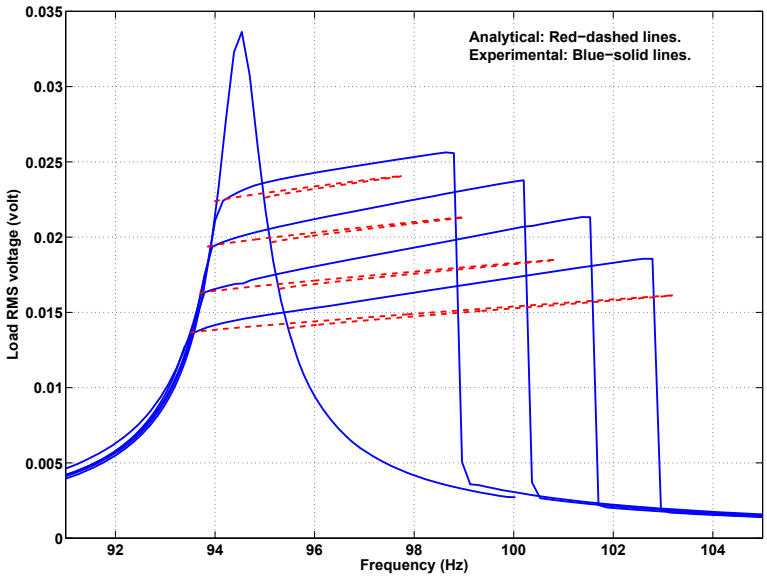

Figure 6.9: Experimental and analytical frequency-response curves for the RMS voltage across R_L in prototype B at different stopper heights $h_\circ$ and $\rho^2 = 20$.

this trend is that the contact damping ratio ζ_2 in the model was set to be equal to that measured for the nominal MPG at half-power. This value is a good estimate of ζ_2 in prototype B at the same stopper height, but it overestimates the contact damping as the stopper height increases, since at these locations, the cantilever engages the stopper at lower velocities, thus reducing the energy losses due to impact and friction.

To examine these hypotheses, the stopper was moved towards the root of the cantilever beam ($l_\circ = 17.7\,\text{mm}$), thereby lowering the stiffness ratio to $\rho^2 = 4.45$. The frequency-response of the output power of the prototype B was found for stopper heights of $h_\circ = 33\mu$, and 47μm, and for a height outside the free stroke. The contact damping ratio was estimated as $\zeta_2 = 0.059$ by fitting the size of the experimental and analytical up-sweep bandwidths at the lower stopper heights. The experimental and analytical results are shown in Figure 6.10. The size of the

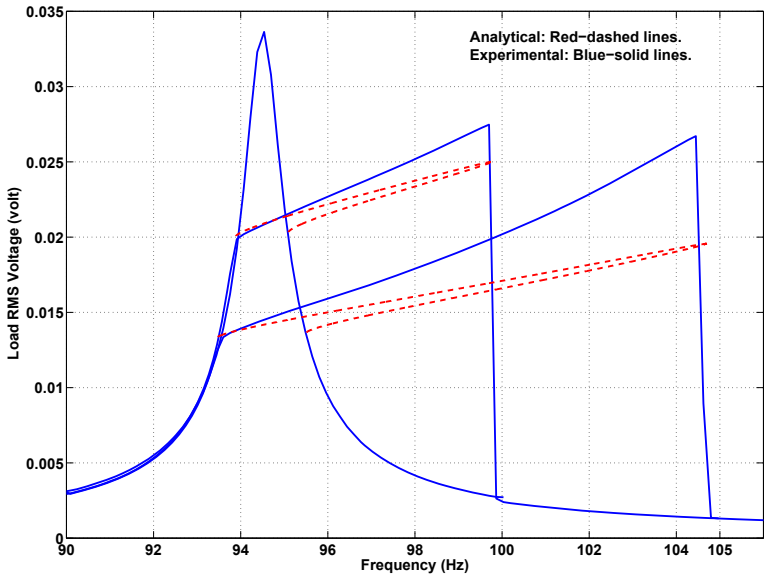

Figure 6.10: Experimental and analytical frequency-response curves for the RMS voltage across R_L in prototype B for $\rho^2 = 4.45$.

MPG excursions beyond the stopper increased as the stopper moved back, thus increasing the moment arm and rotary inertia of the mass, thereby confirming the first hypothesis.

Holding the damping ratio ζ_2 constant while decreasing the stiffness ratio ρ^2 decreases the size of the up-sweep bandwidth, as shown in Figure 5.10; however, the results show that decreasing ρ^2 from 20 to 4.45 results in a larger up-sweep bandwidth of 10.85 Hz. The reason for the decrease is that the shrinkage of the up-sweep bandwidth due to a smaller stiffness ratio is overpowered by the expansion of the bandwidth due to a smaller contact damping ratio (almost 10% of that when $\rho^2 = 20$). The contact damping ratio decreases for $\rho^2 = 4.45$ because closer to the cantilever root the stopper engages the beam at a lower velocity, which decreases the impact and friction energy losses. These conclusions also hold for a stopper height of $h_\circ = 33\mu$m.

It was concluded that reducing the contact damping ratio ζ_2 increases the MPG bandwidth and maximizes energy collection. This goal can be achieved explicitly via the material selection and the optimization of the stopper shape and implicitly via configuring the stopper height $h_\circ$ and offset distance the $l_\circ$ to minimize the velocity of the beam when it engages the stopper. Since $h_\circ$ and $l_\circ$ are used to optimize the output power and the bandwidth of wideband MPGs, that process also involves an implicit optimization of the contact damping ratio ζ_2.

To perform this optimization, the performance of prototype B was evaluated over a grid of six stiffness ratios $\rho^2 = 1.57, 4.45, 6.07, 8.6, 12.75$ and 20 and three stopper heights corresponding to power levels of 50%, 80% and 100% of the nominal MPG. At each grid point, the frequency-response for the load RMS voltage was found experimentally.

If a uniform normal distribution is assumed for the environmental random excitation frequency, the larger the area under the trapezoidal curve, the higher the probability that the MPG harvests more energy over a wider bandwidth. A definition was assigned for a figure of merit, FOM, which is the area under the curve. Figure 6.11 shows a 3-D surface plot that plots the value of the figure of merit versus both the stiffness ratio and the stopper height. As the stiffness ratio is reduced by moving the stopper toward the anchor, the stopper height is adjusted for every stiffness ratio in order to produce the same amount of power at the moment of contact. Should be mentioned here that the figure of merit is maximized at the lowest stiffness ratio and lowest stopper position because at that operating condition, the bandwidth is too large and amount of load power at the right end frequency is more than twice the nominal power because k_2 stiffness value is low and allows a large stroke, which in turn, allows larger load power.

Figure 6.12 shows the experimentally measured up-sweep bandwidth as a function of the stiffness ratio ρ^2 for the three stopper heights. As the stopper moves away from the support, the up-sweep bandwidth increases to a maximum, decreases

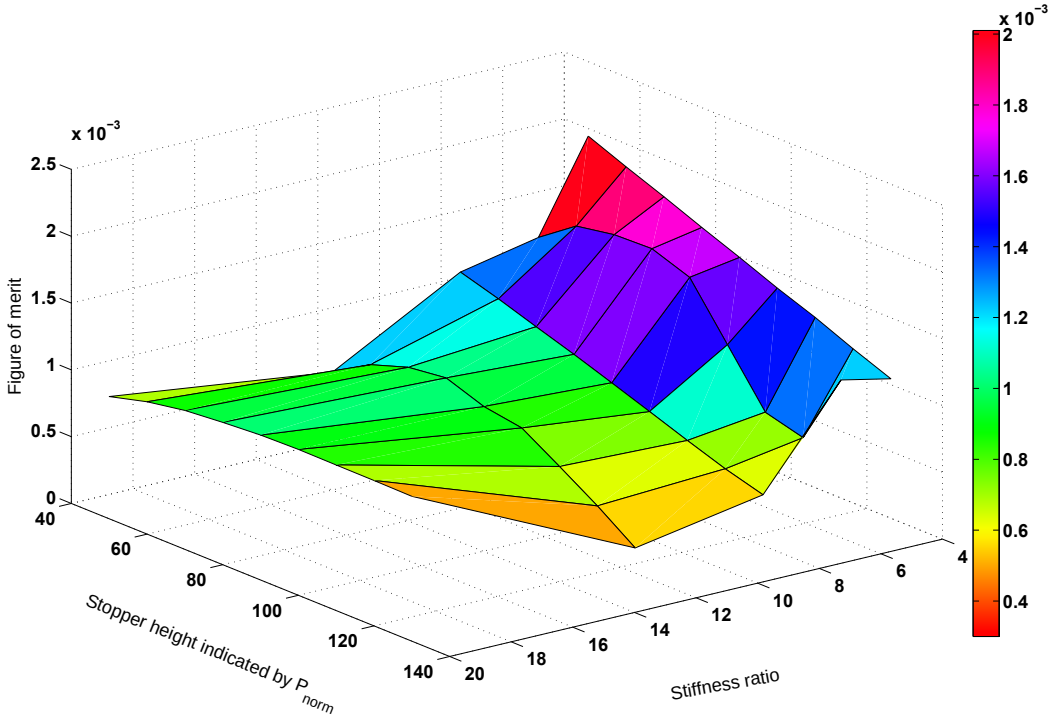

Figure 6.11: Figure of merit versus both the stiffness ratio and the stopper level.

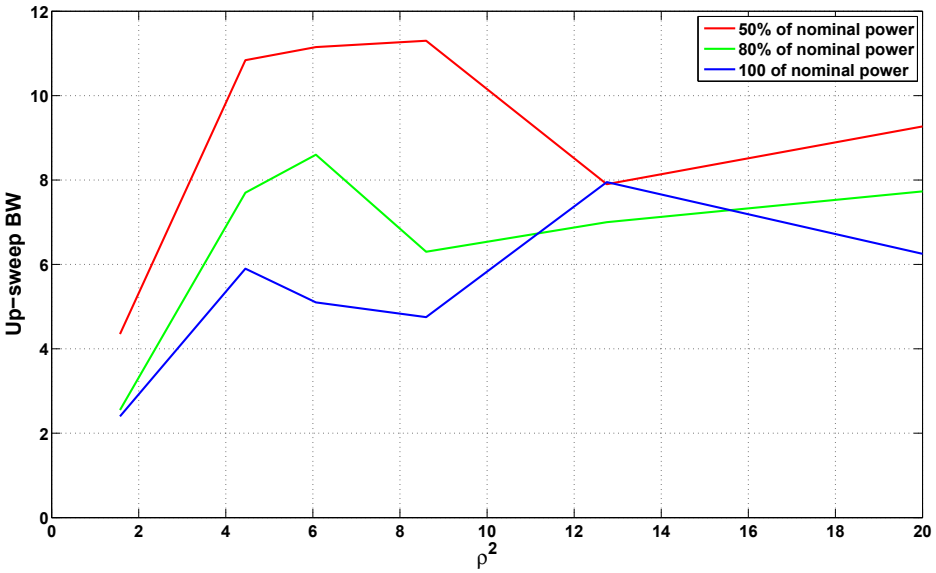

Figure 6.12: The measured up-sweep bandwidth of prototype B at 18 stopper configuration grid points.

to a local minimum, and then increases again. These trends are a consequence of variations in the velocity of the beam along the beam length, which are proportional to the contact damping ratio ζ_2. The cantilever beam responds to excitations in its first deflection mode-shape. Because the other end of the beam is loaded with the inertial mass, the displacement and velocity first increase with the stopper offset distance from the support $l_\circ$ before dropping as the stopper approaches the inertial mass at the other end.

Now if a Gaussian PDF $G(f; f_\circ, \sigma)$ with a mean frequency $f_\circ$ and a standard deviation σ is assumed, which is a more realistic case, at each grid point, as list previously, the frequency-response for the load RMS voltage was found experimentally and convolved with the PDF of the environmental vibrations in order to obtain a figure of merit FoM representing the potential of the MPG to collect energy under that configuration. Since the up-sweep bandwidth is larger than the down-sweep bandwidth (Figure 6.5), equal probability of the frequency of environmental vibra-

tions rising or falling was assumed and the FoMs for the up- and down-sweeps were averaged to obtain

$$FoM = \frac{1}{2}\int_{f_l}^{f_{ru}} P(f)G(f; f_\circ, \sigma)df + \frac{1}{2}\int_{f_l}^{f_{rd}} P(f)G(f; f_\circ, \sigma)df \tag{6.3}$$

where f_l is the left end of the MPG bandwidth, and f_{ru} and f_{rd} are the right end of the up-sweep and down-sweep bandwidths, respectively.

The standard deviation of environmental vibrations was assumed to be $\sigma = 2.5\,\text{Hz}$. The convolution was carried out by numerically integrating equation 6.3 as the mean frequency of the vibrations $f_\circ$ was swept from 90.1 Hz to 105.1 Hz in steps of 0.1 Hz. The maximum FoM is shown for all grid points in Figure 6.13. For stiffness ratios $\rho^2 \leq 4.45$, the performance of the wideband MPG converges and drops for all three stopper heights as the stiffness ratio decreases. The reason for this drop is the shrinkage in the up-sweep bandwidth, as shown Figure 6.12, which diminishes the advantage of the wideband MPG as it begins to approach the performance of a regular MPG. Further, at each stopper height, it was found that the energy collected follows the trends of the up-sweep bandwidth, which indicates that the driver of the wideband MPG advantages over regular MPGs is the ability of the up-sweep bandwidth to match the PDF of the environmental vibrations (i.e., it covers the most active areas of the PDF of environmental vibrations).

The optimal stopper height was found to be in the range $h_\circ = [102, 115]\mu\text{m}$. Setting the stopper to a lower level degrades the energy collected because it reduces the output power while unnecessarily expanding the up-sweep bandwidth beyond the footprint of the PDF of the environmental vibrations, Figure 6.12. Setting the stopper to a higher level also degrades the energy collected, even though it increases the output power, because it shrinks the up-sweep bandwidth so that it does not cover the PDF footprint. Further, the optimal stiffness ratio for this PDF lies in the range $\rho^2 = [4.45, 6.07]$ where the maximum bandwidth of these stopper heights is found.

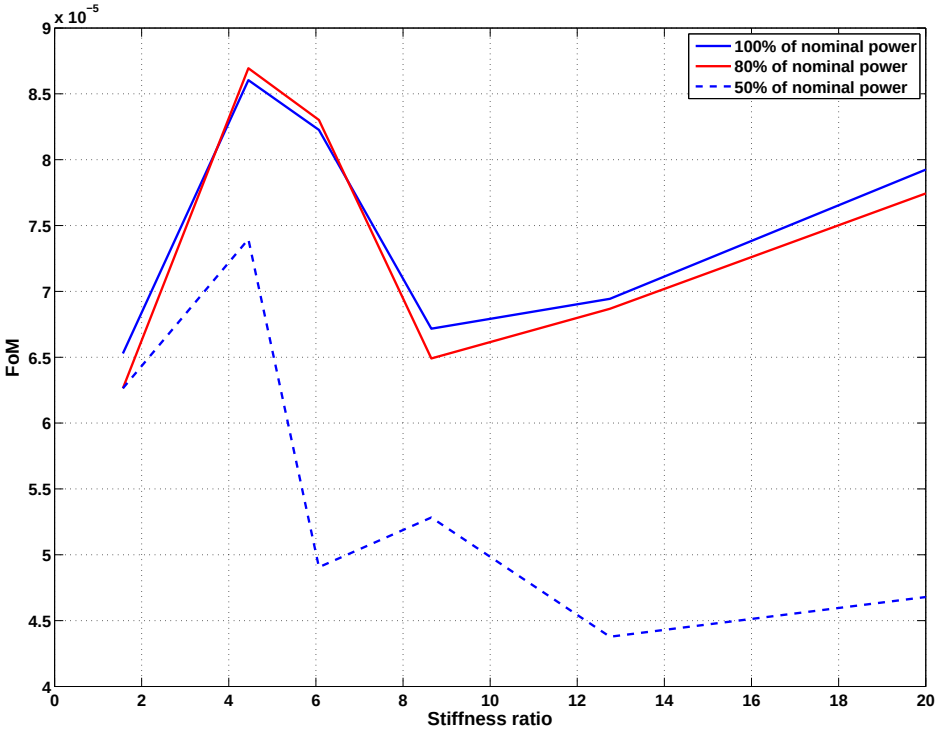

Figure 6.13: Figure of merit for prototype B versus the stiffness ratio.

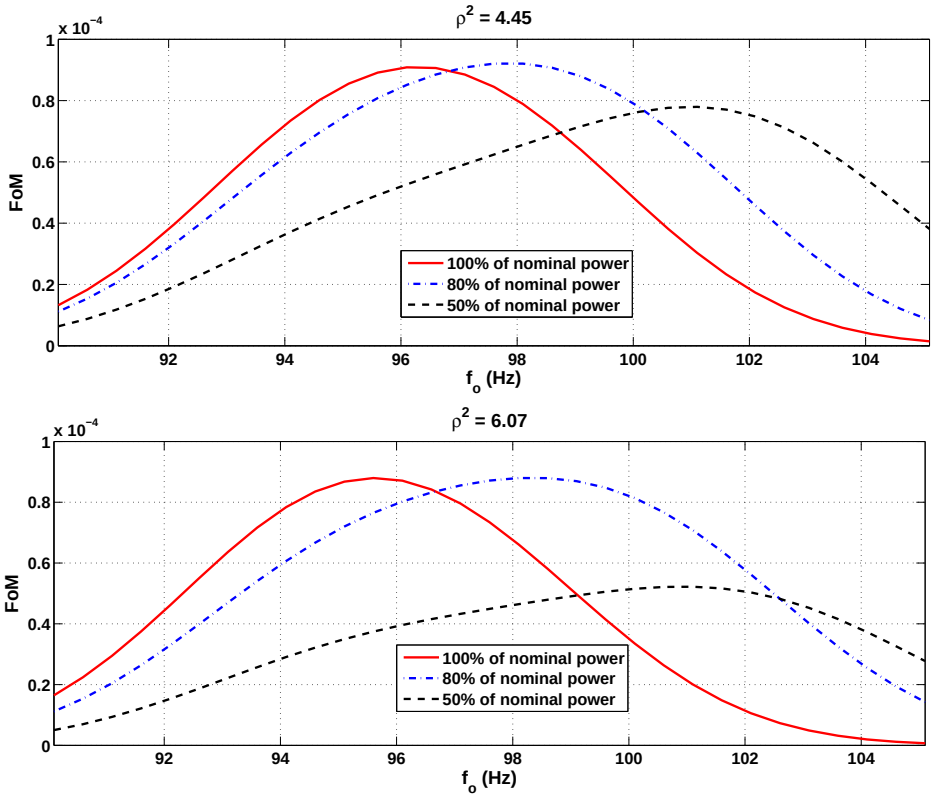

Figure 6.14: The maximum figure of merit for prototype B when $\rho^2 = 4.45$ and 6.07.

The FoM is shown as a function of the mean vibrations frequency $f_\circ$ in Figure 6.14 for stiffness ratios at both ends of this range. Figure 6.14 shows that the MPG performance is better, for all stopper heights, at a stiffness ratio of $\rho^2 = 4.45$. However, since the stopper height $h_\circ = 47\mu$m has a maximum bandwidth at this stiffness ratio, it is less sensitive to perturbations in the PDF of the environmental vibrations. It is concluded that the optimal stopper configuration for prototype B under the given PDF of the environmental vibrations is for ($l_\circ = 17.7$ mm and $h_\circ = 47\mu$m).

The effect of the input environmental vibration standard of deviation, σ, on the value of the FoM was also investigated. Figure 6.15 shows the variation in the FoM for different values of σ: 0.5 Hz, 1 Hz, 2.5 Hz and 10 Hz, for the different

stiffness ratios listed before and after the power level was fixed at the maximum nominal power. For a stiffness ratio of 1.57 and $\sigma = 0.5\,\text{Hz}$, the up-sweep frequency bandwidth, i.e., 2.6 Hz, is very close to the width of the PDF at which the most probability is concentrated: $f_o \pm 3\sigma$. As a result of such a situation, the FoM is maximized at only one peak. As the value of σ increases, the width of the PDF becomes wider with a lower amplitude, which yields a lower value of the FoM. For all other cases, at a very small standard deviation; $\sigma = 0.5\,\text{Hz}$, there are two FoM peaks: one at the left edge of the of the frequency response of the MPG when it starts to engage the stopper and the other peak, with a lower level, when the centre frequency proceeds to the right of the resonant frequency. It was expected that the left peak would be higher than the right peak because it represents the area shared by both the up-sweep and down-sweep. As the value of σ increases, the higher peak decreases to merge with the lower peak at a lower FoM value. When the value of σ reaches very high values, the FoM decreases significantly for all stiffness ratios as a result of the widely distributed input vibration. In this case, it might be helpful to use many WMPGs connected in series so that each one covers a specific region of the input PDF of the vibration. The destructive effect of the series connection would be negligible because only one generator would be tuned while the others would generate only very small amount of power could destroy the total signal generated.

6.4 Dynamic Stability of the Wideband MPG

Variations in the amplitude and frequency of the environmental vibrations are not necessarily smooth. Sudden changes in the amplitude or frequency of the vibration can trigger significant transients in the MPG response. In the region of multi-valued solutions, these external disturbances have the potential to throw the wideband MPG motions out of the basin of attraction of the large periodic orbit, where the

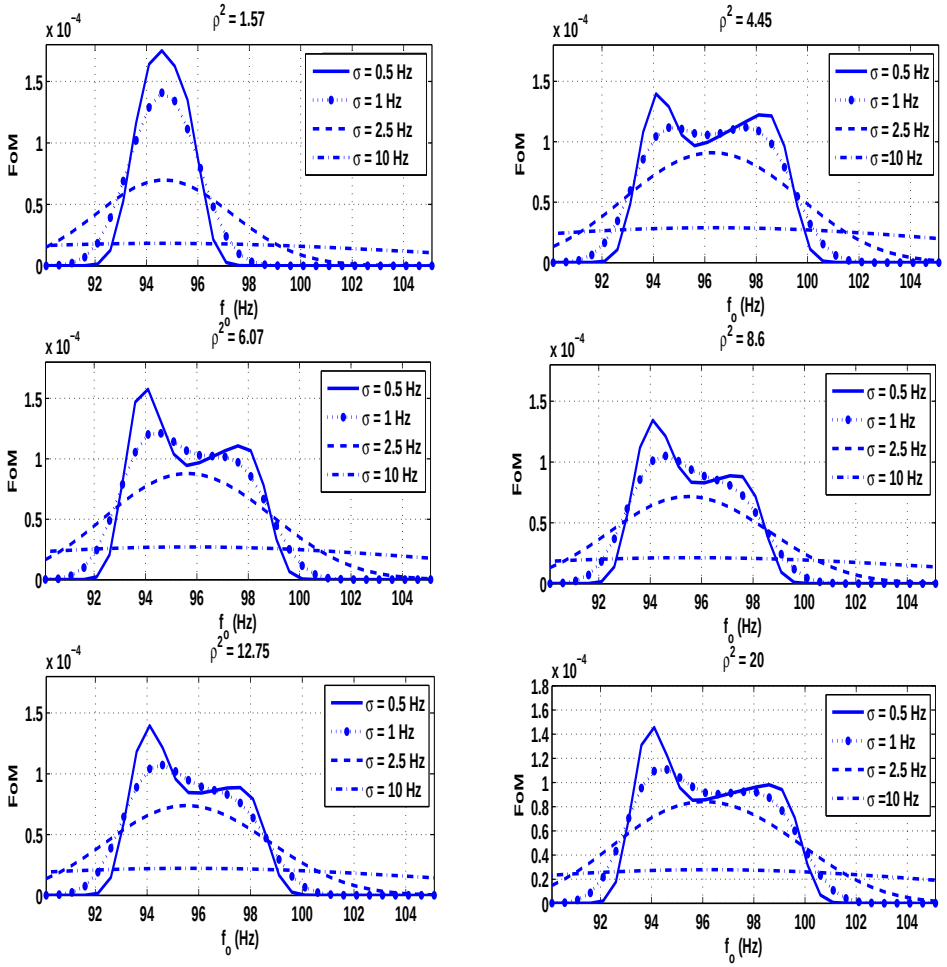

Figure 6.15: Figure of merit for prototype B at different standard diviations.

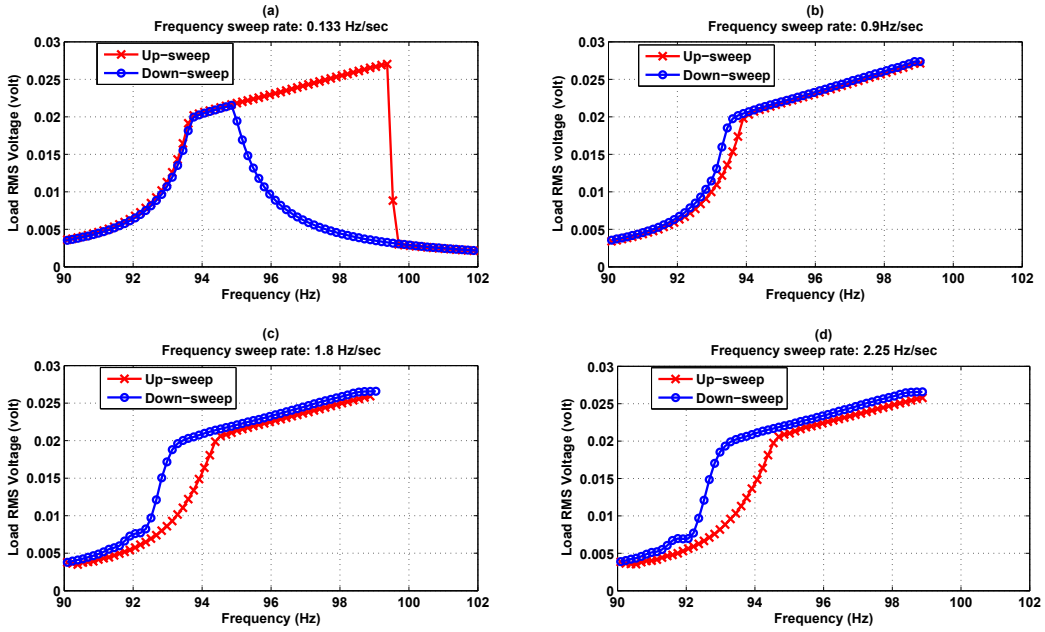

Figure 6.16: Frequency-response curves for the up- and down-sweep of an optimally configured prototype B at sweep rates of (a) 0.133 Hz/sec, (b) 0.9 Hz/sec, (c) 1.8 Hz/sec, and (d) 2.25 Hz/sec.

MPG engages the stopper, to the small periodic orbit of a regular MPG.

A near optimal MPG, that is prototype B with the stopper set at $l_\circ = 17.7\,\text{mm}$ and $h_\circ = 47\mu\text{m}$, was used to investigate the boundaries of the safe basin of motion for the large periodic orbit. First, the excitation frequency was swept up and down in the frequency range of $[90, 102]$Hz at a slow sweep rate of 0.133 Hz/sec as shown in Figure 6.16a, and the frequency-response of the load RMS voltage was recorded. The change in the frequency of excitation under these conditions was smooth enough to allow the response in the up- and down-sweeps to settle down to the same stable orbit throughout the single-valued regions of the frequency-response curve. This response is indicated by the identical up- and down-sweep frequency-response curves in those regions: $[90 - 94.85]$Hz and $[99.7 - 102]$Hz.

The excitation frequency was then swept from 90 Hz to 99 Hz, just before the

end of the branch of the large periodic orbits at 99.4 Hz, and then back at increasing sweep rates of 0.9, 1.8, and 2.25 Hz/sec, respectively, [as shown in Figures 6.16b, c, and d]. A comparison of those figures to figure 6.16a reveals that the up-sweep underestimates and the down-sweep overestimates the size of the motion along the branch of the large periodic orbit and that the difference between the up- and down-sweeps increases as the sweep rate increases. The underestimation and overestimation of the motion occurs in the up-sweeps (down-sweeps) because smaller (larger) transient orbits appear in the time-history used to calculate the RMS voltage. As the sweep rate increases, those transients occupy larger stretches of the time history, thus increasing the divergence between the overestimates and underestimates. As the sweep rate increases and the transients become larger, the left end of the bandwidth, i.e., 93.9 Hz, where the cantilever first engages the stopper, moves to higher values during the up-sweeps because the smaller transient orbits do not have enough time to develop to their full size and thereby touch the stopper. Similarly, the left end of the bandwidth moves to lower values during down-sweeps because the larger transient motions do not have enough time to settle down to smaller orbits away from the stopper. Therefore the increasing distance between the left end of the bandwidth in up- and down-sweeps at the same sweep rate can be used as a measure of the size of the transients available in the MPG motions at any given sweep rate. However, throughout these increasingly larger transients, the largest periodic orbits do not lose stability and disengage from the stopper once the cantilever engaged it at the left end of the bandwidth, which indicates a sizable safe basin of attraction larger than the significant transient motions triggered by the high sweep rates.

To verify the numerical simulations presented in Section 5.2.1, the frequency was swept down from a point outside the half-power bandwidth (98 Hz) to a point that falls within the bandwidth region ($93.9 - 94.85$Hz), and then the frequency was swept up again to a point far from the bandwidth region (101 Hz) at two different

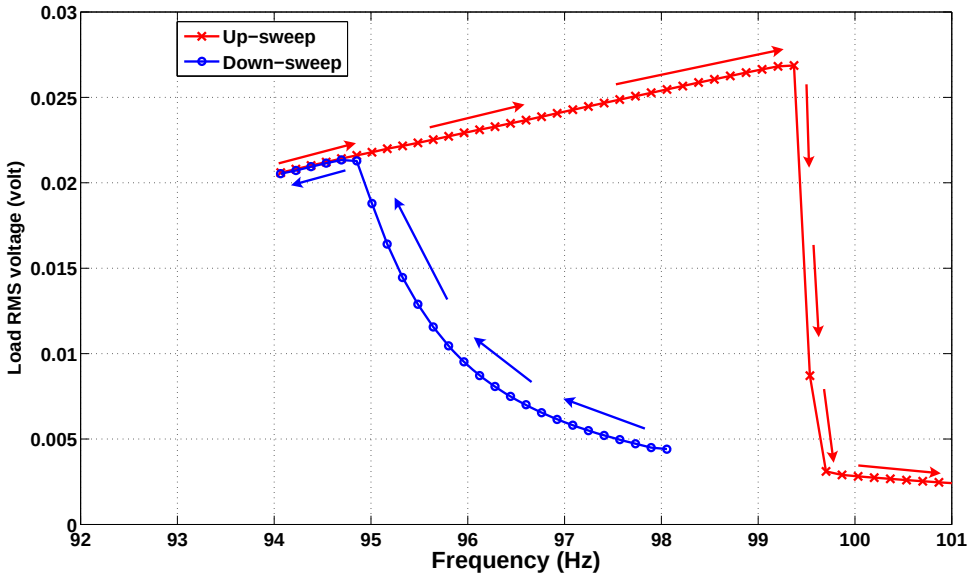

Figure 6.17: Frequency-response curves for the up-and down-sweep of an optimally configured prototype B at sweep rates of 0.133 Hz/sec.

sweep rates. Figures 6.17 and 6.18 show the experimental results for sweep rates of 0.133 Hz/sec and 2.25 Hz/sec, respectively. These figures show clearly the hysteresis behaviour of the WMPG that utilizes piecewise-linear oscillators. It can also be noticed that the WMPG does not lose stability due to the high-frequency sweep rate.

6.5 Summary

A procedure has been developed for optimizing the design of wideband MPGs. It was found that wideband MPGs require two design optimization steps in addition to the traditional technique used in all types of MPGs, that of minimizing mechanical energy losses (the damping coefficient b_m) via structural design and materials selection. The first step, which is common to regular and wideband MPGs, minimizes the MPG damping ratio ζ_1 by increasing the mass and stiffness of the MPG

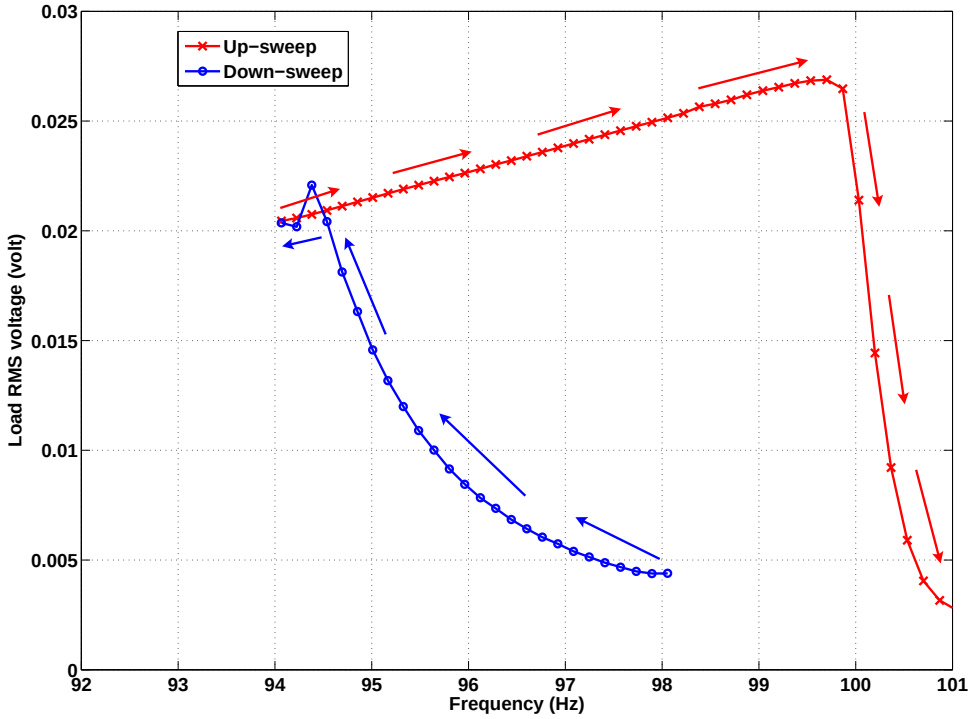

Figure 6.18: Frequency-response curves for the up and down sweep of an optimally configured prototype B at sweep rates of 2.25 Hz/sec.

with a common factor s until the effects of the size cause the rate at which energy losses increase to accelerate beyond the point where $\frac{\partial b_m}{\partial s} = 1$. The second step, which is specific to wideband MPGs, tailors the output power and bandwidth to fit the PDF of the environmental vibrations. A figure of merit FoM was devised in order to quantify the quality of this fit. The FoM was used to configure a wideband MPG to fit a Gaussian PDF $G(f; f_\circ, \sigma)$ with a standard deviation of $\sigma = 2.5\,\text{Hz}$.

In particular, it was found that the dominant factors in the performance of a wideband MPG are the stiffness ratio ρ^2 and the velocity of the MPG structure at the point of impact. These factors are controlled by the configuration of the stopper, namely the stopper height $h_\circ$ and offset distance from the support $l_\circ$. For a cantilever beam-supported MPG, the optimal offset distance was found to be in an intermediate range along the beam length. Therefore, an effective procedure for configuring this class of wideband MPGs is to move the stopper progressively away from the support and to set the offset distance $l_\circ$ to a value slightly larger than the minimum threshold necessary for guaranteeing an up-sweep bandwidth wide enough to cover the PDF of the environmental vibrations at a confidence level of 95%. The stopper height is then set as high as possible in order to minimize the impact velocity, and therefore the contact damping ratio ζ_2, while maintaining the up-sweep bandwidth to be wide enough to cover the PDF at a confidence level of 95%. As well, the boundaries of the safe basin of attraction of a wideband MPG were examined experimentally and it was found that the large periodic motions responsible for the enhanced performance of the wideband MPG were robust with respect to external disturbances.

In conclusion, although the design of wideband MPGs is more challenging than that of regular MPGs, they offer improvements in performance that are significant enough to justify the added design costs.

Chapter 7

Conclusions and Further Work

7.1 Thesis Contributions

The effective deployment of reliable wireless sensor networks is strongly tied to the powering source. The power supply for such applications must be capable of supplying the power required efficiently. Harvesting vibration energy is the main focus of this research because vibrations are present in a wide range of industrial applications. The narrow frequency bandwidth of vibration-based MPGs is the main challenge that restricts the practical application of this kind of power sources.

The major contributions of this work are as follow:

- A novel technique for widening the operating frequency bandwidth of vibration-based MPGs has been developed. The technique is based on replacing the traditional linear oscillators in MPGs with piecewise-linear oscillators. The technique developed is passive, which means that no extra circuits, sensors, or actuators are needed in order to achieve wideband operation. The proposed technique can be applicable to all transduction mechanisms for micro-power generation. A prototype unit, based on electromagnetic transduction mechanism, has been successfully fabricated and tested for the wideband MPG.

The optimization of the new technique and the development of the design procedure were also presented.

- Closed-form expressions for the up-sweep bandwidth were presented and validated experimentally.

- A complete design showing the possibility of applying the proposed technique in MEMS-based MPGs using only one photo mask, which reduces the complexity of the microfabrication process, was also presented.

7.2 Thesis Conclusions

The conclusions of the research accomplished in this thesis can be presented as follows:

- A standard electromagnetic-based MPG was modified to accommodate a stopper with adjustable vertical and horizontal positions. The vertical position of the stopper determines the level of the power generated while the horizontal position determines the value of the stiffness ratio. The stiffness of the oscillator changes abruptly from a low to a high value when the cantilever engages the stopper, thus causing a hardening effect. It was found that a one-sided stopper architecture increases the bandwidth during the frequency up-sweep, while maintaining the same bandwidth as that produced with a regular structure during the frequency down-sweep, thus resulting in performance hysteresis, but with a positive effect. The method of averaging was adopted to produce an analytical model for determining closed-form expressions for the up-sweep bandwidth. In addition, the SIMULINK environment was utilized to develop a numerical model that used to simulate such behaviour. The prototype was examined experimentally, and good agreement was achieved

among the analytical, numerical, and experimental results. An additional analytical model was developed for a two-sided structure, in which two stoppers were placed at symmetrical locations of the cantilever. The analysis showed that the one-sided and two-sided structures have almost the same maximum up-sweep bandwidth. For the same stiffness ratio, the up-sweep bandwidth of the two-sided MPG is larger than the up-sweep bandwidth of the one-sided MPG. However, because adding a second stopper increases the complexity of the structure, an MPG with one-sided stopper is recommended, but with a higher stiffness ratio to compensate for the smaller up-sweep bandwidth that it produces compared with the two-sided MPG.

- An electromagnetic MEMS-based MPG was designed and fabricated, and its performance was simulated. To implement the piece-wise linear oscillators in the MEMS structures, the design took into consideration the addition of the stoppers, i.e., the auxiliary springs, after the shuttle travels a pre-calculated stroke. The analytical model was then modified in order to obtain the closed-form expressions for the up-sweep frequency bandwidth. The moving shuttle was fabricated using the DRIE micromachining technique in order to obtain a high aspect ratio preventing the out-of-plane motion. The coil was wrapped around a lexan core, rather than a metallic core, so that the the eddy current losses would be eliminated. It is expected that the contact damping ratio (ζ_2) will be reduced in the MEMS-based structure, which will lead to a larger up-sweep bandwidth; i.e., more energy collected.

- A design procedure for optimizing the performance of wideband MPGs was proposed. The frequency response for the output power was measured experimentally for different values of stiffness ratios and stopper heights. It was found that for a fixed excitation frequency PDF (fixed centre frequency), as the stiffness ratio decreases, the contact damping ratio decreases and both the

up-sweep bandwidth and the power level increase. However, if the stopper height increases, both the contact damping ratio and the up-sweep bandwidth decrease and the power level increases. For an excitation frequency with varying centre frequency, the FoM maximizes when most of the active area of the excitation PDF lies within the up-sweep bandwidth. Lowering the stopper height for this case makes the FoM flatter and less sensitive to the variation of the PDF centre frequency. It was found that the optimum operating point for the MPG depends greatly on the Probability Density Function (PDF) of the environmental excitation frequency. A figure of merit (FoM) was developed in order to quantify the potential of the wideband MPG for collecting energy under a specific PDF frequency pattern. The design procedure was summarized by selecting optimum values of the stiffness ratio and the contact damping ratio through the adjustment of the horizontal and vertical positions of the stopper, respectively. The stability of the optimized structure with different frequency sweep rates was examined experimentally, and it was shown that the performance of the MPG is robust with respect to high-frequency sweep rates.

In conclusion, the performance of the MPG should not be determined by the output power density; it should be measured based on the average amount of energy collected according to the Gaussian PDF of the environmental excitations.

7.3 Further Research Work

The research accomplished in this thesis can be continued in several directions as follows:

- In this research, piecewise-linear oscillators were implemented for electromagnetic-based MPGs. Theoretically, the technique applies to any vibration-based

MPG; however, more research work is needed with respect to the application of such a technique for both electrostatic and piezoelectric MPGs. The electrostatic transduction mechanism is characterized by a non-linear electrical damping coefficient, which may change the dynamics of the system.

- With respect to the analytical model used in order to obtain the closed-form expressions, the model needs first to be modified so that it considers the mass moment of inertia. Second, the contact damping ratio (ζ_2) needs to be obtained analytically rather than experimentally. With a more accurate analytical model, the optimization process can be run even before the system is built and examined.

- Detailed investigation of methods of reducing the contact damping ratio (ζ_2) are required if the the performance of wideband MPGs is to be significantly enhanced. The reduction of ζ_2 could be achieved by optimizing the shape of the stopper in order to minimize losses during impact with the cantilever. Also, low contact energy dissipation methods must be investigated.

- With respect to the MEMS-based MPG, the coil can be microfabricated using electroplating techniques; however, the coil may not be long enough to produce a reasonable amount of voltage. Multi-layered electroplated coils may be considered as a mean of producing coils with sufficient effective length. This process would result in MPGs with small airgap, which leads to high magnetic field densities resulting in picking up motion from low-gs vibrations. Methods of producing efficient micromachined permanent magnets must also be developed so that the fabrication methods will be more compatible with current inexpensive micromachining techniques.

Bibliography

[1] IEEE 802.15.4 Standard 2003 (New York: IEEE)

[2] B. Warneke, M. Last, B. Leibowitz, and K. Pister, "Smart dust: communicating with a cubic-millimeter computer", *IEEE Computer Society Press*, 2001, vol. 34, pp. 44–51.

[3] J. Rabaye, M. Ammer, J. Da Silva, D. Patel, and S. Roundy, "Picoradio supports ad hoc ultra-low power wireless networking", *IEEE Computer Society Press*, 2000, vol. 33, pp. 42–48.

[4] C. Enz, A. El-Hoiydi, J. Decotignie, and V. Peiris, "WiseNET: An ultralow-power wireless sensor network solution", *IEEE Computer Society Press*, 2004, vol. 37, pp. 62–70.

[5] C. Mathuna, T. Donnell, R. Martinez-Catala, J. Rohan, and B. Flynn, "Energy scavenging for long-term deployable wireless sensor networks", *Talanta*, May 2008, vol. 75(3), pp. 613–623.

[6] V. Raghunathan, C. Schurgers, S. Park, and M. Skrivastava, "Energy-aware wireless microsensor networks", *IEEE Signal Process. Mag.*, 2002, vol. 19, pp. 40–50.

[7] J. Holloday, E. Jones, M. Phelps, and J. Hu, "microfuel processor for use in a miniature power supply", *J. Power Sources*, 2001, vol. 108, pp. 21–27.

[8] S. Roundy, P. Wright, and J. Rabaey, "Energy scavenging for wireless sensor networks with special focus on vibrations", *Kluwer Academic publishers*, 2004.

[9] S. Roundy, "Energy Scavenging for Wireless Sensor Nodes with a Focus on Vibration to Electricity Conversion", a Ph.D. thesis, T*he University of California, Berkeley*, 2003.

[10] S. Roundy, E. Leland, AND J. Baker "Improving power output for vibration-based energy scavenging", *IEEE Computer Society Press*, 2005, vol. 4(1), pp. 28–36.

[11] S. Beeby, M. Tudor, and N. White, "Energy harvesting vibration sources for microsystems applications", *J. Meas. Sci. Technol.*, 2006, vol. 17, pp. 175-195.

[12] J. Nye, "Physical Properties of Crystals", *Oxford Science Publications*, 1957.

[13] N. White, and J. Turner, "Thick-film sensors: past, present and future", *J. Meas. Sci. Technol.*, 1997, vol. 8, pp. 1-20.

[14] A. Erturk, and D. Inman, "Issues in mathematical modeling of piezoelectric energy harvesters", *J. Smart Materials and Structures*, 2008, vol. 17, 065016.

[15] J. Kymissis, C. Kendall, J. Paradiso, AND N. Gershenfeld, "Parasitic power harvesting in shoes", *Second International Symposium on Wearable Computers*, October 1998, pp. 132–139, .

[16] J. Antaki, G. Bertocci, E. Green, A. Nadeem, T. Rintoul, R. Kormos, and B. Griffith, "A gait powered autologous battery charging system for artificial organs", *Am. Soc. for Artif. Internal Organs*, 1995, vol. 41, pp. 588-95

[17] H. Yoon, G. Washington, and A. Danak, "Modelling, optimisation, and design of efficient initially curved piezoceramic unimorphs for energy harvesting applications", *J. Intelligent Material Systems and Structures*, 2005, vol.16, pp. 877-888.

[18] L. Mateu, and F. Moll, "Optimum piezoelectric bending beam structures for energy harvesting using shoe inserts", *J. Intelligent Material Systems and Structures*, 2005, vol. 16, pp. 835-845.

[19] N. Shenck, and J. Paradiso, "Energy scavenging with shoe-mounted piezoelectrics", *IEEE J. Microelectromechanical systems*, 2001, vol. 21(3), pp. 30–42.

[20] M. Ramsay, and W. Clark, "Piezoelectric energy harvesting for bio-MEMS applications", *Proc. SPIE*, 2001, 4332, pp. 429-38.

[21] P. Miao, P. Mitcheson, A. Holmes, E. Yeatman, T. Green, and B. Stark, "MEMS inertial power generators for biomedical applications", *J. Microsyst. Technol.*, 2006, vol. 12, pp. 1079-1083.

[22] E. Reilly, E. Carleton, and P. Wright, "Thin film piezoelectric energy scavenging systems for long term medical monitoring", *Int. Workshop on Wearable and Implantable Body Sensor Networks*, 3–5 April, BSN 2006, pp.41–44.

[23] S. Platt, S. Farritor, K. Garvin, and H. Haider, "The use of piezoelectric ceramics for electric power generation within orthopedic implants", *IEEE/ASME Trans. Mechatron.*, 2005, vol. 10, pp. 455-461.

[24] S. Roundy, and P. Wright, "A piezoelectric vibration based generator for wireless electronics", *J. Smart Mater. Struct.*, 2004, vol. 13, pp. 1131-1142.

[25] S. Beeby, A. Blackburn, and N. White, "Processing of PZT piezoelectric thick films on silicon for microelectromechanical systems", *J. Micromech. Microeng.*, 1999, vol. 9, pp. 218-229.

[26] R. Torah, S. Beeby, and N. White, "An improved thick-film piezoelectric material by powder blending and enhanced processing parameters", *IEEE Trans. UFFC*, 2005, vol. 52, pp. 10-16.

[27] J. Mur Miranda, "Electrostatic Vibration-to-Electric Energy Conversion", Ph.D Thesis, *Massachusetts Institute of Technology*, 2004.

[28] S. Meninger, J. Mur-Miranda, J. Lang, A. Chandrakasan, A. Slocum, M. Schmidt, and R. Amirtharajah, "Vibration to electric energy conversion", *IEEE Trans VLSI Systems*, 2001, vol. 9, pp. 64-76.

[29] W. Ma, M. Wong, and L. Ruber, "Dynamic simulation of an implemented electrostatic power micro-generator", *Proc. Design, Test, Integration and Packaging of MEMS and MOEMS*, 2005, pp. 380-385.

[30] Yi Chiu, Chiung-Ting Kuo, Yu-Shan Chu, "MEMS design and fabrication of an electrostatic vibration-to-electricity energy converter", *J. Microsyst Technol*, 2007, vol. 13, pp.1663-1669.

[31] R. Tashiro, N. Kabai, K. Katayama, Y. Ishizuka, F. Tsuboi, and K. Tsuchiya, "Development of an electrostatic generator that harnesses the motion of a living body", *JSME Int. Journal Series C*, 2000, vol. 43, pp. 916-622.

[32] Y. Chiu and V. Tseng, "A capacitive vibration-to-electricity energy converter with integrated mechanical switches", *J. Micromech. Microeng.*, 2008, vol. 18, 104004.

[33] Y. Arakawa, Y. Suzuki, and N. Kasagi, "Micro seismic power generator using electret polymer film", *Power MEMS Conference*, Kyoto, Japan, 2004, pp. 187-190.

[34] L. Hsi-wen, and T. Yu-Chong, "Parylene-based electret power generators", *J. Micromech. Microeng.*, 2008, vol. 18, 104006.

[35] F. Peano, and T. Tambosso, "Design and optimisation of a MEMS electret-based capacitive energy scavenger", *IEEE J. Microelectromech. Syst.*, 2005, vol. 14, pp. 429-435.

[36] C. Tsung-Shune, "Permanent magnet films for applications in microelectromechanical systems", *Journal of Magnetism and Magnetic Materials*, 2000, vol. 209, pp. 75–79.

[37] W. Trimmer, "Microrobots and micromechanical systems", *J. Sensors and Actuators*, 1989, vol. 19, pp. 267-287.

[38] O. Cugat, J. Delamare, and G. Reyne, "Magnetic micro-actuators and systems (MAGMAS)", *IEEE Trans. Magn.*,2003, vol. 39(6), pp. 3607-3612.

[39] D. Arnold, "Review of microscale magnetic power generation", *IEEE Trans. Magnetics*, 2007, vol. 43(11), pp. 3940-3951.

[40] S. Priya, and D. Inman, "Energy Harvesting Technologies", *Springer*, 2009.

[41] T. Sterken, K. Baert, C. Van Hoof, R. Puers, G. Borghs, and P. Fiorini, "Comparative Modeling for Vibration Scavengers", *Proceedings of IEEE Sensors*, 2004, vol. 3, pp. 1249–1252.

[42] R. Amirtharajah, and A. Chandrakasan, "Self-powered signal processing using vibration-based power generation", *IEEE Journal of Solid-Stat Circuits*, 1998, vol. 33(5), pp. 687–695.

[43] M. El-Hami, P. Glynne-Jones, N. White, M. Hill, S. Beeby, E. James, A. Brown, and J. Ross, "A new approach towards the design of a vibration-based microelectromechanical generator", *Proc. 14th European Conference on Solid-State Transducers*, Copenhagen, August 2730, 2000, pp. 483-486.

[44] M. El-Hami, P. Glynne-Jones, N. White, M. Hill, S. Beeby, E. James, A. Brown, and N. Ross, "Design and fabrication of a new vibration-based electromechanical power generator", *J. Sensors and Actuators, A: Physical*, 2001, vol. 92, pp.335-342.

[45] N. Neil, H. Wong, J. Wen, H. Philip, and Zhiyu Wen, "A laser-micromachined multi-modal resonating power transducer for wireless sensing systems", *J. Sensors and Actuators, A: Physical*, 2002, vol. 97–98, pp. 685–690.

[46] J. Wen, Z. Wen, P. Wong, G. Chan, and P. Leong, "A micromachined vibration-induced power generator for low power sensors for robotic systems", *Proceedings of the World Automation Congress: 8th International Symposium on Robotics with Applications*, June 11-14, 2000, Hawaii, USA,.

[47] J. Wen,C. Terry Ho, M. Gordon Chan, H. Philip Leong, and H. Yung Wong, "Infrared signal transmission by a Laser-Micromachined Vibration-Induced power generator", *Proc. of 43rd IEEE Midwest Symposium on Circuits and Systems*, 2000, Lasing MI, pp. 236–239.

[48] M. Johnny Lee, C. Steve Yung, J. Wen Li, and H. Philip Leong, "Development of an AA size energy transducer with micro resonators", *IEEE International Symposium On Circuit and Systems*, 2003, Thailand, pp. IV.876–IV.879.

[49] P. Glynne-Jones, M. Tudor, S. Beeby, N. White, "An electromagnetic, vibration-powered generator for intelligent sensor systems", *J. Sensors and Actuators*, 2004, vol. A110(13)pp. 344-349.

[50] S. Beeby, R. Torah, M. Tudor, P. Glynne-Jones, T. ODonnell, C. Saha, and S. Roy, "A micro electromagnetic generator for vibration energy harvesting", *J. Micromech. Microeng.*, 2007, vol. 17, pp. 1257-1265.

[51] R. Torah, P. Glynne-Jones, M. Tudor, T. ODonnell, S. Roy, and S. Beeby, "Self-powered autonomous wireless sensor node using vibration energy harvesting", *J. Meas. Sci. Technol.*, 2008, vol. 19, 125202.

[52] K. Sasaki, Y. Osaki, J. Okazaki, H. Hosaka, and K. Itao, "Vibration-based automatic power-generation system", *J. Microsyst. Technol.*, 2005, vol. 11(810), pp. 965–969.

[53] V. Thomas, and T. Gerhard, "Design and optimization of a linear vibration-driven electromagnetic micro-power generator", *J. Sensors and Actuators*, 2007, vol. A135, pp. 765-775.

[54] C. Saha, T. O'Donnell, N. Wang, and P. McCloskey, "Electromagnetic generator for harvesting energy from human motion", *J. Sensors and Actuators*, 2008, vol. A147, pp. 248-253.

[55] Z. Hadas, M. Kluge, V. Singule, and C. Ondrusek, "Electromagnetic Vibration Power Generator", *IEEE International Symposium on Diagnostics for Electric Machines, Power Electronics and Drives*, 2007, pp. 451–455 .

[56] C. Williams, and R. Yates, "Analysis of a micro-electric generator for microsystems", *J. Sensors and Actuators*, 1996 vol. A52(1), pp. 8-11.

[57] C. Shearwood and R. Yates, "Development of an electromagnetic microgenerator", *IEEE Electron. Lett.*, 1997, vol. 33(22), pp. 1883-1884.

[58] C. Williams, C. Shearwood, M. Harradine, P. Mellor, T. Birch, and R. Yates, "Development of an electromagnetic micro-generator", *IEE Proc. Circuits, Devices Syst.*, 2001, vol. 148(6), pp. 337-342.

[59] H. Kulah, and K. Najafi, "An electromagnetic micro power generator for low frequency environmental vibrations", *17th IEEE International Conference on Microelectromechanical Systems*, 2004, pp. 237–240.

[60] M. Mizuno, and D. Chetwynd, "Investigation of resonance microgenerator", *J. Micromech. and Microeng.*, 2003, vol. 13, pp. 209–216.

[61] C. Serre, A. Perez-Rodrguez, N. Fondevilla, E. Martincic, S. Martnez, J. Morante, J. Montserrat, and J. Esteve, "IDesign and implementation of mechanical resonators for optimized inertial electromagnetic microgenerators", *J. Microsyst. Technol.*, 2008, vol. 14, pp. 653-658.

[62] C. Pan, Y. Hwang, H. Hu, and H. Liu, "Fabrication and analysis of a magnetic self-power microgenerator", *J. Magnetism and Magnetic Material.*, 2006, vol. 304(1), pp. e394-e396.

[63] E. Koukharenko, S. Beeby, M. Tudor, N. White, T. ODonnell, C. Saha, S. Kulkarni, and S. Roy, "Microelectromechanical systems vibration powered electromagnetic generator for wireless sensor applications", *J. Microsyst Technol*, 2006, vol. 12, pp. 1071-1077.

[64] S. Kulkarni, S. Roy, T. ODonnell, S. Beeby, and J. Tudor, "Vibration Based Electromagnetic MicroPower Generator on Silicon", *J. Applied Physics*, 2006, vol.99, 08P511.

[65] Pei-Hong Wanga, Xu-Han Daia, Dong-Ming Fang, and Xiao-Lin Zhao, "Design, fabrication and performance of a new vibration-based electromagnetic micro power generator", *Microelectronics Journal*, 2007, vol. 38, pp. 1175-1180.

[66] P. Mitcheson, E. Reilly, T. Toh, P. Wright, and E. Yeatman, "Performance limits of the three MEMS inertial energy generator transduction types", *J. Micromech. Microeng.*, 2007, vol. 17, pp. S211-S216.

[67] I. Sari, T. Balkan, and H, Kulah, "A wideband electromagnetic micro power generator for wireless microsystems", *Transducers and Eurosensors'07*, 2007, pp. 275–278.

[68] I. Sari, T. Balkan, and H. Kulah, "An electromagnetic micro power generator for wideband environmental vibrations", *J. Sensors and Actuators*, 2008, vol. A145146, pp. 405-413.

[69] S. Shahruz, "Design of mechanical band-pass filters with large frequency bands for energy scavenging", *Journal of Mechatronics*, 2006, vol. 16, pp. 523-531.

[70] S Shahruz, and Jingang Yi, "Performance of mechanical band-pass filters used in energy scavenging in the presence of fabrication errors and coupling", *Proceedings of IMECE2007: 2007 ASME International Mechanical Engineering Congress and Exposition*, 2007, Seattle, Washington, USA, 43123.

[71] S. Shahruz, "Performance of Mechanical Bandpass Filters Used in Energy Scavenging in the Presence of Fabrication Errors and Coupling", *J. Vibration and Acoustics*, 2008, vol. 130, 054505-2.

[72] S. Shahruz, "Design of Mechanical Band-Pass Filters for Energy Scavenging: Multi-Degree-of-Freedom Models", *J. Vibration and Control*, 2008, vol. 14(5), pp. 753–768.

[73] M. Ferrari, V. Ferrari, M. Guizzetti, D. Marioli, and A. Taroni, "Piezoelectric multifrequency energy converter for power harvesting in autonomous microsystems", *J. Sensors and Actuators*, 2008, vol. A142, pp. 329-335.

[74] Jing-Quan Liu, Hua-Bin Fang, Zheng-Yi Xu, Xin-Hui Mao, Xiu-Cheng Shen, Di Chen, Hang Liao, and Bing-Chu Cai, "A MEMS-based piezoelectric power generator array for vibration energy harvesting", *Microelectronics Journal*, 2008, vol. 39, pp. 802-806.

[75] E. Leland and P. Wright, "Resonance tuning of piezoelectric vibration energy scavenging generators using compressive axial preload", *J. Smart Materials and Structures*, 2006, vol. 15 , pp. 1413-1420.

[76] J. Loverich, R. Geiger, and J. Frank, "Stiffness nonlinearity as a means for resonance frequency tuning and enhancing mechanical robustness of vibration power harvesters", *Active and Passive Smart Structures and Integrated Systems, Proc. of SPIE*, 2008, vol. 6928, 692805.

[77] V. Challa, M. Prasad, Y. Shi, and F. Fisher, "A vibration energy harvesting device with bidirectional resonance frequency tunability", *J. Smart Materials and Structures*, 2007, vol. 17, 015035.

[78] V. Challa, M. Prasad, and F. Fisher, "High efficiency energy harvesting device with mamagnetic coupling for resonance frequency tuning", *Sensors and Smart Structures Technologies for Civil, Mechanical, and Aerospace Systems, Proc. of SPIE*, 2008, vol. 6932, 69323Q.

[79] S. Burrow, and L. Clare, "A Resonant Generator with Non-Linear Compliance for Energy Harvesting in High Vibrational Environments", *IEMDC '07*, 3-5 May, 2007, vol. 1, pp. 715–720 .

[80] S. Burrow, L. Clare, A. Carrella, and D. Barton, "Vibration energy harvesters with non-linear compliance", *Active and Passive Smart Structures and Integrated Systems, Proc. of SPIE*, 2008 vol. 6928, 692807.

[81] B. Yang, C. Lee,W. Xiang, J. Xie, J. Han He, R. Kotlanka, S. Low and H. Feng, "Electromagnetic energy harvesting from vibrations of multiple frequencies", *J. Micromech. Microeng.*, 2009, vol. 19, 035001.

[82] J. Wen, Z. Wen, P. Wong, G. Chan, and P. Leong, "A micromachined vibration-induced power generator for low power sensors for robotic systems", *Proc. Of the World Automation Congress*, June 11-14, 2000, Hawaii, USA.

[83] N. Stephen, "On energy harvesting from ambient vibration", *J. Sound and Vibration.*, 2006, vol. 293, pp. 409-25.

[84] Permanent Magnets data sheets available from MMG Magdev Limited.

[85] M. Harris, "Shock and Vibration Handbook", *McGraw-HILL*, Fourth Eddition, 1995.

[86] P. Laura, J. Pombo, and E. Susemihl, "A note on the vibrations of a clamped-free beam with a mass at the free end", *J. Sound and Vibration*, 1974, vol. 37(2), pp. 161–168.

[87] A. Narimani, and F. Golnaraghi, "Frequency Response of a Piecewise linear Vibration isolator", *J. Vibration and control*, 2004, pp. 1775–1794.

[88] A. Nayfeh, and B. Balachandran, "Applied Nonlinear Dynamics", *Wiley, New York*, 1995.